Mixing, exchange, and residence times in estuaries with complex bathymetry

Erin Morgan Broatch

A dissertation
submitted in partial fulfillment of the
requirements for the degree of

Doctor of Philosophy

University of Washington
2025

Reading Committee:
Parker MacCready, Chair
Alison R. Gray
W. Rockwell Geyer

Program Authorized to Offer Degree:
Oceanography

University of Washington

Abstract

Mixing, exchange, and residence times in estuaries with complex bathymetry

Erin Morgan Broatch

Chair of the Supervisory Committee:

Parker MacCready
School of Oceanography

Circulation in estuaries is complicated by irregular bathymetric features such as branching basins, constrictions, islands, river mouths distributed along the coastline, multiple entrances, and shallow sill areas. This dissertation examines the dynamics within complex fjord-type estuaries and their exchange with the coastal ocean. A combination of realistic and idealized numerical models is used to provide descriptive results and generalizable insights.

In Chapter 2, output from a realistic numerical ocean model is used to study mixing in the Salish Sea. Salinity variance budgets are used to quantify the mixing in different regions within the estuary and to evaluate the importance of numerical mixing in the model. The timing of mixing in the Salish Sea is found to be tightly coupled to the river flow, and mixing hotspots are located at the river mouths. A simple approximation based on the river flow and the estuarine exchange flow salinities is shown to predict the total mixing in the Salish Sea and Puget Sound with good accuracy. Over a long time average, the exchange flow salt transport can also be used to estimate mixing in Puget Sound.

In Chapters 3 and 4, an ensemble of idealized models is used to study the effects of varying sill length and its ratio to the tidal excursion. Five idealized estuary models are developed with geometry loosely based on Puget Sound and its entrance sill at Admiralty Inlet, with sill lengths ranging from $5\ \mathrm{km}$ to $80\ \mathrm{km}$.

Chapter 3 seeks to characterize the mechanisms driving the estuarine exchange flow in estuaries with long and short sills. Three different salt transport decompositions are applied at cross sections along the sill

in the idealized estuary models. The behavior of salt transport over the spring-neap cycle is used to identify the dominant mechanism of exchange as either gravitational circulation or tidal pumping. At the ends of the sill, tidal pumping is found to be important regardless of sill length, whereas the middle of the sill develops a stronger gravitational circulation in the long sill models. A momentum balance analysis also supports these results. A transition from tidally-driven to gravitationally-driven exchange is shown to occur when the sill length exceeds the tidal excursion.

Chapter 4 investigates the relationship between sill length and estuarine residence times. The idealized model ensemble is used to conduct particle tracking experiments and construct box models of different regions of the estuary. Both approaches are used to calculate transport time scales representing retention in the estuary, as well as reflux coefficients, which quantify subtidal recirculation on the sill. Longer sills are found to produce greater retention in the inner basin of the estuary due to increased reflux and reentry from the sill region. The fate of particles on the sill is shown to be linked to the tidal cycle and the ratio of the sill length to the tidal excursion.

Acknowledgments

The research in this dissertation was funded by the U.S. National Science Foundation. Chapter 2 was supported by NSF Award 1736242 “Using Salinity Variance to Link Estuarine Mixing and Exchange Flow." Chapters 3 and 4 were supported by NSF Award 2122420 “Beyond salt: Effects of estuarine circulation and mixing timescales on biogeochemistry". Chapters 2 and 4 are coauthored by Parker MacCready. Chapter 3 is coauthored by Parker MacCready and W. Rockwell Geyer.

This research took place on the ancestral territory of the Coast Salish peoples. I acknowledge with gratitude their stewardship of these lands and waters since time immemorial.

Many people have contributed to making this work a reality. First and foremost, I owe a debt of gratitude to my advisor Parker MacCready, who has always been deeply invested in my training and development as a scientist and researcher. Thank you for introducing me to estuaries, helping me to build my confidence and independence, supporting me in achieving my goals, and always being excited about our new results. Thank you to my committee members, Alison Gray, Jodi Young, Andrea Ogston, Rocky Geyer, Christie Hegermiller, and Michelle DiBenedetto for their guidance over the years. I want to especially thank Rocky, who has been exceedingly generous with his time, ideas, and wealth of estuarine knowledge, and has played a big part in shaping this work into what it is today. The advice and encouragement that I received in Arthur Nowell’s graduate writing workshop was instrumental in completing Chapter 4.

I have the utmost admiration and appreciation for my colleagues in the UW Coastal Modeling Group, past and present: Elizabeth Brasseale, Hally Stone, Kate Hewett, Jilian Xiong, Dakota Mascarenas, and Aurora Leeson. I have deeply enjoyed our conversation, camaraderie, and adventures together. In particular, I want to thank Kate, who has been a role model, mentor, and friend since we met at Friday Harbor when I was just starting out in this field.

I have been fortunate to spend my time in graduate school surrounded by bright, hardworking, and kind people, including my 2018 Oceanography cohort and the graduate student community as a whole, the UW Environmental Fluid Mechanics group, and classmates in the 2019 Estuarine and Coastal Fluid Dynamics Summer School at Friday Harbor and 2023 Fluid Dynamics of Sustainability and the Environment Summer School at Cambridge. Thank you to my union, UAW 4121, and particularly the International Solidarity Working Group, for their support and collaboration through the years. My fun officemates in OSB 331, Katy Christensen, Zho Ragen, Laura Crews, Jade Sauvé, Stevie Walker, and Sarah Lang, (and honorable mention LuAnne Thompson), make me excited to come to campus. A special shoutout to Katy for providing me with this LaTeX template at the crucial moment! My PhD journey has been greatly enriched by my best physical oceanography pal, fellow Canadian Jade Sauvé, who has been there since Day 1. I cherish the countless hours we've spent at the office and out in the world, learning together and motivating each other, and I am grateful to have made a lifelong friend.

Finally, I want to thank my other wonderful friends here in Seattle, back home, and around the world, for their encouragement and for always giving me something to look forward to, even during difficult times. Thank you to my family, and especially my parents, Jillian and Trevor, for their love and support, and for always cheering me on. Last but certainly not least, thank you to Keir and Phoebe, who have been there for me every step of the way. I couldn't have done this without you.

Contents

List of Figures

List of Tables

There is a tide in the affairs of men

Which, taken at the flood, leads on to fortune;

Omitted, all the voyage of their life

Is bound in shallows and in miseries.

On such a full sea are we now afloat;

And we must take the current when it serves,

Or lose our ventures.

WILLIAM SHAKESPEARE
Julius Caesar

Chapter 1

Introduction

Estuaries are highly productive ecosystems, generating organic matter at a greater rate than comparably-sized areas of forest, grassland, or agricultural land [U.S. Environmental Protection Agency]. The astounding amount of biological activity in these transitional environments is facilitated by the mixture of river and ocean water and the nutrients they provide. Moreover, constant exchange between estuaries and the coastal ocean continually renews the water within them, replenishing oxygen and nutrients while flushing out pollutants.

A defining property of estuaries is the existence of an estuarine exchange flow, which is a persistent, subtidal circulation that exchanges water and tracers with the coastal ocean. The traditional conception of the exchange flow is a two-layer gravitational circulation, which draws salty ocean water into the estuary at depth and returns brackish water at the surface. The development of such an exchange flow requires input of fresh water, usually delivered by rivers, which is diluted through turbulent mixing, typically performed by the tides. The resulting estuarine circulation is often significantly larger than the incoming river flow. Other mechanisms are also capable of generating exchange between the estuary and ocean. For example, tidal pumping relies on differences in the flow structure between the ebb and flood tides to preferentially bring saltier water into the estuary and expel fresher water out of the estuary.

In studying the dynamics of estuaries, we often concentrate our attention on salinity and salt transport. Salt is a conservative tracer and the primary source of density differences in estuaries, much more so than temperature. We use these attributes to our advantage in several analysis methods. For example, the de-

struction of salinity variance can be used to quantify the irreversible process of turbulent mixing [Burchard and Rennau, 2008]. The spatial and temporal organization of salt flux through a cross section of the estuary may be used to infer the mechanisms responsible for exchange [Lerczak et al., 2006; Dronkers and van de Kreeke, 1986]. Alternatively, the Total Exchange Flow (TEF), which combines the contributions of various physical processes, can be found by grouping transports based on their salinity class [MacCready, 2011]. Salt conservation in box models can be used to calculate vertical mixing and transport between layers of the exchange flow using efflux-reflux theory [Cokelet and Stewart, 1985; MacCready et al., 2021]. Despite the popularity of salinity-based approaches, strategies that do not directly consider salinity information are also available, such as dye releases and Lagrangian particle tracking experiments.

The three projects presented in this dissertation are motivated by a desire to understand our local estuary: Puget Sound and the wider Salish Sea. The inland waters of Washington State and southwestern British Columbia form the Salish Sea, a large fjord-type estuarine system encompassing the Strait of Juan de Fuca, Strait of Georgia, and Puget Sound. The Salish Sea is home to over eight million (human) inhabitants [The SeaDoc Society] and provides valuable environmental and economic benefits to the region. However, the ecosystem also faces challenges due to increasing hypoxia, ocean acidification, and other threats to water quality such as oil spills, accumulating microplastics, and polluted land-based runoff. The prevalence and persistence of these problems is moderated by physical processes in the estuary.

The Salish Sea's network of interconnected basins, sills, constrictions, numerous rivers and streams, and other irregular elements means that understanding these processes is not straightforward. This dissertation seeks to develop new insights into the factors controlling mixing, exchange flow mechanisms, and residence times in estuaries with complex bathymetry. Our research questions lend themselves to a combination of realistic and idealized modeling approaches. With realistic modeling, we can incorporate the full extent of bathymetric complexity and variable external forcing. This provides us with informative, descriptive results specific to our local study region, with implications for how things might change in the future. At the same time, it can be difficult to isolate the influence of any given bathymetric feature in a system with so many simultaneous interactions. To address this problem, we use idealized models, which allow us to perform controlled experiments varying a single bathymetric parameter. The results from the idealized modeling studies are also easier to generalize, improving our ability to make predictions about other estuaries where

detailed models and/or observations are not available. In the work that follows, we focus on sills, and particularly, the effects of varying sill length relative to the tidal excursion. The prototype for the idealized models is Admiralty Inlet, the entrance sill to Puget Sound.

The remainder of this dissertation is organized into three main chapters. In Chapter 2, we use destruction of salinity variance to uncover where and when mixing occurs in the Salish Sea. We use output from a realistic numerical model of the coast of Oregon, Washington, and southern British Columbia called LiveOcean to construct salinity variance budgets for the Salish Sea, Puget Sound, and smaller basins within, for the years 2017-2019. We also produce maps showing the spatial variability of mixing on a finer scale. To find out when mixed water is produced, we correlate the time series of mixing in each basin with three external forcing factors: tidal amplitude, river flow, and wind strength. A complementary property to salinity variance, mixedness, is introduced to represent removal of mixed water from the estuary in a similar correlation analysis. Finally, we test the performance of two theoretical expressions for time-averaged, basin-wide mixing against our model results.

In Chapter 3, we develop an ensemble of idealized models inspired by the geometry of Puget Sound, but with varying sill length. We examine the dependence of estuarine exchange flow mechanisms on the sill length to tidal excursion ratio using three salt flux decompositions: the Total Exchange Flow (TEF), the standard Eulerian decomposition, and the Dronkers and van de Kreeke decomposition. Together these decompositions provide information about spatial variations in the dominant exchange flow mechanism along the sill, as well as differences in behavior between long and short sills. In addition, we calculate momentum balances for the inflowing and outflowing layers of the exchange flow as defined by the TEF decomposition, and compare the primary force balances to expectations for gravitational circulation and tidal pumping. We also consider the along-channel salinity gradient, which is important for understanding the observed salinity in the inner basin as well as the baroclinic pressure gradient that is required for gravitational exchange.

Chapter 4 uses the same idealized model ensemble as Chapter 3. We use Lagrangian particle tracking experiments in the five models to determine how sill lengths affect residence times in the inner basin and the estuary as a whole. We calculate e-folding times, which are based on bulk counts of particles remaining in the domain, as well as exposure and strict residence times, which are local measures specific to the particle's

point of release. We also use the exchange flow transports from the TEF method to calculate flushing times, another transport time scale. The importance of reentry and reflux in increasing retention is explored by comparing these different time scales. We follow the procedure of Cokelet and Stewart [1985] to determine the amount of reflux which occurs on the sill, and also compare with estimates calculated directly from the tidally-averaged particle tracks. In addition, we propose a time-dependent version of the efflux-reflux formulas, which accounts for storage of salt in the sill region. Lastly, we examine the trajectories of particles during their visits to the sill to understand the conditions that foster and inhibit particle return.

Finally, Chapter 5 presents conclusions and suggests possible avenues for future research.

Chapter 2

Mixing in a salinity variance budget of the Salish Sea is controlled by river flow

This chapter has been published as: Broatch, E. M., and P. MacCready, 2022: Mixing in a salinity variance budget of the Salish Sea is controlled by river flow. Journal of Physical Oceanography, 52 (10), 2305 – 2323, https://doi.org/10.1175/JPO-D- 21-0227.1.

Abstract

A salinity variance framework is used to study mixing in the Salish Sea, a large fjordal estuary. Output from a realistic numerical model is used to create salinity variance budgets for individual basins within the Salish Sea for 2017-2019. The salinity variance budgets are used to quantify the mixing in each basin and estimate the numerical mixing, which is found to contribute about one-third of the total mixing in the model. Whidbey Basin has the most intense mixing, due to its shallow depth and large river flow. Unlike in most other estuarine systems previously studied using the salinity variance method, mixing in the Salish Sea is controlled by the river flow and does not exhibit a pronounced spring-neap cycle. A "mixedness" analysis is used to determine when mixed water is expelled from the estuary. The river flow is correlated with mixed water removal, but the coupling is not as tight as with the mixing. Because the mixing is so highly correlated with the river flow, the long-term average approximation $M = Q_r s_{out} s_{in}$ can be used to predict the mixing in the Salish Sea and Puget Sound with good accuracy, even without any temporal averaging. Over a three-year average, the mixing in Puget Sound is directly related to the exchange flow salt transport.

2.1 Introduction

A defining feature of estuaries is the exchange flow, which draws ocean water into the estuary at depth and expels brackish water near the surface. Two factors are required for the development of an exchange flow: a source of buoyancy, and mixing [MacCready et al., 2018]. Typically the buoyancy is supplied by rivers, although other sources such as strong precipitation are also possible, and mixing is provided primarily by tides.

Historically, mixing in estuaries has been quantified using buoyancy flux (e.g. Peters and Bokhorst 2001; Simpson et al. 1990), which is a measure of potential energy creation through the destruction of vertical stratification. However, buoyancy flux does not incorporate the effects of horizontal mixing. Moreover, the buoyancy flux for convective mixing and shear-driven mixing will have opposite signs, such that these two mixing modes may cancel each other's contribution to the overall buoyancy flux [Burchard et al., 2009; MacCready et al., 2018; Burchard et al., 2019]. Other measures of mixing used in the open ocean such

as the turbulent dissipation are important, but not directly useful, in estuarine and coastal environments. Dissipation destroys kinetic energy through turbulence, but may not produce mixing if the water is already well-mixed. Similarly, the eddy diffusivity alone is not a suitable measure of mixing, since the mixing also depends on the strength of salinity gradients in the estuary.

More recently, destruction of salinity variance has been used to quantify mixing in estuaries, although loss of tracer variance has been used to define mixing in the ocean turbulence field for many decades [Wang and Geyer, 2018]. Burchard and Rennau [2008] showed that tracer variance decay is a physically sound measure of mixing equivalent to the dissipation of micro-structure variance. Salt is an appropriate tracer to choose since it is a conservative tracer and the main driver of density differences in estuarine environments. Therefore, loss of salinity variance is an unambiguous measure that represents irreversible mixing [MacCready et al., 2018; Warner et al., 2020].

Burchard et al. [2009] used both the vertically integrated decay of salinity variance and the vertically integrated turbulent salt flux to quantify mixing associated with dense bottom currents in the Western Baltic Sea. They found good qualitative agreement between the two methods for identifying mixing hotspots from model results, because convective mixing is relatively unimportant in the study region. An early study to use the dissipation of salinity variance to quantify mixing in an estuarine context was Wang et al. [2017]. Using a numerical model of the Hudson estuary, they found that the mixing is lowest at spring tide, and greatest in the neap-to-spring transition, even though the most energetic turbulence occurs during spring tides. This is because the estuary is restratified around neap tide, so the neap-to-spring transition period has intensified turbulence and strong salinity gradients, which are both required for mixing. Li et al. [2018] decomposed the salinity variance into horizontal and vertical components, which can be used to link four defining estuarine features. The horizontal variance represents horizontal density gradients (1), which provide a baroclinic pressure gradient that drives the exchange flow. The vertical variance represents stratification (2). The conversion from horizontal to vertical variance represents straining (3), and, as we have seen previously, the destruction of variance represents mixing (4). They used this framework to evaluate straining and dissipation in the Changjiang estuary.

MacCready et al. [2018] used salinity variance to connect mixing to the magnitude of the estuarine exchange flow. The Knudsen relations [Knudsen, 1900; Burchard et al., 2018] relate the magnitude of a

time-averaged, two-layer exchange flow to the river flow through the salinities of the inflowing and outflowing layer. By combining the salinity variance budget with a time-dependent version of the Knudsen relations, MacCready et al. [2018] established an approximation for the total mixing using the Total Exchange Flow (TEF) variables. Over a long-term average, such that the storage term in the salinity variance budget becomes small relative to the advection and mixing terms, this approximation can be reduced to a simple relationship $M = Q_r s_{out} s_{in}$, where M is the volume-integrated rate of salinity variance destruction (mixing), Q_r is the river flow and s_{in} and s_{out} are the inflowing and outflowing salinities, respectively, for an equivalent two-layer exchange flow. Alternatively, this can be expressed as $M = Q_{in} \Delta s \, s_{in}$, where Q_{in} is the magnitude of the inflowing branch of the exchange flow and $\Delta s = s_{in} - s_{out}$. This formulation links the mixing in an estuary to the strength of its exchange flow, represented by Q_{in}, albeit with some ambiguity, since the mixing also affects Δs. MacCready et al. [2018] used an idealized model which, similarly to Wang et al. [2017], shows that mixing peaks just after neap tide. Wang and Geyer [2018] used the salinity variance method to study the effects of varying river flow and the spring-neap cycle on mixing and the exchange flow in the Hudson estuary. By running their numerical model with different levels of constant river discharge, they found that increased river flow leads to increased mixing in the estuary.

Another useful application of salinity variance is that it can be used to diagnose the numerical mixing in a model. Numerical mixing is often overlooked in ocean models, but can significantly impact model results [Ralston et al., 2017]. Coarse model grid sizes, sharp gradients, high fluid velocities, and steep bathymetry are factors that may lead to intensified numerical mixing [Ralston et al., 2017], in addition to the choice of advection scheme. As described in Burchard and Rennau [2008], the numerical mixing, defined as the loss of tracer variance due to discretization errors, is equal to the decay rate between the advected square of the tracer and the square of the advected tracer. This method can be used to calculate the numerical mixing in a model on a cell-by-cell basis. Alternatively, the volume-integrated numerical mixing can be estimated as the residual of a salinity variance budget [MacCready et al., 2018], which is appropriate when the model output data capture typical flow timescales [Wang et al., 2021]. The volume-integrated numerical mixing can also be calculated from the diahaline diffusive salt flux and volume-integrated salinity variance dissipation, as described in Wang et al. [2017].

Most of the studies described above used idealized models or models of shallow coastal plain estuaries.

We will use the salinity variance framework to study mixing in the Salish Sea, a complex fjordal estuary. The Salish Sea is an inland sea in British Columbia and Washington which comprises the Strait of Juan de Fuca, Strait of Georgia, and Puget Sound.

The Salish Sea is substantially different from other estuaries previously studied using salinity variance. It is a large, deep fjordal estuary carved by glaciers, with a surface area of approximately $17000\ \mathrm{km}^2$ and depths exceeding $400\ \mathrm{m}$ in the Strait of Georgia (The SeaDoc Society). The Salish Sea is a complex network of interconnected basins, with over 400 islands. Unlike most estuaries, many rivers of varying sizes feed the Salish Sea, and are distributed along its coastline. It is filled with mostly ocean water and therefore very salty, with a mean salinity over $30\ \mathrm{g\ kg}^{-1}$ in 2017-2019. In many regards, the Salish Sea lacks resemblance to simpler estuaries such as the Hudson River. Despite these differences, it still develops one of the largest estuarine exchange flows on the planet [MacCready et al., 2021] and has many qualities characteristic of estuarine systems.

In Section 2.2, we will outline the theory behind the salinity variance framework, as well as the related concept of mixedness. In Section 2.3, we will describe the model and methods used to construct the salinity variance budget, as well as the calculation of mixedness and time series of external forcing factors. Our main goals are to use salinity variance to answer the questions:

- Where and when is mixed water created in the Salish Sea?
- When is mixed water removed from the estuary?
- How well does the long-term average mixing approximation perform in the Salish Sea and Puget Sound?
- How important is numerical mixing in the model?

In Section 2.4 we will discuss the results pertaining to these questions. In Section 2.5 we will summarize conclusions.

2.2 Theory

2.2.1 Salinity variance

The salinity variance in a given volume V is defined as

$$\text{var}(s) = \int_V s'^2 dV \tag{2.1}$$

where $s' = s - \bar{s}$, with s being the local salinity and $\bar{s}$ being the mean salinity in the volume. We will call s'^2 the "local salinity variance," acknowledging that while the variance is only defined as a single statistic for the entire volume, s'^2 determines the local contribution to the overall variance when volume-integrated. Following MacCready et al. [2018] we start with a salt budget:

$$\frac{\partial s}{\partial t} + \boldsymbol{u} \cdot \nabla s = \nabla \cdot (\boldsymbol{K} \cdot \nabla s) \tag{2.2}$$

where $\boldsymbol{u} = (u, v, w)$ is the velocity, and $\boldsymbol{K} = (K_H, K_H, K_V)$ is the eddy diffusivity, with horizontal eddy diffusivity K_H and the vertical eddy diffusivity K_V. Expanding $s = \bar{s} + s'$ and multiplying both sides by $2s'$, we obtain an equation for the evolution of local salinity variance:

$$\frac{\partial}{\partial t}(s'^2) + \boldsymbol{u} \cdot \nabla(s'^2) = \nabla \cdot (\boldsymbol{K} \cdot \nabla(s'^2)) - 2\boldsymbol{K} \cdot (\nabla s')^2 - 2s' \frac{\partial \bar{s}}{\partial t} \tag{2.3}$$

where here we use $(\nabla s')^2$ to denote the vector $((ds'/dx)^2, (ds'/dy)^2, (ds'/dz)^2)$. Now we take the volume integral over the entire estuarine volume V and apply the Reynolds transport theorem. Assuming incompressible flow and that the diffusive transport of salinity variance across the open boundaries is negligible compared to the advective transport, we arrive at the equation for the salinity variance budget:

$$\boxed{\frac{d}{dt} \int_V s'^2 \, dV = - \int_A s'^2 \boldsymbol{u} \cdot \hat{\boldsymbol{n}} \, dA - 2 \int_V \boldsymbol{K} \cdot (\nabla s')^2 \, dV} \tag{2.4}$$

The term on the left-hand side represents the time evolution of the variance, and the terms on the right-hand side represent the effects of advection and mixing, which is a sink for variance.

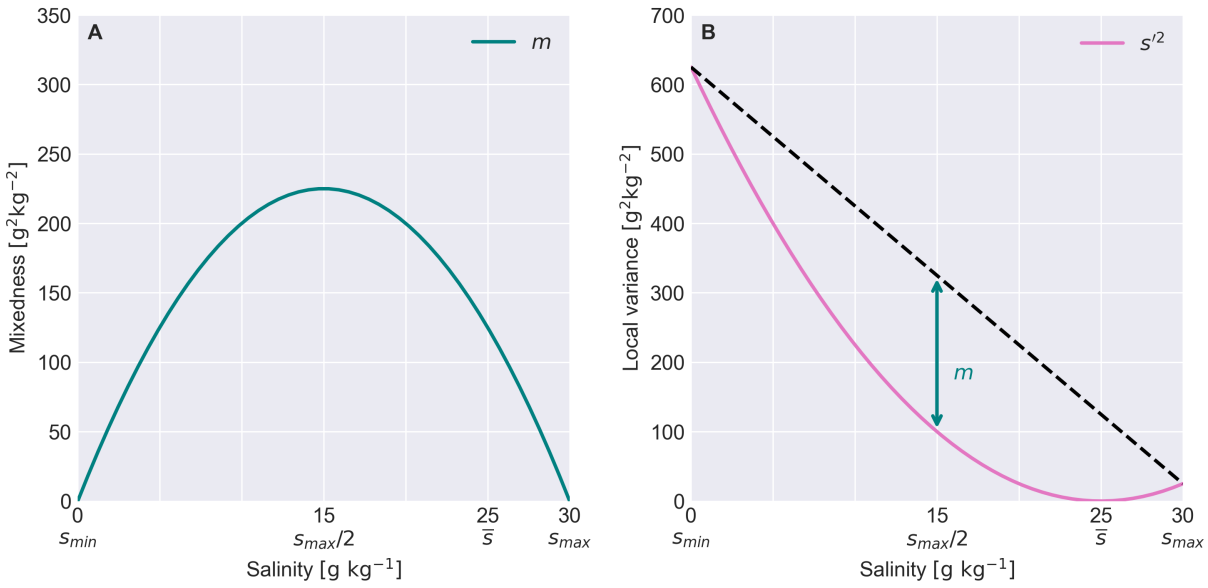

Figure 2.1: Example graph explaining mixedness concept (A) and its relationship to salinity variance (B) for a scenario with $s_{max} = 30$, $s_{min} = 0$, and $\bar{s} = 25$. Note that $\bar{s} \neq s_{max}/2$. Since $\bar{s}$ is close to s_{max}, the local variance in this scenario is greatest for the freshwater rivers. This is similar to the situation in the Salish Sea.

2.2.2 Mixedness

A complementary property to the salinity variance is the mixedness m. We define the mixedness as

$$m = (s_{max} - s)(s - s_{min}) \tag{2.5}$$

where s_{max} and s_{min} are the maximum and minimum salinities, respectively. For an estuary it can be assumed that $s_{min} = 0$ since the river input is freshwater. Therefore we have

$$m = s_{max}\, s - s^2 \tag{2.6}$$

Figure 2.1 shows graphically how mixedness and salinity variance are related for an example scenario. The mixedness is zero for the two endmembers s_{max} and s_{min}, and has its peak at $s_{max}/2$, while the variance is zero at the mean salinity $\bar{s}$ and increases away from the mean. Because we will generally not have $s_{max}/2 = \bar{s}$, it may not be possible to achieve the maximum mixedness $s_{max}^2/4$ everywhere, even in a volume that is fully homogenized where the salinity variance is zero. In the Salish Sea, similarly to

Figure 2.1, the mean salinity is closer to the oceanic salinity than to the freshwater rivers. If we consider truly "mixed" water to have salinity $\bar{s}$, the mixedness m is not a perfect measure unless the mixing involves equal amounts of the fresh and salty endmembers. However, because the mixedness curve varies gradually around its maximum, the overall mixedness will still increase as the salinity variance decreases. By combining a salt budget with a salt-squared budget we may construct a mixedness budget:

$$\frac{d}{dt}\int_V m\, dV = -\int_A m\boldsymbol{u}\cdot\hat{\boldsymbol{n}}\, dA + 2\int_V \boldsymbol{K}\cdot(\nabla s')^2\, dV \tag{2.7}$$

Note that the last term is the same mixing term present in the salinity variance budget, except that it is positive and acts as a source of mixedness.

2.3 Methods

2.3.1 Model overview

The model used is a realistic simulation of the coastal waters of Oregon, Washington, and southern British Columbia called LiveOcean, created by the University of Washington Coastal Modeling Group. A description of the model and its validation can be found in MacCready et al. [2021]. The model is built using the Regional Ocean Modeling System (ROMS), and uses a spherical grid in the horizontal, with grid lines along constant latitudes and longitudes. The cell dimensions vary from 500m in the Salish Sea to 1500m offshore. The model has 30 s-coordinate terrain-following vertical layers, which are more closely spaced near the surface and sea floor to better resolve boundary effects. The time step is 40 seconds.

For external forcing, the model includes 45 rivers, with data from USGS and Environment Canada flow gauges. Atmospheric forcing is provided by a regional Weather Research and Forecasting (WRF) model. The open ocean boundary is forced by the HYbrid Coordinate Ocean Model (HYCOM) and eight tidal constituents from the TPXO tide model. We use the output of a three-year hindcast for 2017-2019, with history files which record the instantaneous model fields at hourly intervals.

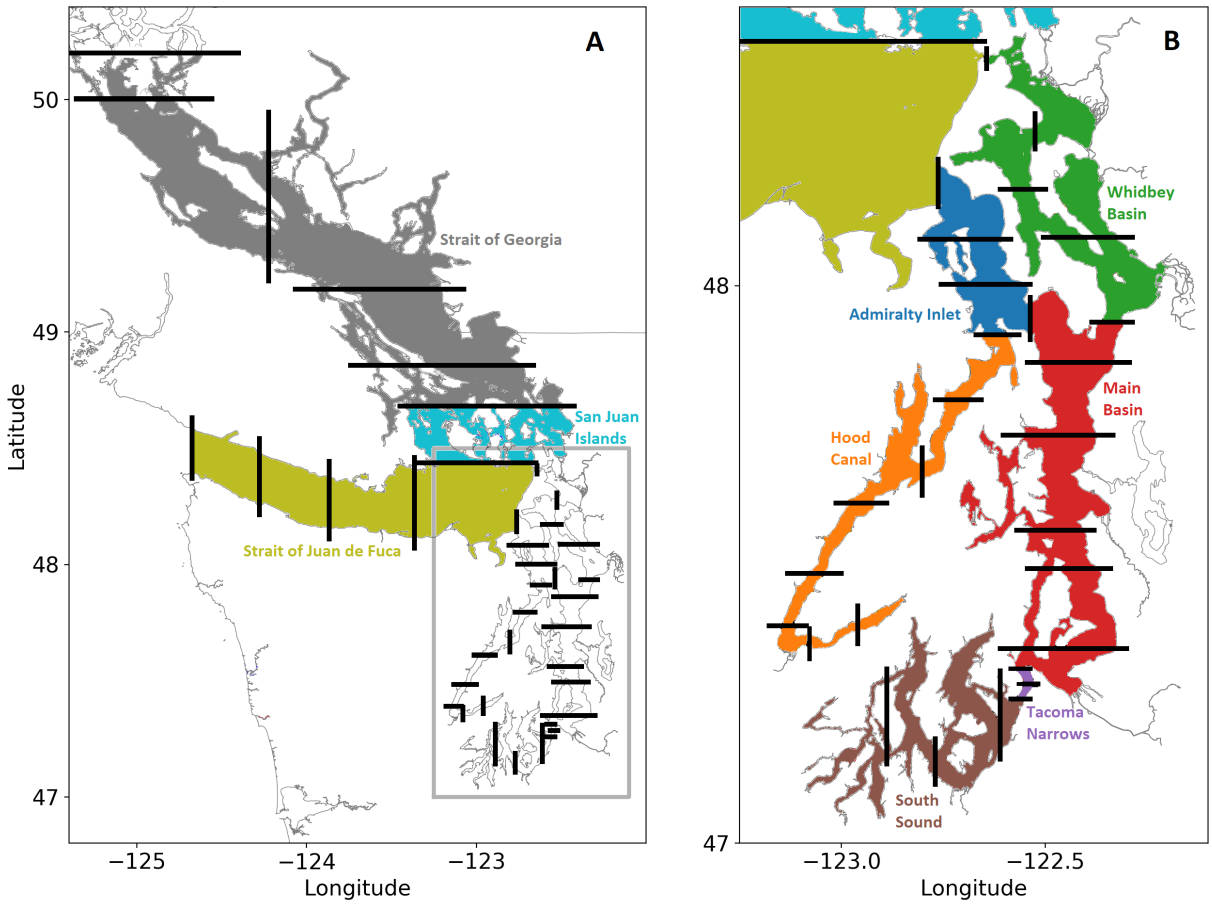

Figure 2.2: Map showing the nine basins used in this project (A), with inset map of Puget Sound (B). The bold black lines are the sections dividing the smaller volume segments used in MacCready et al. [2021]. Adapted from MacCready et al. [2021].

2.3.2 Basins

We divide the Salish Sea into nine different basins: South Sound, Tacoma Narrows, Main Basin, Hood Canal, Whidbey Basin, Admiralty Inlet, the San Juan Islands, the Strait of Juan de Fuca, and the Strait of Georgia. Salinity variance budgets can be made for any of these individual basins, which requires calculating s' using the mean salinity within the individual basin volume. We will also occasionally consider Puget Sound, which consists of the first six basins listed, as well as the Salish Sea as a whole. To divide the model domain into these basins we use the same framework as MacCready et al. [2021], but group together several of the smaller volume segments in each basin, as shown in Figure 2.2.

2.3.3 Diagnostic budgets

In the LiveOcean model, we can choose to save the ROMS diagnostics and averages files at hourly intervals, in addition to the hourly history (snapshot) files. The averages files, given on the half-hour, record the average of the model fields over every time step within the hour. The diagnostics files record information about how the model behaves internally. The diagnostics fields contain the rates of change of water properties in each cell due to various processes resolved in the model. These rates of change are an average over the hour, quoted on the half-hour.

Starting with a salt budget for a single cell made up of diagnostics terms, we follow a procedure similar to Section 2.2.1 to construct an exact salinity variance budget with a vanishingly small residual. Details of the derivation can be found in Appendix A. The diagnostics salinity variance budget equation is

$$\int_V 2s' \left[\texttt{salt\_rate} - \frac{s}{\delta}\frac{\partial \delta}{\partial t} \right] dV = \int_V 2s' \left[\texttt{salt\_xavd} + \texttt{salt\_yavd} + \left(\texttt{salt\_vavd} - \frac{s}{\delta}\frac{\partial \delta}{\partial t} \right) \right] dV + \int_V 2s' \left[\texttt{salt\_hdiff} + \texttt{salt\_vdiff} \right] dV \quad (2.8)$$

where the left-hand side represents storage, the first term on the right-hand side represents advection, and the second term on the right-hand side represents mixing. This is of the same form as the salinity variance

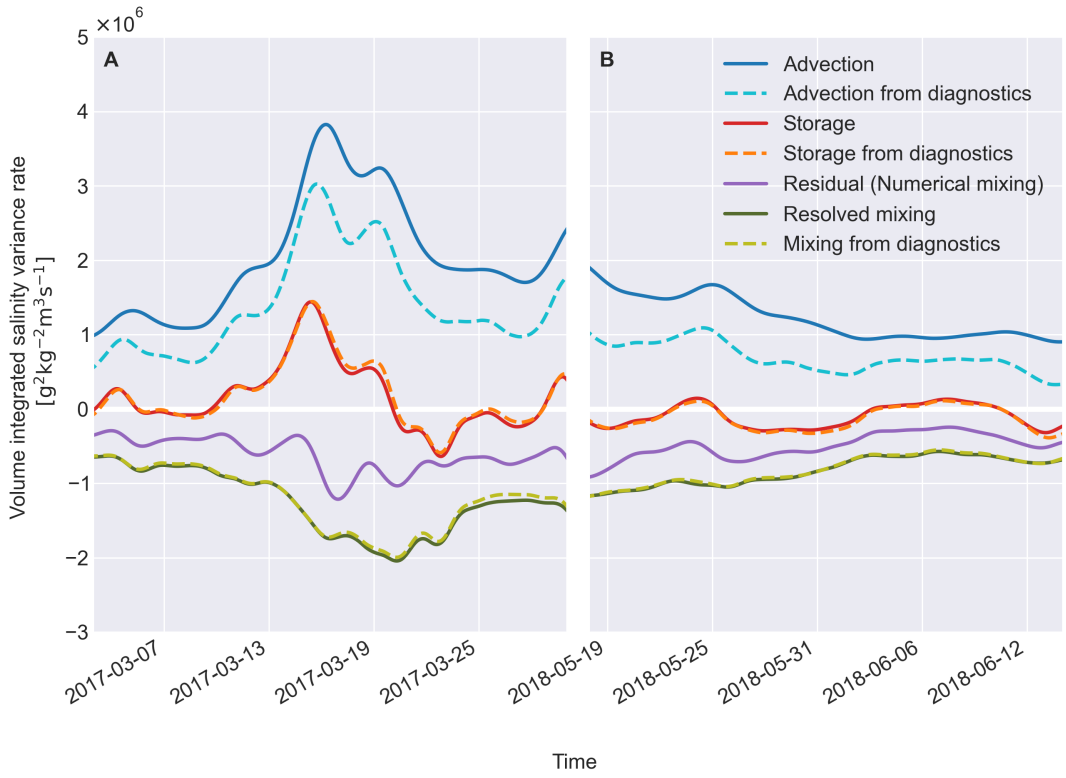

Figure 2.3: Comparison of terms from history and diagnostic budgets for Puget Sound in March 2017 (A) and May/June 2018 (B). The history budgets have a residual due to numerical mixing which is the cause of the large difference between the history and diagnostic advection terms.

budget given in Equation 2.4, although here we calculate the advection term using a volume integral instead of invoking the Reynolds transport theorem to calculate the advective transport through the open boundaries. `salt_xavd`, `salt_yavd`, and `salt_vavd` are diagnostics fields that give the rates of change due to advection in the x, y and z directions, respectively, and `salt_hdiff` and `salt_vdiff` are diagnostics that give the rates of change due to horizontal and vertical diffusion, respectively. `salt_rate` is the total rate of change in the salt content of the model cell, and δ is the cell thickness, which changes over time.

The advantage of using the diagnostics to form salinity variance budgets is that the budget closes exactly on a cell-by-cell basis, so a volume-integrated budget will close with no residual. Figure 2.3 shows an example of diagnostic budgets for Puget Sound (alongside budgets constructed from the history files which will be covered in Section 2.3.4). The diagnostic budgets have been tidally-averaged using a Godin filter

[Godin, 1972; Walters and Heston, 1982]. The advection term is positive since river and ocean inflow bring salinity variance into the estuary, while the outflow of mixed water removes a small amount of variance. Most of the variance that is imported through advection is destroyed by mixing.

It is important to note that the diagnostics budgets do not include the effects of numerical mixing, consistent with the numerical mixing method outlined in Burchard and Rennau [2008]. Nonetheless, the diagnostic budgets are useful for validating salinity variance budgets calculated from the history files alone by comparing their storage, horizontal mixing, and vertical mixing terms.

2.3.4 Three-year salinity variance budgets

To make salinity variance budgets over the three years of our model hindcast, we need to estimate the storage, mixing, and advection terms from the history files. The storage term can be estimated by calculating the mean salinity for the chosen volume at every hour to create a time series of total salinity variance in the basin. We then use centered differencing to find the rate of change, and filter the time series with a Godin filter. To estimate the mixing term, we calculate the resolved mixing using Equation 2.4:

$$M_{resolved} = 2 \int_V \boldsymbol{K} \cdot (\nabla s')^2 \, dV \tag{2.9}$$

We can split the resolved mixing into vertical and horizontal components, M_V and M_H:

$$M_V = 2 \int_V K_V \left(\frac{ds}{dz} \right)^2 \, dV \tag{2.10}$$

$$M_H = 2 \int_V K_H \cdot (\nabla_H s)^2 \, dV \tag{2.11}$$

where ∇_H is the horizontal gradient operator, K_V is the vertical eddy diffusivity, and K_H is the horizontal eddy diffusivity, which is a constant ($2.0 \ \mathrm{m^2 s^{-1}}$). To calculate the horizontal gradients, we use simple centered differencing along the terrain-following layer, neglecting layer height variations. By comparing our results to the diagnostic budgets, we determined that applying a correction to account for the slope of the layer resulted in worse performance, likely due to discretization errors.

The last term that we need to estimate is the advection term. We use the Total Exchange Flow (TEF)

[MacCready, 2011] to find the tidally-averaged advection as a sum of three terms: a river term, and inflowing and outflowing terms representing an equivalent two-layer flow at the open boundaries. The TEF method decomposes the flow through a section in salinity coordinates into an equivalent two-layer exchange flow Q_{in} and Q_{out} [MacCready, 2011]. To find the total exchange flow, flow through a section is binned according to its salinity class, tidally-averaged, and then grouped into inflowing and outflowing layers. We use 1000 salinity classes with the dividing salinity method described in Lorenz et al. [2019], which is more numerically robust, to find Q_{in} and Q_{out} at the bounding sections of each basin. The flux-weighted salinities of the inflow and outflow, denoted by s_{in} and s_{out}, respectively, can then be found from the salt flux in each layer. We can also find the flux-weighted s_{in}^2 and s_{out}^2 at each section. We then use these known quantities to efficiently calculate the flux-weighted salinity variance at each section:

$$s_{in}'^2 = s_{in}^2 - 2s_{in}\bar{s} + \bar{s}^2 \tag{2.12}$$

$$s_{out}'^2 = s_{out}^2 - 2s_{out}\bar{s} + \bar{s}^2 \tag{2.13}$$

This is advantageous because performing the TEF extractions is computationally expensive. We want to create salinity variance budgets for eleven individual basins, each with a different mean salinity. This method allows us to find the $s_{in}'^2$ and $s_{out}'^2$ for a given mean salinity without actually extracting the fluxes of s'^2 through each section. We can then use the $s_{in}'^2$ and $s_{out}'^2$ to form the advection term for a salinity variance budget:

$$-\int_A s'^2 \boldsymbol{u} \cdot \hat{\boldsymbol{n}}\, dA = Q_r \bar{s}^2 + Q_{in} s_{in}'^2 + Q_{out} s_{out}'^2 \tag{2.14}$$

where Q_r is the river flow and Q_{out} is defined as being negative. This is similar to the formulation given in Equation 33 of Burchard et al. [2019], except that the covariance between the river flow and the mean salinity is not included.

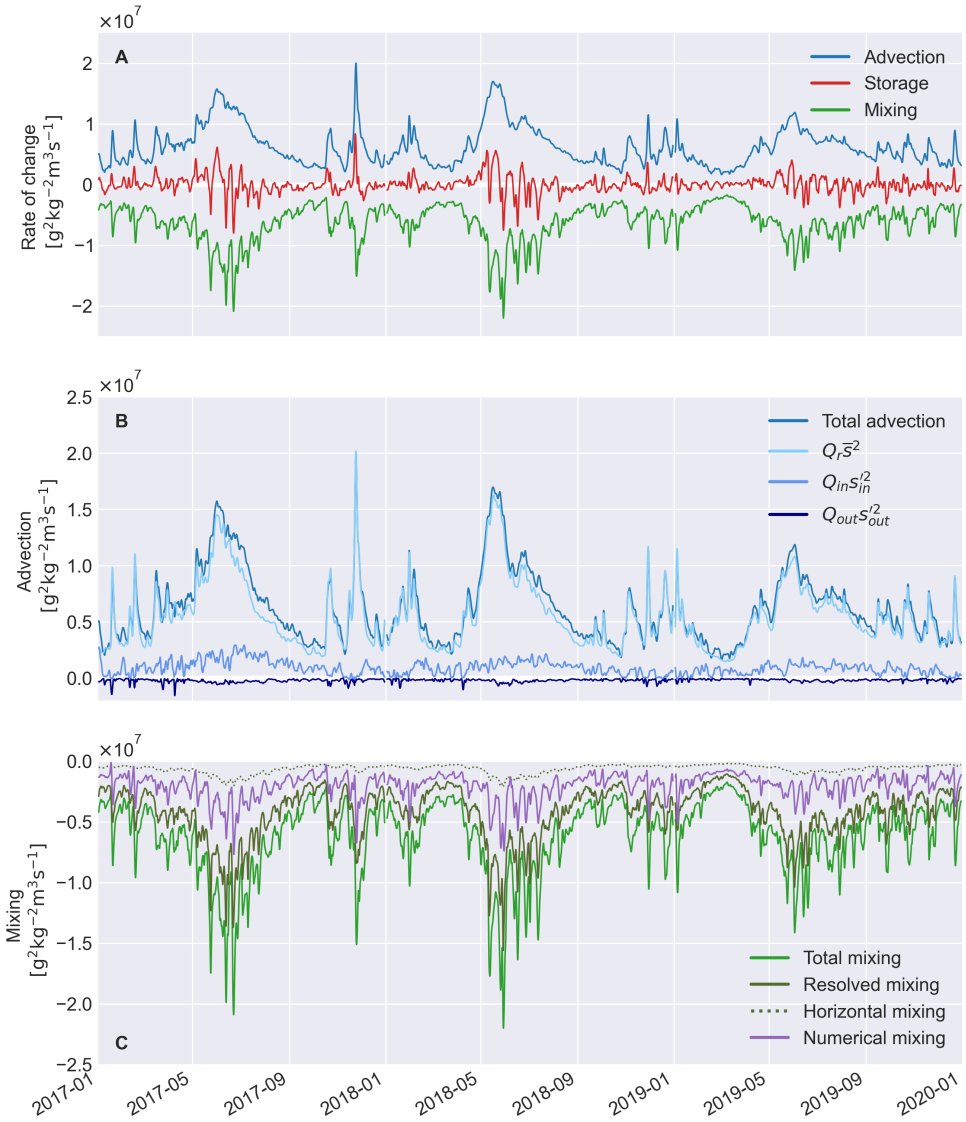

Figure 2.4: Salinity variance budgets for 2017-2019 calculated from history files in the Salish Sea (A). This budget closes by construction since the residual (estimated numerical mixing) is grouped into the mixing term. Breakdown of the advection term from the Salish Sea salinity variance budget into river, inflow and outflow components (B). Breakdown of the mixing term from the Salish Sea salinity variance budget (C). The total mixing is the sum of the resolved and numerical mixing. The horizontal mixing is a component of the resolved mixing.

We can categorize the basins as “enclosed" or “non-enclosed" based on whether the flow at all of its bounding sections is in the same direction. For the “enclosed" basins, such as Whidbey Basin, flow into the basin (Q_{in}) is in the “landward" direction at all openings. For enclosed basins with more than one bounding section we can combine the Q_{in} or Q_{out} from openings and find a single combined flux-weighted value of $s_{in}'^2$ and $s_{out}'^2$ for the basin. For the “non-enclosed” basins, such as Tacoma Narrows, flow into the basin is “landward" at some openings and “seaward" at others. In this case, the TEF variables must be kept separate for each boundary. In such cases, calculating a combined value for $s_{in}'^2$ or $s_{out}'^2$ yields little physical insight.

Figure 2.3 shows the three terms (storage, mixing and advection) calculated from the diagnostics and history files for Puget Sound for the two months where the diagnostics are available. As expected, the advection term is much larger in the history budgets due to the effects of numerical mixing. The residual from the history budgets, shown in purple, is an estimate of the numerical mixing. As shown in Figure 2.3, the resolved mixing and storage terms calculated using the history files are very similar to the the mixing and storage from the diagnostic budgets. We have also previously used the history files to construct volume and salt budgets (not shown) that close with a small residual, which implies that our advection calculation method is sound. Therefore, we can be reasonably confident that the residual is primarily due to numerical mixing and not other errors.

Now we can use the history budget method to construct salinity variance budgets for the full three years 2017-2019. The salinity variance budget for the Salish Sea using the history budget method is shown in Figure 2.4, where the resolved mixing and estimated numerical mixing have been grouped together. We refer to the sum of the resolved and numerical mixing as the total mixing. Figure 2.4 also shows the breakdown of the total advection into its TEF components. Even though the river flow is much smaller than the exchange flow, the river contribution dominates the advection term in the salinity variance budget because the fresh river water has very high variance. The inflowing exchange flow term is slightly larger than the outflowing term, even though Q_{in} and Q_{out} have very similar magnitudes, because s_{out} is close to $\bar{s}$. The bottom panel of Figure 2.4 shows the breakdown of the total mixing into resolved and numerical mixing, along with the horizontal contribution to the resolved mixing. We also create salinity variance budgets for all nine smaller basins shown in Figure 2.2, as well as Puget Sound, and the mixing terms from these budgets will be used to answer our research questions.

2.3.5 Mixedness transport

Similarly to Section 2.3.4, we can write the mixedness budget in terms of the TEF variables:

$$\frac{d}{dt}\int_V m\, dV = Q_{in}m_{in} + Q_{out}m_{out} + 2\int_V \boldsymbol{K}\cdot(\nabla s')^2\, dV \tag{2.15}$$

where there is no contribution from the freshwater rivers which have $m = 0$. The inflowing and outflowing mixedness m_{in} and m_{out} are calculated as

$$m_{in} = (s_{in})(s_{max}) - s_{in}^2 \tag{2.16}$$

$$m_{out} = (s_{out})(s_{max}) - s_{out}^2 \tag{2.17}$$

where we use the highest s_{in} in the three-year time series as s_{max}. It is necessary to use s_{out}^2 rather than $(s_{out})^2$ to obtain the correct flux-weighted mixedness.

To study when mixed water is expelled from the estuary, we use the outflowing mixedness transport $Q_{out}m_{out}$. We calculate time series of outflowing mixedness for six enclosed basins: the entire Salish Sea, Puget Sound, South Sound, Hood Canal, Whidbey Basin and the Strait of Georgia. Since the remaining basins do not have a well-defined Q_{out}, s_{out} and s_{out}^2 (see Section 2.3.4), they are excluded from this portion of the analysis.

2.3.6 Forcing factors

To study the timing of mixing, we look at the correlation with three forcing factors: rivers, tides and winds. For the rivers, we use the total river flow Q_r from all rivers entering a given segment. Since the forcing files for the model only have a single river flow value per day, the total river flow is smoothed with the Godin filter, consistent with the other budget terms and forcing factors. We use the surface current and surface wind stress to calculate the energy input from winds [Yu et al., 2018]:

$$P_{wind} = \int_A \boldsymbol{\tau_s}\cdot\boldsymbol{u_s}\, dA \tag{2.18}$$

where $\boldsymbol{\tau_s}$ is the surface wind stress and $\boldsymbol{u_s}$ is the surface current.

Because the quantities required are on different coordinates of the model grid, we interpolate the fields to the center of each cell using simple averaging. The area integral over the surface of the basin gives a rate of wind energy input to the ocean in watts. The time series of wind forcing is then filtered using the Godin filter. For the tides, we use the same method with the bottom velocities and bottom stress to calculate the energy dissipation due to bottom drag. Although the velocity right at the bottom is zero due to the no-slip condition, the stress and velocity in the bottom model cell can be used to calculate the energy dissipation in a layer just above the bottom. This is appropriate because we are using the tidally-averaged energy dissipation near the bottom as a timekeeper for the spring-neap cycle and not as part of an energy budget.

To study the correlation between the forcing factors and the mixing or mixedness transport, we use a lagged correlation (up to 15 days lag, in one hour increments) to find the maximum Pearson's correlation coefficient r.

2.4 Results and discussion

2.4.1 Numerical mixing

The different contributions to the total mixing term are shown in Figure 2.4 for the Salish Sea. Although the total resolved and numerical mixing balances the salinity variance budget, any conclusions drawn from the model output rely on whether the simulated total mixing is a good representation of the mixing that occurs in the real ocean. It is challenging to make observations that can be used to validate the mixing in the model. However, there are other ways to evaluate the impact of numerical mixing on our results.

First, we can examine the size of the numerical mixing in comparison with the resolved mixing, and whether it dominates the total mixing. On average, about one-third of the total mixing in the Salish Sea is due to numerical mixing in the model. This is reasonable for a realistic numerical model of a complex estuary. In Li et al. [2018], numerical mixing accounts for approximately one-third of the total mixing in their model of the Changjiang estuary. In contrast, models of estuaries with simpler geometries, such as the idealized model used in MacCready et al. [2018] or the Hudson river model used in Wang et al. [2017], have small, but non-negligible, numerical mixing. Ralston et al. [2017] found that approximately half of the

Table 2.1: Average values of numerical mixing as a percentage of the total mixing in each basin for 2017-2019.

Basin	**Numerical Mixing** [% of total mixing]
Tacoma Narrows	73.3
Hood Canal	59.6
South Sound	57.2
San Juan Islands	50.7
Admiralty Inlet	48.8
Strait of Juan de Fuca	42.2
Main Basin	37.5
Whidbey Basin	31.3
Strait of Georgia	27.5
Puget Sound	36.6
Salish Sea	32.4

mixing was numerical in an of the Connecticut River estuary, although they used an FVCOM model with an unstructured grid.

Because numerical mixing is a model artifact caused by discretization errors in the advection scheme, it will not necessarily have the same spatial structure as the resolved mixing. Therefore, we also want to know whether the proportion of numerical mixing is similar across the different basins in the Salish Sea. Table 2.1 shows the average percentage of the total mixing that is due to numerical mixing in each basin. We can see that there is a wide variation, with the numerical mixing accounting for an average of 27% to 73% of the total mixing, depending on the location. The high numerical mixing in Tacoma Narrows is likely because it is not well resolved, being only two cells wide in some places. On the other hand, the high proportion of numerical mixing in Hood Canal and South Sound, which are generally more stagnant, may simply be because there is not much resolved mixing in these basins.

To examine whether the numerical mixing has temporal behaviour similar to the resolved mixing, we use a linear regression of the numerical mixing against resolved mixing to see whether the numerical mixing stays at a constant proportion of the total mixing in each basin. The numerical mixing is most highly correlated in time with the resolved mixing in the San Juan Islands ($r^2 = 0.97$) while the lowest correlation by a significant margin is in Whidbey Basin ($r^2 = 0.51$). Overall, the numerical mixing is well-correlated temporally with the resolved mixing in most basins, with $r^2 = 0.76$ for the Salish Sea as a whole. The

Table 2.2: Average values of the volume-normalized total mixing, integrated total mixing, and horizontal mixing as a percentage of the resolved mixing, in each basin for 2017-2019. The nominal volume (with sea surface height $\zeta = 0$) is also given. The largest value in each column (excluding the totals for Puget Sound and the Salish Sea) is bolded.

Basin	**Volume-normalized Total Mixing** $[\mathrm{g^2 kg^{-2} s^{-1}}]$	**Integrated Total Mixing** $[\mathrm{g^2 kg^{-2} m^3 s^{-1}}]$	**Horizontal Mixing** [% of resolved mixing]	**Volume** $[\mathrm{m^3}]$
Whidbey Basin	$\mathbf{2.4 \times 10^{-5}}$	6.5×10^5	14.0	2.7×10^{10}
Tacoma Narrows	5.5×10^{-6}	2.3×10^3	5.4	4.2×10^8
San Juan Islands	4.3×10^{-6}	3.1×10^5	18.4	7.2×10^{10}
Admiralty Inlet	4.1×10^{-6}	7.1×10^4	20.1	1.7×10^{10}
Main Basin	3.1×10^{-6}	2.6×10^5	14.5	8.5×10^{10}
South Sound	3.1×10^{-6}	4.8×10^4	4.1	1.6×10^{10}
Strait of Georgia	3.0×10^{-6}	$\mathbf{4.0 \times 10^6}$	13.5	$\mathbf{1.3 \times 10^{12}}$
Hood Canal	2.9×10^{-6}	7.2×10^4	17.3	2.5×10^{10}
Strait of Juan de Fuca	2.1×10^{-6}	9.0×10^5	**22.9**	4.4×10^{11}
Puget Sound	6.5×10^{-6}	1.1×10^6	14.3	1.7×10^{11}
Salish Sea	3.1×10^{-6}	6.3×10^6	14.9	2.0×10^{12}

numerical mixing occurs at roughly the same place and time as the resolved mixing, and therefore should not adversely affect the analysis of mixing location and timing presented in the following sections.

2.4.2 Geographic distribution of mixing

To examine where mixed water is created in the Salish Sea, we divide our study region into nine basins, as shown in Figure 2.2. The average mixing in each basin for 2017-2019 is shown in Table 2.2. To start, we group the six smaller basins within Puget Sound together, leaving four "major basins" (Strait of Georgia, Strait of Juan de Fuca, San Juan Islands, and Puget Sound). The top panel of Figure 2.5 shows the mixing contributions of the four major basins. The largest contribution, with an average of about 4×10^6 $\mathrm{g^2 kg^{-2} m^3 s^{-1}}$, is from the Strait of Georgia, which is also the largest basin, with about two-thirds of the overall volume of the Salish Sea. Note that the total mixing in the Salish Sea is 6.3×10^6 $\mathrm{g^2 kg^{-2} m^3 s^{-1}}$, so the mixing in the Strait of Georgia is approximately proportional to its volume. The Strait of Juan de Fuca and Puget Sound have similarly sized contributions of around 1×10^6 $\mathrm{g^2 kg^{-2} m^3 s^{-1}}$. The San Juan Islands have strongly seasonal mixing, with low mixing on the order of 1×10^5 $\mathrm{g^2 kg^{-2} m^3 s^{-1}}$ during the winter, but often exceeding the mixing of the Strait of Juan de Fuca or Puget Sound during the summer months.

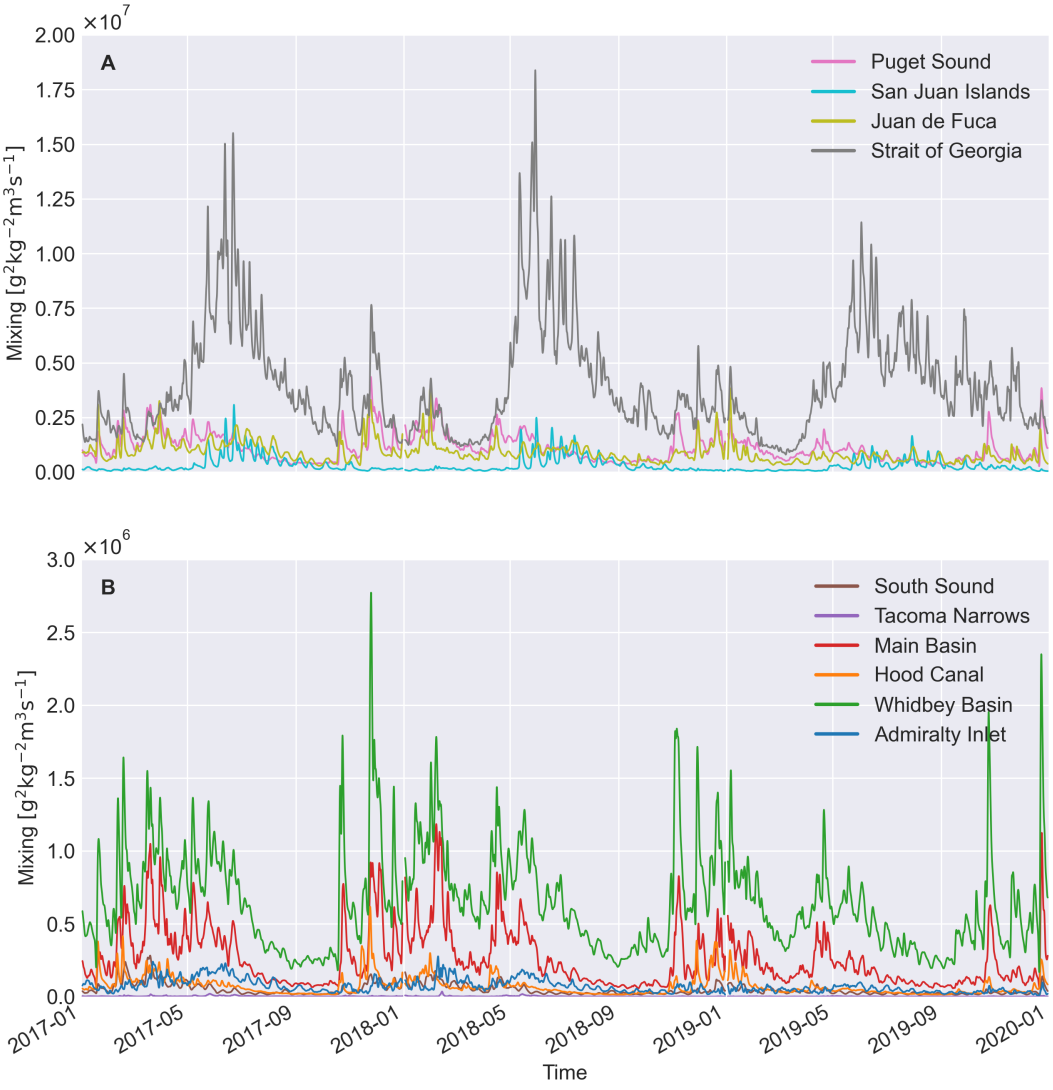

Figure 2.5: Mixing in the four major basins of the Salish Sea for 2017-2019, with all the Puget Sound basins grouped together into the pink line (A), and the breakdown of mixing in each basin of Puget Sound (B).

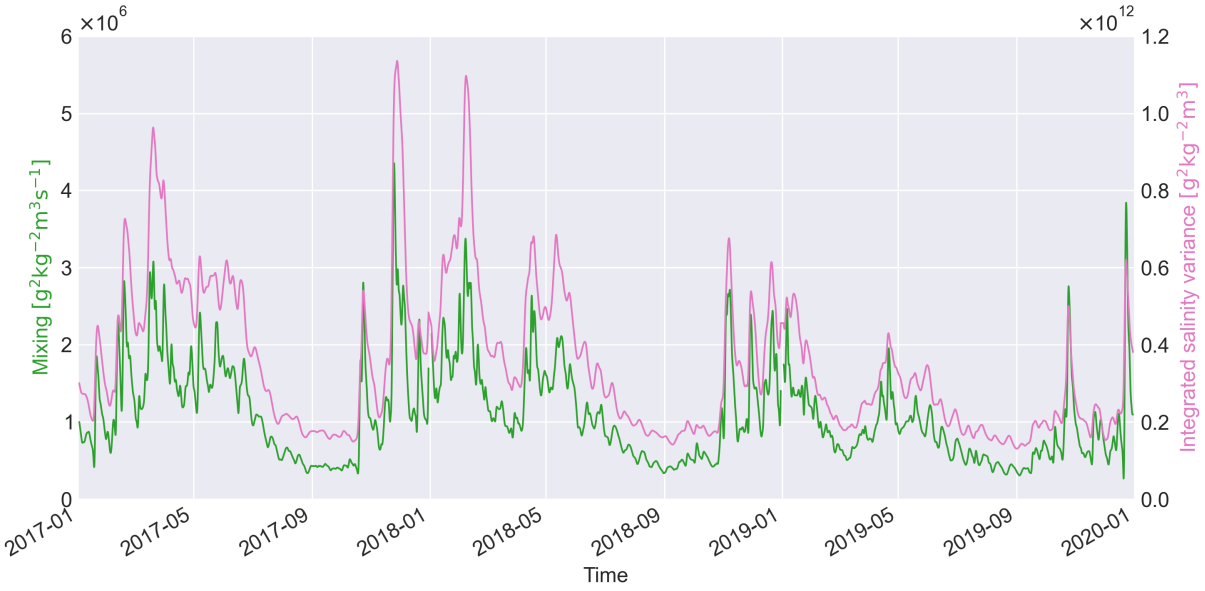

Figure 2.6: Total mixing and reservoir of salinity variance in Puget Sound for 2017-2019.

To provide context for these mixing rates, consider Figure 2.6, which shows a time series of the salinity variance reservoir and mixing in Puget Sound. The average variance is 3.5×10^{11} $\mathrm{g^2 kg^{-2} m^3}$. With an average mixing rate for Puget Sound of 1.1×10^6 $\mathrm{g^2 kg^{-2} m^3 s^{-1}}$, the reservoir divided by the rate gives a timescale of $\sim$3.7 days for all salinity variance to be mixed away.

Taking a closer look at the mixing within Puget Sound (bottom panel of Figure 2.5), we see that Whidbey Basin makes the largest contribution with over half of the total mixing in the Sound. Whidbey Basin is one of the shallower basins in Puget Sound and has large river inflow (the Skagit River accounts for approximately half of the river flow into Puget Sound). This large input of freshwater leads means that there is more salinity variance (as horizontal gradients and high stratification) available to be destroyed by mixing. Main Basin also has a significant contribution, primarily due to its large size.

Figure 2.5 concerned only the integrated total mixing. Alternatively, we may consider the volume-normalized total mixing in each basin, as shown in Figure 2.7. Here we can clearly see that Whidbey Basin has the most intense mixing. Other areas of intense mixing are Tacoma Narrows and the San Juan Islands. The weaker mixing in 2019 is associated with lower-than-average river flows. The three-year average of volume-normalized total mixing in each basin is shown in Table 2.2.

Puget Sound has historically been considered as a network of quiescent basins connected by highly

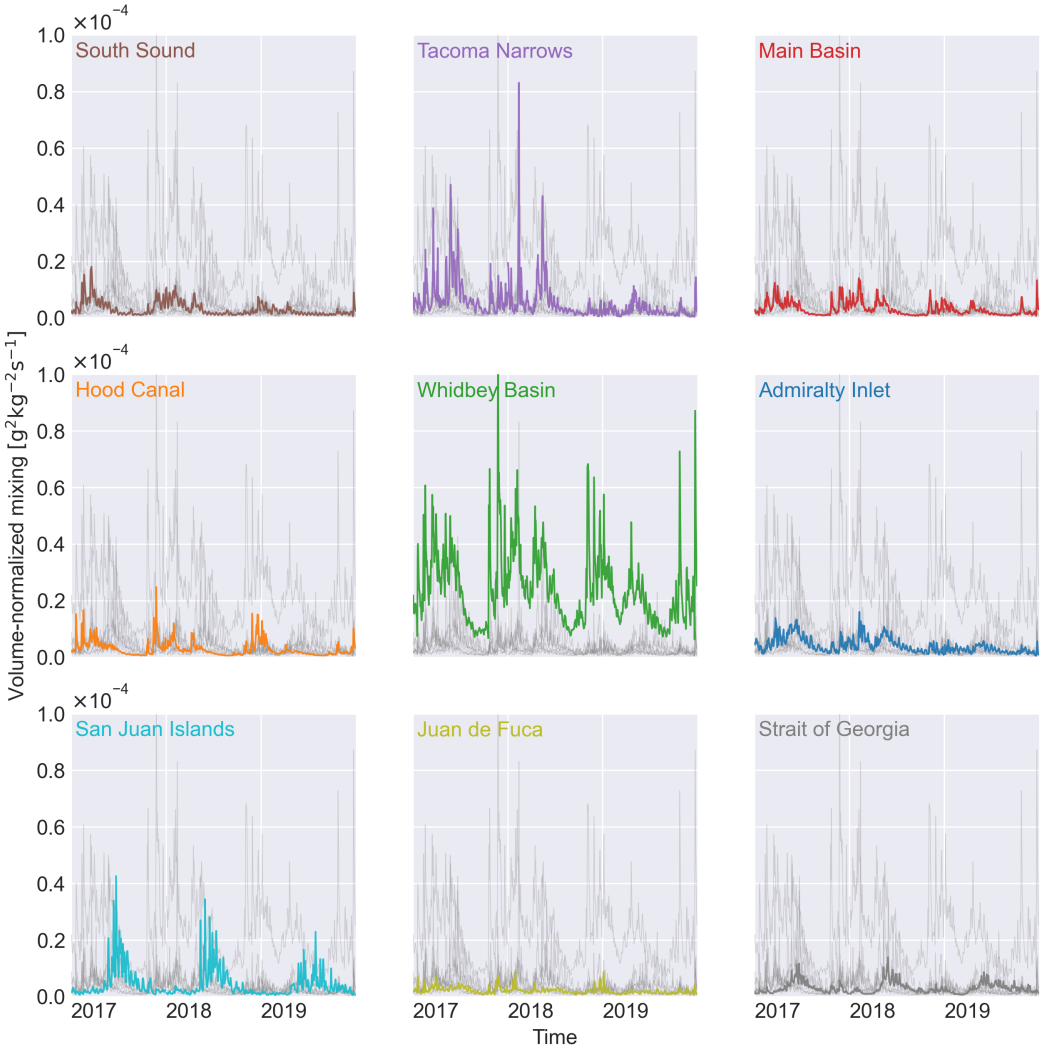

Figure 2.7: Volume-normalized total mixing in each basin for 2017-2019. The scale is the same in each subplot and the thin grey lines show the volume-normalized total mixing in the other basins for ease of comparison.

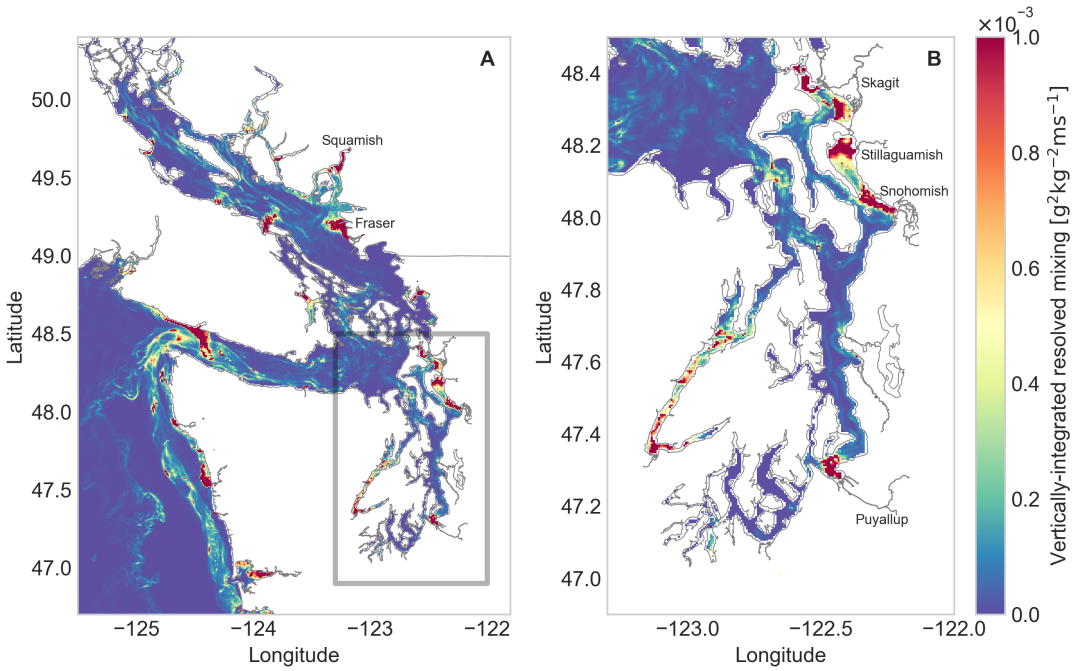

Figure 2.8: Map of vertically-integrated resolved mixing per unit horizontal area at 19:00 on January 19, 2017 in the Salish Sea (A) and Puget Sound (B). Selected rivers are labeled. Note that the mixing is highly concentrated at the river mouths.

energetic sills where strong mixing occurs [Cokelet and Stewart, 1985; Ebbesmeyer et al., 1988]. In contrast, the combined mixing that occurs at Tacoma Narrows and Admiralty Inlet in our results only accounts for about 6.6% of the mixing in Puget Sound. The mixing is also not significantly more intense at these sills. Aside from Whidbey Basin, all the basins within Puget Sound have average volume-normalized total mixing within the same order of magnitude. Although Tacoma Narrows and Admiralty have the strongest mixing after Whidbey Basin, their volume-normalized mixing rates are still less than double that of Hood Canal, which has the weakest mixing in Puget Sound.

On a finer scale, we can look at a map of resolved mixing in the Salish Sea. Because we have estimated the numerical mixing as the residual of the salinity variance budget for an entire basin, we cannot determine the amount of total mixing in each cell or water column. Figure 2.8 shows an example of the vertically-integrated resolved mixing per unit horizontal area. Within each basin, the mixing is primarily concentrated at the river mouths, which are sources of high-variance water.

As described in Section 2.3.4, horizontal mixing is not negligible in the model. In assessing where mixed water is produced, a related question is whether the breakdown between vertical and horizontal mixing is consistent across the various basins. Table 2.2 shows the percentage of the resolved mixing that is due to horizontal mixing in each basin. Overall, horizontal mixing accounts for $\sim$15% of the resolved mixing in the Salish Sea, with values as low as 4-5% in South Sound and Tacoma Narrows, and as high as 23% in the Strait of Juan de Fuca. K_H is constant in the model ($2.0\ \mathrm{m^2 s^{-1}}$), so the amount of horizontal mixing depends primarily on how strong the horizontal salinity gradients are.

2.4.3 Correlation of mixing and forcing factors

To ascertain when mixed water is produced in the Salish Sea, we look at the correlation of mixing with various forcing factors. In Figure 2.5 we can see that the various basins have different timing for their peaks in mixing. Puget Sound and the Strait of Juan de Fuca have their peak in mixing during the winter, while the Strait of Georgia and San Juan Islands peak later in the spring. To study the timing of mixing in the Salish Sea we consider three different external forcings as described in Section 2.3.6. Figure 2.9 shows the river flow, spring-neap cycle, and wind time series overlaid on the total mixing in the Salish Sea. It is immediately apparent that the mixing most closely follows the river flow curve. Note that there is a declining trend in the river flow over the three years studied. Figure 2.10 shows the correlation coefficient r from a lagged correlation of the mixing term with the three forcing factors for each basin. The rivers are the dominant forcing factor and positively correlated with the mixing magnitude in most basins, with winds and tides being of secondary importance. The lag between the river flow and mixing ranges from 11 hours in the Strait of Juan de Fuca to 39 hours in the Strait of Georgia. Tacoma Narrows and Admiralty Inlet do not have rivers entering them directly. The correlation coefficients of mixing with rivers entering basins landward of Tacoma Narrows and Admiralty Inlet are 0.41 and 0.55, respectively. Similarly, the correlation of mixing with rivers in the San Juan Islands actually has a small negative correlation. However, only the Samish River enters the San Juan Islands segment directly, but mixing in the San Juan Islands is influenced by the Fraser River flow which enters the Strait of Georgia. The maximum correlation of the San Juan Islands mixing with the rivers entering the Strait of Georgia is 0.69.

We have determined that mixing is highly correlated with river flow. To answer our question of when

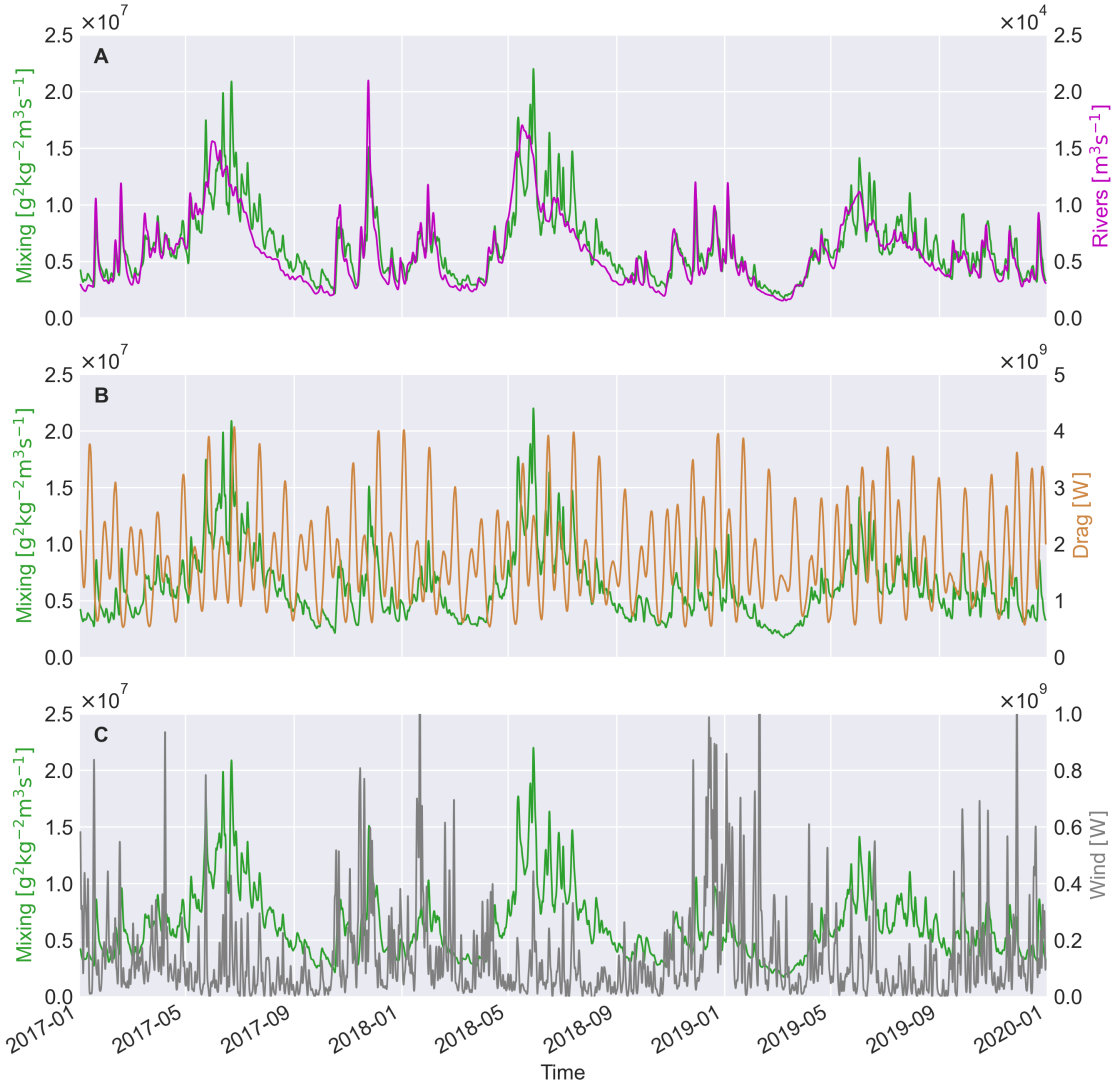

Figure 2.9: Time series of mixing in the Salish Sea for 2017-2019 plotted with three different forcing factors: total river flow (A), energy dissipation due to bottom drag (B) which represents the spring-neap cycle, and energy input from winds (C). Note that the mixing most closely follows the shape of the river flow time series.

Figure 2.10: Radar plots showing the correlation coefficient $|r|$ from a lagged correlation between the mixing and forcing factors in each basin. The $+$ or $-$ sign next to the name of the forcing factor indicates whether the corrlation is positive or negative. Note that Admiralty Inlet and Tacoma Narrows do not have any rivers entering them directly, so the correlation with the landward rivers is shown instead. The San Juan Islands have only one river, the Samish river, entering directly.

mixed water is created, we need to know what creates the different patterns of river flow in each basin. The overall annual cycle of the river flow depends on what type of watershed it drains [Casola et al., 2005; Lee and Hamlet, 2011]. In snow-dominant watersheds, snow accumulates in the watershed over the winter and peak flow is during the spring when snow melts. In rain-dominant watersheds, peak flow is during the winter due to heavy preciptation. Mixed rain and snow watersheds generally have two peaks, one in the winter and one in the spring. This explains why the Strait of Georgia and San Juan Islands have their mixing peak in the spring, since they are most affected by the Fraser River, which has a snow-dominant watershed. The rivers entering the Strait of Juan de Fuca and Puget Sound mostly have rain-dominated or mixed watersheds, which is why they have a flatter mixing peak across the winter and spring. Streamflow patterns in the Salish Sea and Puget Sound are predicted to change in the future, as climate change alters the size of snowpacks and how rapidly they melt, and watersheds transition towards more rain-dominated regimes [Casola et al., 2005; Lee and Hamlet, 2011]. Therefore, the timing of mixing in the Salish Sea will likely change in the future.

The lack of influence of the spring-neap cycle on the timing of mixing is in contrast to previous studies such as Wang et al. [2017], Li et al. [2018], MacCready et al. [2018] and Wang and Geyer [2018], where a pronounced spring-neap effect was observed. However, all of these studies except Li et al. [2018] used a constant river flow in their model setup, and a dependence of mixing on river flow was found in Wang and Geyer [2018] in their experiments testing varying levels of constant river discharge. The river flow entering the Salish Sea, which imports high-variance water into the estuary, varies drastically throughout the year. Although the mixing is provided primarily by tides, the total amount of mixing is controlled by how much variance is available to be destroyed rather than by the smaller fluctuations in the strength of the tides. This can also be seen in Figure 2.6, where the mixing rate curve closely follows the reservoir of integrated salinity variance. The other estuaries previously studied generally have lower mean salinities than the Salish Sea, such that advection of salinity variance through the ocean boundaries plays a more significant role.

2.4.4 Removal of mixed water from the estuary

To discover when mixed water is removed from the estuary, we look at the correlation of the outflowing mixedness transport $Q_{out}m_{out}$ with the same three forcing factors used in Section 2.4.3. Note that for this

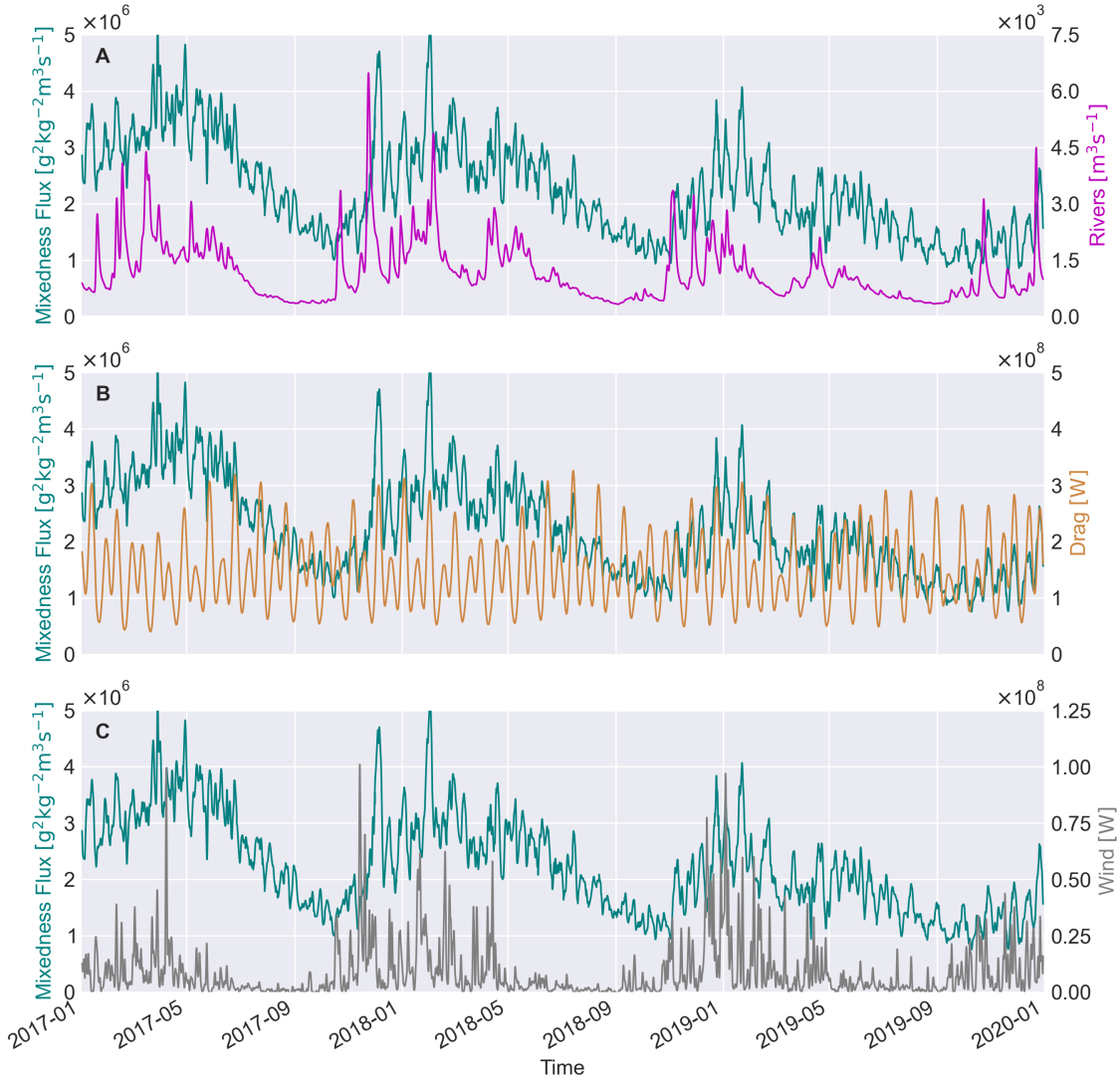

Figure 2.11: Time series of outflowing mixedness transport for Puget Sound for 2017-2019 plotted with three different forcing factors: total river flow (A), energy dissipation due to bottom drag (B) which represents the spring-neap cycle, and energy input from winds (C).

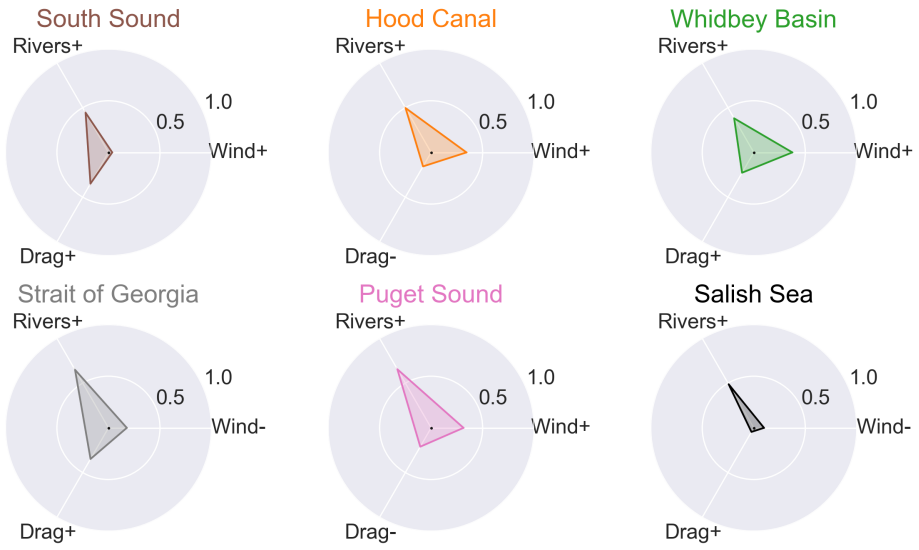

Figure 2.12: Radar plots showing the correlation coefficient $|r|$ from a lagged correlation between the outflowing mixedness transport and forcing factors in the enclosed basins. The $+$ or $-$ sign next to the name of the forcing factor indicates whether the correlation is positive or negative.

section we only consider the "enclosed" basins, while excluding Tacoma Narrows, Main Basin, Admiralty Inlet, the San Juan Islands, and the Strait of Juan de Fuca. Figure 2.11 shows the river flow, spring-neap cycle, and wind time series overlaid on the outflowing mixedness transport for Puget Sound. Because we use the TEF salinity s_{out} to calculate the mixedness, the time series for the Salish Sea (not shown) is much noisier than that for Puget Sound. This is caused by the Columbia River plume entering the Salish Sea through the Strait of Juan de Fuca, which can promote reverse estuarine circulation, as described in Thomson et al. [2007] and Giddings and MacCready [2017]. While the salinities for Puget Sound behave as expected, with s_{out} always fresher than s_{in}, the Salish Sea has inversions when s_{in} is fresher than s_{out}.

Figure 2.12 shows the correlation coefficients r from a lagged correlation of the three forcing factors with the outflowing mixedness transport for the enclosed basins. The rivers are the most important factor in every basin, and the coupling is generally tighter with the mixing (Figure 2.10) than the mixedness transport. The lag between the river flow and mixedness transport time series is 9.9 days and 14.7 days in Puget Sound and the Salish Sea, respectively, which is much longer than the lag between the river flow and mixing ($\sim$1 day). This is reasonable because mixing is concentrated at river mouths, far from the open boundaries where

mixed water is expelled.

2.4.5 Long-term average mixing approximation

Finally, we want to determine how well the long-term average mixing approximation proposed in MacCready et al. [2018] can predict the mixing in the Salish Sea, and on what timescales. Figure 2.13 shows the total mixing M from the salinity variance budgets and the approximations $Q_r s_{out} s_{in}$ and $Q_{in} \Delta s \, s_{in}$ for Puget Sound. The timeseries are all tidally averaged and sampled hourly.

As shown, the long-term average approximation $Q_r s_{out} s_{in}$ gives a good estimate of the mixing in Puget Sound, even without any additional time averaging. The root mean square error (RMSE) normalized by the mean mixing is 0.297. This approximation performs similarly well in the Salish Sea as a whole, with a normalized RMSE of 0.266. Additional averaging did not significantly improve the mixing estimates. The lag between the long-term average approximation and the mixing in the history budgets is 28 hours in Puget Sound and 27 hours in the Salish Sea, which is on the same order of magnitude as the lag between the river flow and mixing reported in Section 2.4.3. It is somewhat surprising that an approximation that assumes time-averaged conditions should perform so well without any temporal averaging in an environment where the river flow varies by an order of magnitude. However, most of the mixing occurs near the river mouths, and therefore the basin-wide mixing reacts quickly to river discharge. Because the river flow is tightly coupled with the mixing, and the salinities s_{in} and s_{out} vary only by $\sim 2 \text{ g kg}^{-1}$ over the year, Puget Sound and the Salish Sea are exactly the type of estuary where this type of approximation can be successfully implemented. It is particularly convenient to be able to use $M = Q_r s_{out} s_{in}$ to predict the mixing in an estuary since the formula only requires knowledge of the TEF properties on the open boundaries and the river flow, but does not require any information about the interior of the estuary. However, it should be noted that this approximation relies on the assumption that $s_{in}'^2 \approx (s_{in} - \bar{s})^2$ and $s_{out}'^2 \approx (s_{out} - \bar{s})^2$. For cases where this assumption is not valid, Burchard et al. [2019] have defined a hierarchy of mixing parametrizations with and without constancy and periodicity assumptions.

Conversely, the approximation $Q_{in} \Delta s \, s_{in}$ does not follow the mixing curve closely in Puget Sound. This is likely due to time-dependence of variance storage in the system. As shown in Figure 2.13, the peaks of $Q_{in} \Delta s \, s_{in}$ align with neap tides. This is consistent with the findings of Geyer and Cannon [1982] that

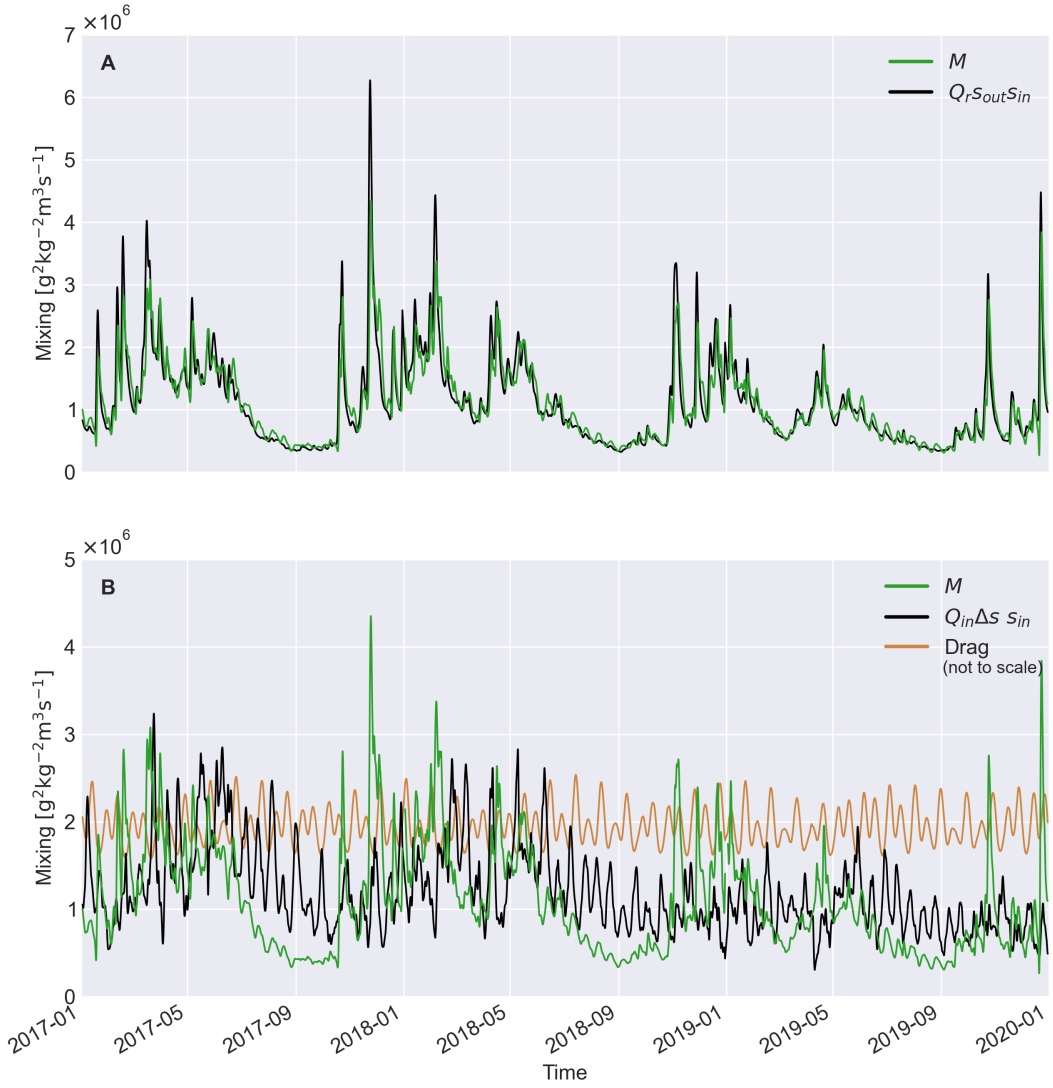

Figure 2.13: Total mixing calculated from the salinity variance budget and using the long-term average approximations $M = Q_r s_{out} s_{in}$ (A) and $M = Q_{in} \Delta s\, s_{in}$ (B) in Puget Sound for 2017-2019. The brown curve (B) represents the spring-neap cycle (tidally-averaged energy dissipation due to bottom drag, not to scale).

the gravitational circulation and stratification at Admiralty Inlet were greatest at neap tides. However, three-year average of mixing in Puget Sound is 1.10×10^6 $\mathrm{g^2 kg^{-2} m^3 s^{-1}}$, while $Q_r s_{out} s_{in}$ and $Q_{in} \Delta s \, s_{in}$ have averages of 1.12×10^6 $\mathrm{g^2 kg^{-2} m^3 s^{-1}}$ and 1.19×10^6 $\mathrm{g^2 kg^{-2} m^3 s^{-1}}$, respectively. Therefore, over a long time average, $Q_{in} \Delta s \, s_{in}$ may be used to provide a reasonable estimate of mixing in Puget Sound. Note that this approximation is not a good choice for the Salish Sea as a whole, due to the reversals in estuarine circulation discussed previously, which lead to negative values of Δs.

The salt budget in an estuary may be expressed in terms of the TEF variables:

$$\frac{d}{dt} \int_V s \, dV = Q_{in} s_{in} + Q_{out} s_{out} \tag{2.19}$$

By substituting $Q_r = -(Q_{in} + Q_{out})$ and $\Delta s = s_{in} - s_{out}$, we may alternatively express the salt budget as

$$\frac{d}{dt} \int_V s \, dV = Q_{in} \Delta s - Q_r s_{out} \tag{2.20}$$

where $Q_{in} \Delta s$ represents the exchange flow salt transport and $Q_r s_{out}$ represents the river salt transport.

Note that either term on the right-hand side of Equation 2.20 multiplied by s_{in} is equal to one of the long-term average mixing approximations. In Puget Sound, s_{in} is approximately constant over time, with small variations of ~ 2 $\mathrm{g\,kg^{-1}}$. Therefore, using the approximation $M \approx (Q_{in} \Delta s) s_{in}$, the mixing in Puget Sound is proportional to the exchange flow salt transport. We noted in the introduction that the approximation $M = Q_{in} \Delta s \, s_{in}$ provides an inexplicit link between mixing and the estuarine exchange flow. However, in systems similar to Puget Sound it may be more useful to instead consider that the direct link is between mixing and the exchange flow salt transport.

The $Q_r s_{out} s_{in}$ approximation can also be used to calculate the mixing completeness $M/(Q_r s_{in}^2)$, which is the ratio of total mixing to theoretical maximum mixing [MacCready et al., 2018]. Using the three-year average values of mixing, river flow, s_{in}, and s_{out}, the mixing completeness in Puget Sound is 94.1%. This is high compared to values of mixing completeness found in studies of other estuaries. For example, MacCready et al. [2018] found 68% mixing completeness in their idealized V-shaped estuary model, and Lange et al. [2020] found 84% mixing completeness in a modeling study of the weakly tidal Warnow estuary.

2.5 Summary

Using salinity variance budgets, we have gained insights into how mixing occurs in the Salish Sea. Most mixing occurs in the Strait of Georgia where the volume-normalized mixing is close to the average for whole Salish Sea, due to its large size. The volume-normalized mixing is lower in the Strait of Juan de Fuca and higher in Puget Sound, although these two regions make similarly-sized contributions to the total mixing. The strongest mixing by far occurs in Whidbey Basin, likely due to its shallow depth and large river flow. The timing of mixing in all regions of the Salish Sea is highly correlated with the river flow, whose annual cycle depends on whether the watershed is snow-dominated, rain-dominated or mixed. Because $\bar{s}$ is close to the oceanic salinity in the Salish Sea, the rivers have very high variance and dominate the input of salinity variance to the estuary even though their volume transport is low. Unlike other estuaries studied using the salinity variance framework, no pronounced spring-neap cycle is seen in the mixing time series for the Salish Sea. Using the outflowing mixedness transport we determine that mixed water is also removed from the estuary when river flow is high, but the coupling is not as tight as it is between the river flow and mixing. Even without any additional time-averaging, the long-term average mixing approximation $M = Q_r s_{out} s_{in}$ can accurately predict the mixing in the Salish Sea and Puget Sound. Because the mixing is tightly coupled with the river flow and the s_{in} and s_{out} do not vary widely over time, additional averaging does not significantly improve the performance of this long-term average approximation. Over a long time average, the alternative approximation $M = Q_{in} \Delta s \, s_{in}$ may also be used to estimate the mixing in Puget Sound. Because s_{in} is nearly constant for Puget Sound, the average mixing in Puget Sound is directly proportional to the average exchange flow salt transport $Q_{in} \Delta s$. The residual of the salinity variance budget gives an estimate of the numerical mixing, which accounts for approximately one-third of the total mixing in our model.

Acknowledgments

This project was supported by NSF Award 1736242: Using Salinity Variance to Link Estuarine Mixing and Exchange Flow. We thank W. Rockwell Geyer for the mixedness concept.

Data availability statement

All code used in this analysis is archived at 10.5281/zenodo.6568187, including code for calculating salinity variance budgets, salinity variance reservoirs, and forcing factor time series. Output data files and plotting code are also included. The LiveOcean model code is archived at 10.5281/zenodo.4282775 [MacCready et al., 2021].

Chapter 3

Exchange flow mechanisms in estuaries with long and short sills

Abstract

An ensemble of idealized estuary models is used to study the effects of varying sill lengths on the estuarine exchange flow mechanism and subtidal salt transport. Each model contains an estuary with bathymetry characteristic of fjords, with two large, deep basins separated by a shallow, narrow sill. Five different models are created with sill lengths ranging from $5\ \mathrm{km}$ to $80\ \mathrm{km}$, and a tidal excursion of $20\ \mathrm{km}$. The models are forced with constant river flow and a simple spring-neap cycle. Three different exchange flow decompositions are calculated at cross sections along the sill, as well as momentum balances for the inflowing and outflowing layers of the exchange flow. The response of the estuary to changing tidal forcing is used to understand the dynamics of the exchange flow. The ends of the sills have behavior consistent with tidal pumping, while the middle of the sill is characteristic of gravitational circulation, with a stronger gravitational circulation developing in the longer sill models. For shorter sills the salt transport increases at spring tide, consistent with expectations for tidal pumping. As the sill length increases past the length of the tidal excursion the pattern reverses: salt transport decreases at spring tide, consistent with expectations for gravitational circulation. The sill length also influences the time-mean salinity structure: the inner basin becomes fresher with increasing sill length. All of the model ensemble members occupy the same part of the estuarine parameter

space of Geyer and MacCready [2014], but exhibit different exchange flow mechanisms and salt transport behavior. This suggests that a third parameter, the sill length to tidal excursion ratio, is required to describe the character of these otherwise similar estuaries.

3.1 Introduction

A shared feature among estuaries of many types is the development of an estuarine exchange flow, which exchanges water and tracers such as salt between the estuary and the coastal ocean. However, this exchange is not driven by the same process or processes across all estuaries, or even within a single estuary, and many exchange flow mechanisms have been proposed.

The classical description of the estuarine exchange flow is a gravitational circulation. The salinity difference between the fresh river water and salty ocean water creates a baroclinic pressure gradient in the estuary [Hansen and Rattray, 1965; MacCready and Geyer, 2010]. This induces a density-driven flow, which draws ocean water into the estuary at depth and expels brackish water at the surface. The force due to the baroclinic pressure gradient is opposed by the vertical turbulent stress divergence in the fluid.

However, exchange may also be caused by other processes. One alternative to gravitational circulation is tidal pumping, whereby water exiting the estuary on the ebb tide is replaced by water of a different salinity during the flood tide. Although there is no standardized definition of tidal pumping, we use this term to describe correlation of transport and salinity on tidal timescales, which may arise from several different physical mechanisms. An example of such a scenario is a jet-sink asymmetry, as described in Stommel and Farmer [1952], where mixed water exits through a constriction as a jet on the ebb and saltier water is drawn back into the estuary in a radial pattern on the flood. Similarly, tidal trapping in side channels can create stronger correlation between velocity and salinity in the estuary [Okubo, 1973; MacVean and Stacey, 2011]. Exchange may also be affected by interactions between gravitational circulation and tidal processes [Fram et al., 2007].

In addition, a variety of lateral processes may be important in the development of the estuarine exchange flow, including lateral salinity gradients driven by differential advection [Geyer et al., 2020], flood-ebb asymmetry in lateral circulation [Lerczak and Geyer, 2004] and tidal rectification [Scully et al., 2009]. Exchange flow may also arise from tidal variation in the eddy viscosity [Jay and Musiak, 1994; Burchard

and Schuttelaars, 2012; Dijkstra et al., 2017]. Other external factors such as wind forcing [Wong, 1994; Scully et al., 2005] may also generate exchange. For the purposes of this study we will focus on two main mechanisms, gravitational circulation and tidal pumping.

The dominant mechanism of the exchange flow is influenced by the geometry of the estuary. Abrupt bathymetric variation is likely to give rise to flow separation which can enhance tidal pumping. Chen et al. [2012] found that the length of an estuary, as defined by the the salt intrusion, relative to the tidal excursion is an important factor in determining the mechanism of salt flux. They found that exchange flow in the long Hudson river was well described by a Simpson number scaling, consistent with gravitational circulation driven by the baroclinic pressure gradient. In contrast, exchange flow in the short Merrimack river was better described by a tidal transport scaling, indicating the importance of tidal pumping. Garcia and Geyer [2023] also found increasing importance of tidal processes as the estuary becomes shorter. Topographic features such as constrictions, meanders, and the estuary mouth allow for flow separation, while shallow shoals allow tidal trapping and differential advection [Garcia and Geyer, 2023].

Another type of feature which may favor tidal pumping as an exchange flow mechanism are sills, which are common in fjords. The circulation in fjordal estuaries is often complicated by highly irregular geometry including branching basins, constrictions, and shallow sill areas formed by glacial till or hard bedrock. These sills restrict circulation with the ocean and between basins, and can be areas of enhanced mixing and reflux [Cokelet and Stewart, 1985]. Additionally, sills often have elevated tidal velocities compared with other parts of the estuary due to their reduced cross-sectional area, and sharp topographic changes at the ends of the sill may promote flow separation. Where stratification is present, tides may generate internal waves at the sill [Stigebrandt, 1976, 1980]. Sills and constrictions can exert hydraulic control on a two-layer flow [Armi and Farmer, 1986; Farmer and Armi, 1986], and time-dependent barotropic currents can increase the maximum two-layer transport capacity of the sill [Stigebrandt, 1977; Helfrich, 1995].

It is also important to note that sills and irregular bathymetry are not unique to fjords and are found in many types of estuaries around the world. For example, the Baltic Sea is connected to the North Sea through the Danish Straits, where water must pass over the shallow Darss ($18\ \mathrm{m}$) or Drogden ($7\ \mathrm{m}$) sills [Fischer and Matthäus, 1996]. The Mattituck Sill in Long Island Sound has been shown to influence the circulation [Valle-Levinson and Wilson, 1998; Whitney et al., 2014]. Chesapeake Bay, a large coastal plain

estuary, has a shallow sill in the lower basin at Rappahannock Shoal [Xiong et al., 2021a]. At the entrance to San Francisco Bay, a shallow sandbar exists just seaward of the Golden Gate, which is itself a lateral constriction, albeit with deeper bathymetry than the rest of the Bay.

The length of the sill is an important factor in determining when deep water renewal in the basins will occur. In a physical hydraulic modeling study, Farmer and Rattray [1963] found that deep water intrusions in Puget Sound occur when the flood tidal range at Seattle exceeded $3.5\ \mathrm{m}$, which corresponded to when the tidal excursion exceeded the length of the entrance sill at Admiralty Inlet. When water can transit the sill in a single tidal period it experiences less mixing than if it remains in the energetic sill zone for multiple tidal cycles. Deep water replacement under these conditions was observed by Cannon and Laird [1978] during winter. However, the salinity of deep water outside the estuary and mixing along the finite-length sill are also important factors. At certain times of the year, no inflow was observed during high tidal ranges and deep water intrusion did occur during tidal ranges below $3.5\ \mathrm{m}$ [Cannon and Laird, 1978]. Geyer and Cannon [1982] found that bottom water renewal in Puget Sound occurs at neap tides, and that tidal advection only contributes to bottom water renewal during extreme tides close to the solstices. Similarly, Deppe et al. [2018] found that intrusions of deep low-oxygen water into Puget Sound occur at neap tides with maximum diurnal inequality, which create conditions of minimal mixing and stronger gravitational circulation.

While the importance of sill length relative to the tidal excursion has often been discussed in the context of deep water renewal, the relationship between sill length and the mechanism of the estuarine exchange flow has not been investigated. For the Salish Sea, MacCready and Geyer [2024] found that different areas of the estuary exhibited behavior consistent with tidal pumping and/or gravitational circulation. Additionally, even in regions where the exchange flow increased with stronger tides (consistent with tidal pumping), the salt transport often decreased with stronger tides due to increased mixing which reduces stratification. It remains to be explained why different sections of the estuary behave as they do.

Our main goals are to answer the questions:

- What is the dominant mechanism of the exchange flow and how does it vary with sill length?
- How does the sill length to tidal excursion ratio affect the magnitude of the estuarine exchange flow and subtidal salt transport?

To tackle this problem, we use an idealized modeling approach. While highly realistic models allow for a

more accurate depiction of a particular estuary, it can be difficult to tease apart causes and effects when many complex features and variable external forcings are present. On the other hand, simple theoretical models, which can account for variation in the dimensions of the system, may not include enough complexity to describe the effects of the bathymetic irregularities that we are interested in. Idealized models offer a middle ground that brings more clarity to our exploration of bathymetrically complex estuaries, while also allowing for more generalizable results. Other recent studies have employed idealized models to study the effects of various types of topographic features in estuaries. Garcia and Geyer [2023] use an idealized model based on the North River estuary including areas with channel curvature, intertidal shoals, and a constriction to study tidal dispersion. Bo and Ralston [2022] use three idealized models with varying amounts of channel curvature to investigate the impact on stratification and mixing. Bao and Moffat [2024] use an idealized fjord model with variable height sills to determine the effect of sill height on circulation and glacial melting. Brasseale and MacCready [2021] use five idealized V-shaped estuary models with differing shelf slopes and mouth widths to study the sources of shelf inflow to the estuary.

In this study, we use idealized estuary models with varying sill lengths. This allows us to study how the ratio of sill length to tidal excursion affects the characteristics of the estuarine circulation.

In section 3.2, we give an overview of the idealized model ensemble and analysis procedures, including three salt flux decompositions and layer-averaged momentum budget calculations. In section 3.3 we discuss results and in section 3.4 we summarize conclusions.

3.2 Methods

3.2.1 Idealized model ensemble

To study the effect of varying sill lengths on the estuarine circulation, we developed an ensemble of five idealized models using the Regional Ocean Modeling System (ROMS) [Shchepetkin and McWilliams, 2005]. The dimensions of the model estuaries are loosely based on the geometry of Puget Sound and its sill at Admiralty Inlet. The model domain covers 4° latitude, centered around 45° N, and 6.5° longitude, with a north-south coastline at 0° longitude. The estuary is located at 45°N. The cell dimensions vary from $320\ \mathrm{m}$ in the estuary to $2.5\ \mathrm{km}$ at the oceanic boundaries, with 30 s-coordinate terrain-following vertical layers.

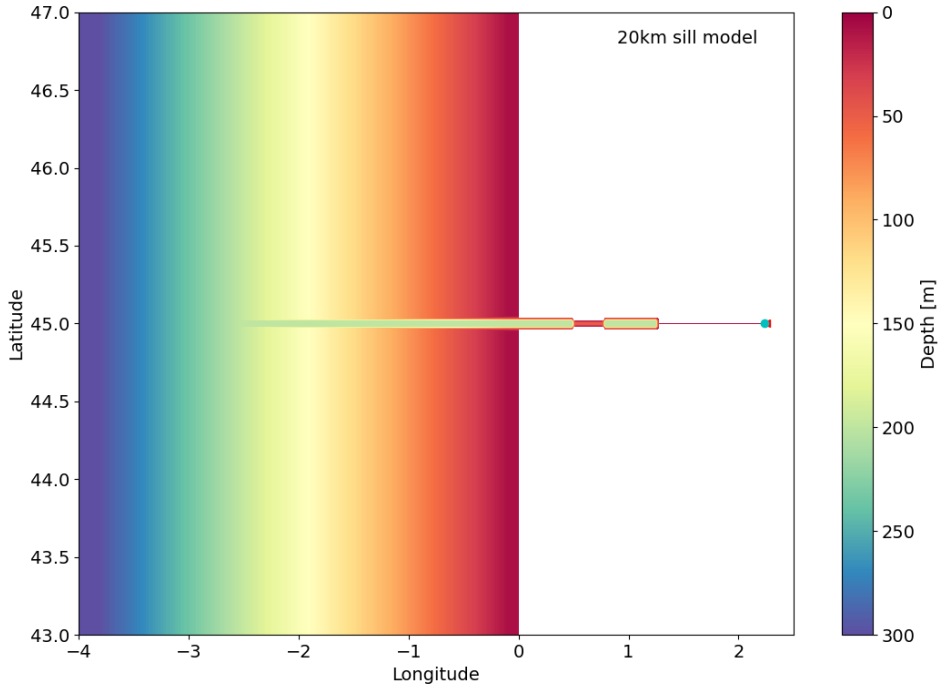

Figure 3.1: Idealized model grid for the $20\ \mathrm{km}$ sill ensemble member. Colormap shows bathymetry. Red line shows the river channel ($5\ \mathrm{m}$ deep), blue dot shows the cell where river input is added, and red triangle indicates the side of the cell where the point source is located and its flow direction. All other ensemble members have the same domain and coast bathymetry with the estuary and river located at the same latitude. See Figure 3.2 for the estuary bathymetry in all ensemble members.

Each model has an estuary with two basins, with each basin being $40\ \mathrm{km}$ long by $8\ \mathrm{km}$ wide and $200\ \mathrm{m}$ deep, separated by a shallow and narrow sill that is $4\ \mathrm{km}$ wide and $50\ \mathrm{m}$ deep. The five models have different sill lengths: $5\ \mathrm{km}$, $10\ \mathrm{km}$, $20\ \mathrm{km}$, $40\ \mathrm{km}$, and $80\ \mathrm{km}$. The $20\ \mathrm{km}$ sill model grid (Figure 3.1) is designed to be most similar to Admiralty Inlet. A close-up of the estuary portion of the grid in all 5 models is shown in Figure 3.2. While the deep basins used here are more characteristic of fjords than coastal plain estuaries, they function mainly as less dynamically active regions surrounding the dynamically active sill.

The river forcing is a constant $1000\ \mathrm{m^3\ s^{-1}}$ delivered at the landward end of the estuary by a single river of 5m depth. There is no atmospheric forcing and the water temperature everywhere is 10°C. The ocean boundary is forced with M2 and S2 tides, creating a simple spring-neap cycle. The ocean (west of 0°longitude) is initialized with a vertical salinity stratification of $1\ \mathrm{psu}/50\ \mathrm{m}$ from $30\ \mathrm{psu}$ at the surface to

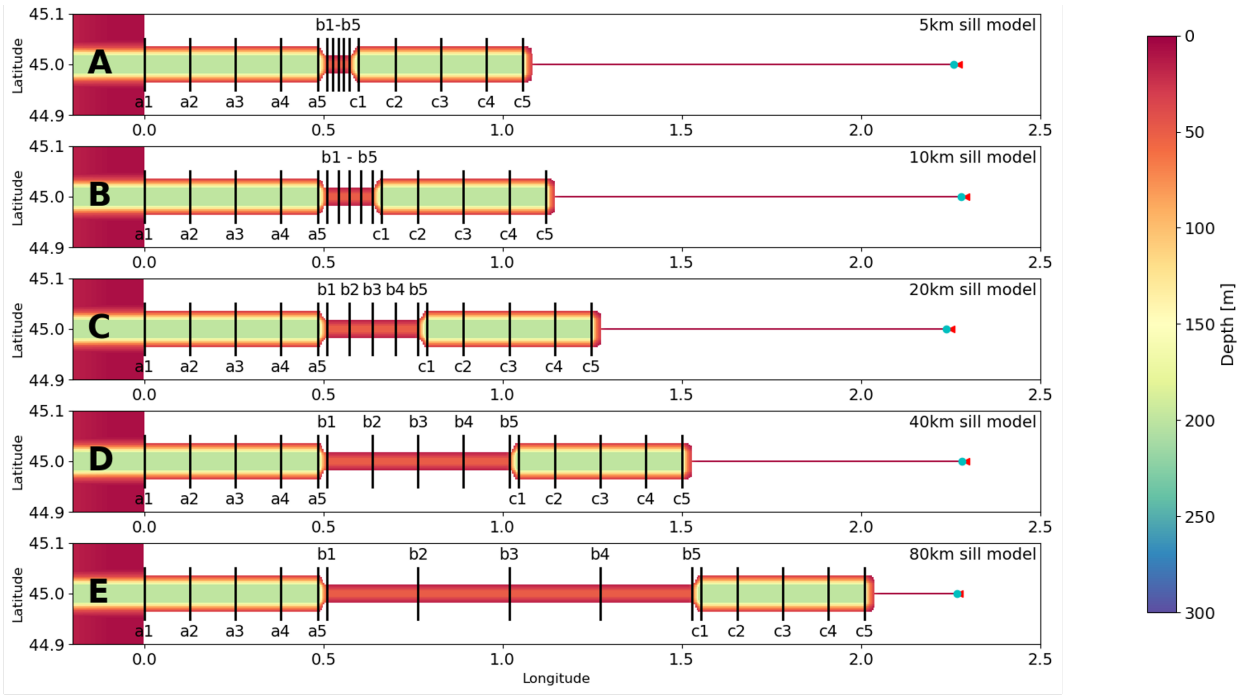

Figure 3.2: Model estuaries with (A) 5 km, (B) 10 km, (C) 20 km, (D) 40 km, and (E) 80 km sills. Black lines show the cross sections used for exchange flow decompositions. Colormap shows bathymetry, and color scale is the same as in Figure 3.1. Red lines show the river channels (5 m deep), blue dots show the cells where river input is added, and red triangles indicate the sides of the cells where the point sources are located and their flow direction. The inner and outer basins are 40 km long in all models. Each basin and the sill has five sections approximately evenly spaced across it, except that sections a5, c1, and c5 are shifted 2 km towards the middle of their respective basins (otherwise they would coincide with sections b1, b5, and the end of the estuary, respectively).

34 psu at 200 m and deeper. This stratification is also maintained as the ocean boundary condition. The estuary is initialized with all fresh water, which promotes faster spin-up of an estuarine exchange flow. The model is run for one year, with the first eight months as spinup, and the last four months used for analysis.

The tidal excursion L_T is the distance that a water parcel covers along the estuary over a tidal cycle:

$$L_T = \frac{U_T T}{\pi} \tag{3.1}$$

where U_T is the amplitude of the tidal velocity and T is the tidal period. We calculate U_T from half the range of the sectionally-averaged velocity through a cross section at the middle of the sill (section b3, see Figure 3.2). To create an ensemble of models with similar tidal excursions, it was necessary to account for the effects of tidal resonance in the inner basin when setting the amplitudes of the tidal forcing. The large inner basin and the narrow sill combine to create a system analogous to a Helmholtz resonator [Mehta and Özsoy, 1978; Miles and Lee, 1975]. Longer sills result in larger amplification of the sea surface height in the inner basin, which in turn increases the tidal velocities and tidal excursion over the sill. The longer sills also have a lag between the sea surface height amplitudes in the inner and outer basins, with a lag of approximately one hour for the 80 km sill model. We tune the amplitudes of the M2 and S2 forcing such that all models have similar tidal excursion to the 5 km sill model. We hold the M2 and S2 amplitudes at a 3:1 ratio, which creates spring tides twice as large as neap tides, and reduce the amplitudes until the maximum (spring) tidal excursion is approximately 20 km. Table 3.1 shows the tidal forcings used for each ensemble member and their resultant tidal excursions. The values of U_T on the sill in the five models range from 1.42 m/s to 1.58 m/s at spring tide and 0.67 m/s to 0.76 m/s at neap tide. Note that a reduction in the tidal amplitudes by a factor of up to 2.7 (for the 80 km sill model relative to the 5 km sill model) is required to match the tidal excursions.

The estuarine parameter space of Geyer and MacCready [2014] classifies estuaries according to their freshwater Froude number Fr_f and mixing parameter M. The freshwater Froude number represents the importance of river input and is defined as

$$Fr_f = \frac{U_r}{U_c} = \frac{Q_r/A}{\sqrt{g\beta s_{ocean} H}} \tag{3.2}$$

Table 3.1: Amplitudes of the M2 and S2 tidal forcing used for each model. The tidal excursion and U_T values shown are calculated using the section-averaged tidal velocities through section b3 (center of the sill) at the spring and neap tides closest to 10 October in the model run. The spring tidal excursion and U_T are calculated using the maximum range of the tidal velocity during the spring tide. The tidal amplitudes used in the 80 km sill model are 2.7 times smaller than in the 5 km sill model.

Model sill length	M2 amplitude [m]	S2 amplitude [m]	Spring tidal excursion [km]	Neap tidal excursion [km]	Spring U_T [m/s]	Neap U_T [m/s]
5km	2.25	0.75	20.50	9.69	1.47	0.69
10km	2.091	0.697	20.01	9.46	1.43	0.68
20km	1.8	0.6	19.92	9.44	1.42	0.67
40km	1.383	0.461	20.07	9.35	1.43	0.67
80km	0.83333	0.27777	22.10	10.60	1.58	0.76

where U_r is the velocity due to river flow, U_c is the maximum possible frontal propagation speed, Q_r is the river flow, A is the cross-sectional area, g is the acceleration due to gravity, β is the haline contraction coefficient, s_{ocean} is the maximum salinity, and H is the depth of the estuary. The mixing parameter represents the importance of tidal mixing and is defined as

$$M = \frac{C_D U_T^2}{\omega N_0 H^2} \tag{3.3}$$

where C_D is the drag coefficient, $\omega = 2\pi/T$ is the tidal frequency, and $N_0 = \sqrt{\beta g s_{ocean}/H}$ is the maximum possible buoyancy frequency. Because all of our models have the same cross-sectional areas in the sill and basins, and the same constant river flow, the Fr_f is the same for all ensemble members. Similarly, for the mixing parameter, all models have the same values for C_D and H. Therefore, any variation in M is due to the scale of the tidal velocity U_T. U_T varies over the spring-neap cycle, which leads to a range of values. However, we have chosen the forcing such that all models have a tidal excursion around 20 km, so the range of U_T will also be similar. Figure 3.3 shows the position of the idealized model ensemble on the estuarine parameter space, alongside some real estuaries for reference. The parameters for the idealized models are calculated at the center of the sill. The sills of all five models span nearly identical ranges of the parameter space. The model sills are also located close to the area of parameter space covered by Admiralty Inlet, the entrance sill to Puget Sound.

Although the models share the same location in the estuarine parameter space, they have another dimen-

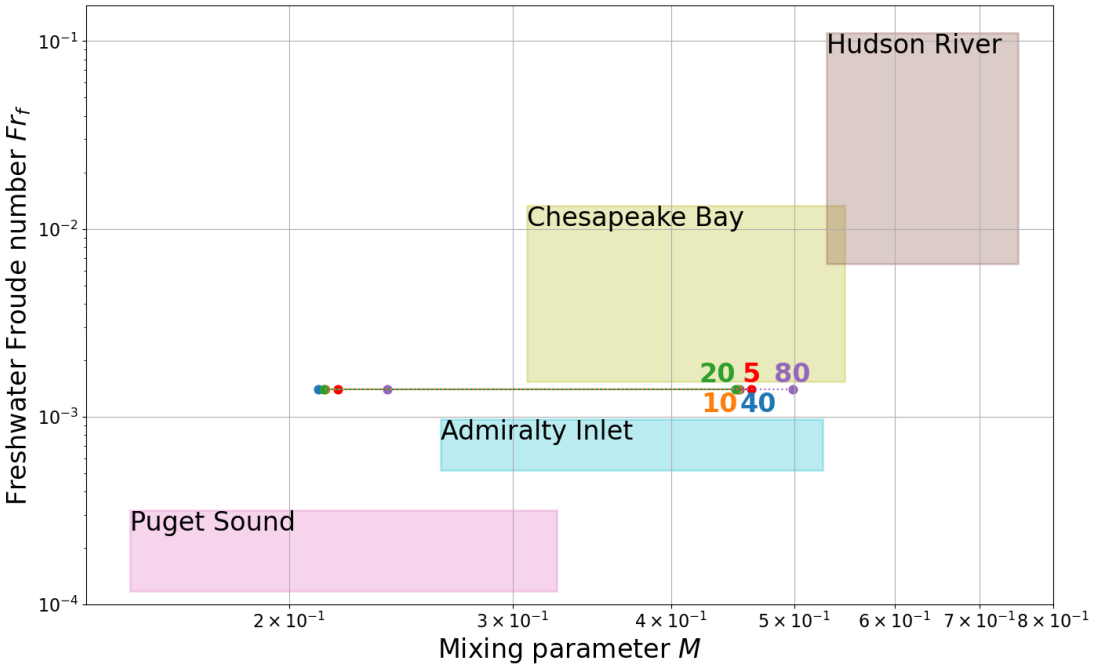

Figure 3.3: Location of idealized model ensemble in the estuarine parameter space, with real estuaries for reference. The range for each model shows the variation of the mixing parameter between neap and spring tide. The mixing parameters are calculated using the section-averaged tidal velocity through section b3 (center of the sill) at the neap and spring tides closest to 10 October in the model run. All five models, denoted by colored numbers for sill length in km, occupy a similar area of parameter space. Figure based on Geyer and MacCready [2014].

sionless parameter that differentiates them: the sill length to tidal excursion ratio L_S/L_T, where L_S is the length of the sill and L_T is the spring tidal excursion. This determines whether a sill is “long" or “short" relative to its tidal excursion, which we expect to affect its dynamics. Since the spring tidal excursion is approximately $20\ \mathrm{km}$ for all models, the L_S/L_T ranges from approximately $1/4$ for the shortest ($5\ \mathrm{km}$) sill to 4 for the longest ($80\ \mathrm{km}$) sill. For the $20\ \mathrm{km}$ sill model, the ratio is approximately 1. Likewise, Admiralty Inlet has $L_S/L_T \approx 1$, with a maximum tidal excursion and sill length both around $30\ \mathrm{km}$.

3.2.2 Exchange flow decompositions

To evaluate the estuarine exchange flow, we use three different decompositions: the Total Exchange Flow (TEF) [MacCready, 2011], the standard Eulerian decomposition [Lerczak et al., 2006; MacCready, 2011], and the Dronkers and van de Kreeke decomposition [Dronkers and van de Kreeke, 1986; Garcia and Geyer, 2023]. Each of these three decompositions can provide different information about the organization of the flow and salt transport mechanisms. We calculate these decompositions at fifteen cross sections, including five cross sections along the sill. The locations of the cross sections for each model are shown in Figure 3.2. Our focus will be primarily on the sections across the sill, labeled b1 to b5, with b1 at the seaward end of the sill and b5 at the landward end. We apply all three decompositions to the five idealized models over a period of four months (September-December in the one-year model run).

Total Exchange Flow decomposition

The first decomposition that we use is the Total Exchange Flow (TEF), following MacCready [2011], which uses binning in salinity classes instead of spatial coordinates to find the inflow Q_{in} and outflow Q_{out} through a cross section. To calculate the TEF decomposition, we bin the volume and salinity transport through a section into 1000 salinity classes, tidally average the transport in each class, and then group the transports into inflowing and outflowing layers using the dividing salinity method of Lorenz et al. [2019]. If there are multiple inflowing or outflowing layers they can then be combined into an equivalent two-layer flow. The flux-weighted salinities associated with the inflow and outflow are s_{in} and s_{out}, respectively. The salt transport through the section may then be decomposed as an inflow term $Q_{in}s_{in}$ and outflow term $Q_{out}s_{out}$, and we can write the salt budget for the estuarine volume V enclosed by a given cross section in terms of

the TEF variables:

$$\frac{d}{dt}\left\langle \int_v s dV \right\rangle = Q_{in} s_{in} + Q_{out} s_{out} \tag{3.4}$$

where s is the salinity and angle brackets $\langle\rangle$ denote tidal averaging. Assuming volume changes are negligible, we may substitute $Q_{in} + Q_{out} = -Q_r$ to rewrite the salt budget as

$$\frac{d}{dt}\left\langle \int_v s dV \right\rangle = Q_{in}\Delta s - Q_r s_{out} \tag{3.5}$$

where Q_r is the river flow and $\Delta s = s_{in} - s_{out}$. In this formulation $Q_{in}\Delta s$ represents landward salt transport due to the exchange flow and $Q_r s_{out}$ represents seaward salt transport due to river flow. If volume changes are important, the left-hand side of Equation 3.5 can be replaced by an "adjusted storage"

$$Storage^{adj} = \frac{d}{dt}\left\langle \int_v s dV \right\rangle - \frac{dV}{dt} s_{out} \tag{3.6}$$

as used in MacCready and Geyer [2024]. Unlike the standard Eulerian decomposition and the Dronkers and van de Kreeke decomposition, the TEF method does not explicitly separate the exchange due to gravitational circulation and tidal pumping, but rather gives a combined total Q_{in} which may arise from multiple physical processes [MacCready, 2011]. However, the primary mechanisms driving the exchange may be deduced from the correlation of the exchange flow with tidal variability. Additionally, the TEF decomposition allows us to differentiate between the exchange flow Q_{in} and the associated exchange flow salt transport $Q_{in}\Delta s$, which may be more relevant depending on the particular question being investigated.

Standard decomposition

For the standard decomposition, we decompose the subtidal salt transport through a section into a river term F_R, an exchange term F_E, and a tidal term F_T. The benefit of the standard decomposition is that it can separate spatially organized gravitational exchange from other processes. However, it is known to exhibit large fluctuations in the decomposition terms along the estuary due to interaction with topography [MacCready, 2011; Chen et al., 2012; Geyer and MacCready, 2014]. We use angle brackets $\langle\rangle$ to denote tidal averaging. A is the cross-sectional area which is divided into a fixed number of area elements dA, u is

the along-channel velocity, and s is the salinity. The river term F_R is calculated from the cross-sectionally and tidally averaged fields:

$$A_0 = \left\langle \int dA \right\rangle \tag{3.7}$$

$$u_0 = \frac{\left\langle \int u dA \right\rangle}{A_0}, \;\; s_0 = \frac{\left\langle \int s dA \right\rangle}{A_0} \tag{3.8}$$

$$F_R = u_0 s_0 A_0 \tag{3.9}$$

The exchange term F_E is calculated from the cross-sectionally varying and tidally averaged fields:

$$dA_0 = \langle dA \rangle \tag{3.10}$$

$$u_1 = \frac{\langle u dA \rangle}{dA_0} - u_0, \;\; s_1 = \frac{\langle s dA \rangle}{dA_0} - s_0 \tag{3.11}$$

$$F_E = \int u_1 s_1 dA_0 \tag{3.12}$$

The tidal term F_T is calculated from the remaining cross-sectionally and tidally varying fields:

$$u_2 = u - u_0 - u_1, \;\; s_2 = s - s_0 - s_1 \tag{3.13}$$

$$F_T = \left\langle \int u_2 s_2 dA \right\rangle \tag{3.14}$$

A salt budget for the estuarine volume V that is enclosed by the section can be written in terms of the standard decomposition terms:

$$\frac{d}{dt} \left\langle \int_v s dV \right\rangle = F_R + F_E + F_T \tag{3.15}$$

We expect that the river term F_R will be negative as it removes salt from the estuary. The exchange term F_E, which represents spatial correlations of velocity and salinity over the section, and the tidal term F_T, are both expected to be positive as they drive up-estuary salt flux. For the tidal term F_T, we further decompose into a lateral component F_{TL} and a vertical component F_{TV}:

$$F_T = F_{TL} + F_{TV} \tag{3.16}$$

We calculate the lateral component using the depth-mean tidal salinity and velocity:

$$u_{2L} = \frac{1}{H}\int u_2 dz, \;\; s_{2L} = \frac{1}{H}\int s_2 dz \tag{3.17}$$

$$F_{TL} = \left\langle \int u_{2L} s_{2L} H dy \right\rangle \tag{3.18}$$

where H is the height of the water column and y is the direction parallel to the cross section. The remainder makes up the vertical component:

$$u_{2V} = u_2 - u_{2L}, \;\; s_{2V} = s_2 - s_{2L} \tag{3.19}$$

$$F_{TV} = \left\langle \int u_{2V} s_{2V} dA \right\rangle \tag{3.20}$$

Partitioning the tidal term into laterally and vertically organized contributions can provide additional information about the physical processes involved. Lateral dominance could be indicative of horizontal flow separation, as explored in Willapa Bay in Banas et al. [2004]. Vertical dominance could instead point to stratified hydraulics, such as the river plume lift-off reviewed in Horner-Devine et al. [2015].

In addition to the sections shown in Figure 3.2, we also calculate the standard decomposition at a set of finely spaced cross sections around the sill, with one section every $320\ \mathrm{m}$ (i.e. along each u-grid line). These can then be combined to create an along-estuary profile of the standard decomposition terms.

Dronkers and van de Kreeke decomposition

The Dronkers and van de Kreeke decomposition is similar to the standard decomposition but uses a different order of averaging. Dronkers and van de Kreeke [1986] argue that the terms in this decomposition represent “local" and “nonlocal" contributions to the salt flux. The local salt flux is due to spatial correlations of velocity and salinity over the section, while the nonlocal salt flux, or tidal oscillatory salt flux, is due to shear dispersion that occurs within one tidal excursion of a fixed cross section. Garcia and Geyer [2023] calculated salt fluxes in an idealized numerical model of a tidally dominated estuary using both fixed and moving cross sections, and validated the result that all landward salt flux is ultimately due to shear dispersion. We denote subscripted quantities used in calculating the Dronkers and van de Kreeke terms with a prime $'$ to differentiate from the quantities used to calculate the standard decomposition, which are not the same. The river salt flux F_0 is calculated from the cross-sectionally and tidally averaged fields:

$$\bar{u} = \frac{\int udA}{A}, \;\; \bar{s} = \frac{\int sdA}{A}, \;\; Q = \int udA \tag{3.21}$$

$$u_0' = \langle \bar{u} \rangle \,, \;\; s_0' = \langle \bar{s} \rangle \,, \;\; Q_0' = \langle Q \rangle \tag{3.22}$$

$$F_0 = Q_0' s_0' \tag{3.23}$$

Note that u_0' and s_0' are slightly different from the u_0 and s_0 used to calculate F_R because the area averaging happens before the tidal averaging. The “nonlocal" or tidal oscillatory salt flux F_1 is:

$$u_1' = u - u_0', \;\; s_1' = s - s_0', \;\; Q_1' = Q - Q_0' \tag{3.24}$$

$$F_1 = \left\langle Q_1' s_1' \right\rangle \tag{3.25}$$

The local dispersive salt flux F_2 is:

$$u_2' = u - u_0' - u_1', \;\; s_2' = s - s_0' - s_1' \tag{3.26}$$

$$F_2 = \left\langle \int u_2' s_2' dA \right\rangle \tag{3.27}$$

Like the standard decomposition, the Dronkers and van de Kreeke decomposition terms can be used to form a salt budget:

$$\frac{d}{dt}\left\langle \int_v s dV \right\rangle = F_0 + F_1 + F_2 \tag{3.28}$$

3.2.3 Momentum balance

To supplement the exchange flow decompositions, we also compute a momentum balance for the inflowing and outflowing layers of the exchange flow. The x-momentum equation is

$$\frac{\partial u}{\partial t} + (\mathbf{u} \cdot \nabla) u = fv + \left[-g\frac{\partial \eta}{\partial x} - \int_z^0 g\beta \frac{\partial s}{\partial x} dz \right] + \frac{\partial}{\partial z}\left(A \frac{\partial u}{\partial z} \right) \tag{3.29}$$

where f is the Coriolis parameter, η is the sea surface height, and A is the eddy viscosity. The terms on the left-hand side represent the acceleration and advection, and the terms on the right are the Coriolis term, pressure gradient (including the effects of the sea surface slope and the horizontal salinity gradient), and the vertical stress divergence. We calculate the momentum balance terms for each cross section on the sill. For the pressure gradient term, we calculate the salinity and sea surface height gradients using the nearest grid points on either side of the section (the sections are aligned with the model u-grid). All other quantities are interpolated onto the section as necessary and derivatives are estimated using centered differences. We calculate the stress divergence from the u-velocity only without appending the bottom u-stress field. This excludes the stress divergence in the bottom cell, however the bottom cells are generally thin and have low velocities, which would reduce their importance in a flux-weighted average.

For the Coriolis, pressure gradient, and stress divergence terms, we calculate the term for each grid point on the section and then average into flux-weighted quantities for the inflow and outflow using a procedure similar to TEF. At every point in the section, the momentum balance terms are multiplied by the volume

transport through that point and then grouped into salinity bins. The volume transport and cross-sectional area of each salinity bin is also calculated. The bins are grouped into inflowing and outflowing layers using the dividing salinity method of Lorenz et al. [2019]. This gives the “transport" of momentum balance terms and the volume transport in each layer, from which we can determine transport-weighted average values for the momentum balance terms in each layer. If there are multiple inflowing or outflowing layers, we can then combine them into an equivalent two-layer flow with a single flux-weighted value for each of the inflow and outflow.

Because a given cell may switch between inflow and outflow over time, we do not calculate the acceleration term from the $\partial u/\partial t$ in each grid cell with the method described previously for the other terms. Instead, we use the TEF volume transports Q_{in} or Q_{out} divided by the cross-sectional area of the inflow A_{in} or outflow A_{out} to get the average inflow or outflow velocity U_{in} and U_{out}. We then use centered differencing to take the time derivative. The advection term $(\mathbf{u} \cdot \nabla)\, u$ is not calculated directly, but is estimated from the residual of the balance in each layer.

3.2.4 Along-channel salinity gradient

We also calculate the depth-mean salinity at the cross sections shown in Figure 3.2. The salinities are binned by depth into $2\ \mathrm{m}$ bins to create salinity profiles for each section, down to a common depth ($50\ \mathrm{m}$). These profiles are then averaged in depth to create a time series of depth-mean salinity. Using pairs of sections, we can also calculate the average along-channel salinity gradient in the portion of the estuary between the two sections, which is important for understanding the baroclinic pressure gradient.

3.3 Results and discussion

3.3.1 Salinity structure

Salinity contours on an along-estuary section are shown in Figures 3.4 and 3.5 for neap flood and spring flood, respectively. The outer basins have a similar stratification in all of the models, which is comparable to the ocean salinity boundary forcing, whereas the salinity of the inner basin varies greatly between models. The short $5\ \mathrm{km}$ sill model has a very salty inner basin, with maximum salinities reaching $31.5\ \mathrm{psu}$.

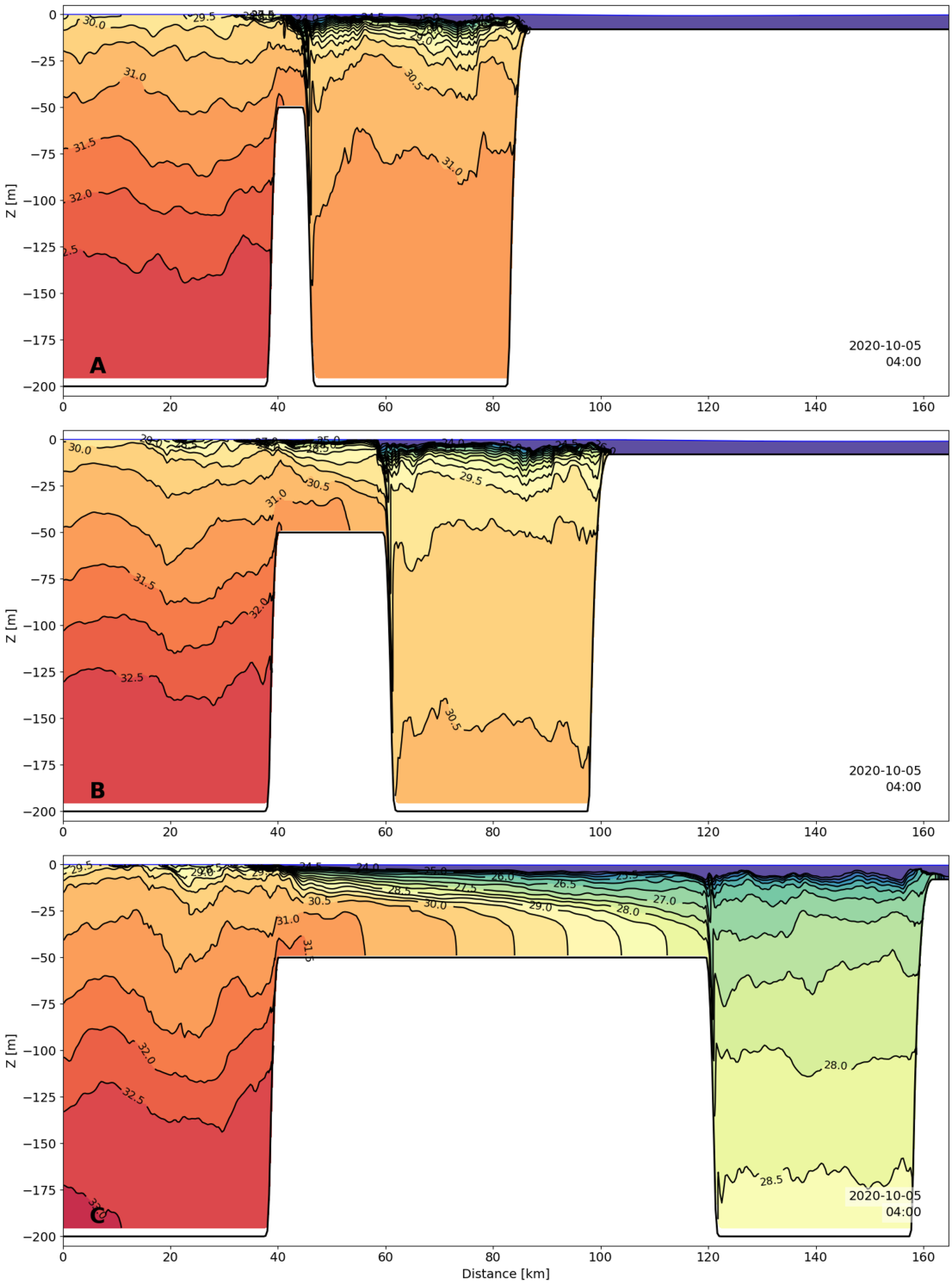

Figure 3.4: Along-estuary salinity sections at neap flood for the (A) 5 km, (B) 20 km, and (C) 80 km sill models. All panels have the same color scale. Contours are at 0.5 psu intervals, and the lowest contour is at 24 psu.

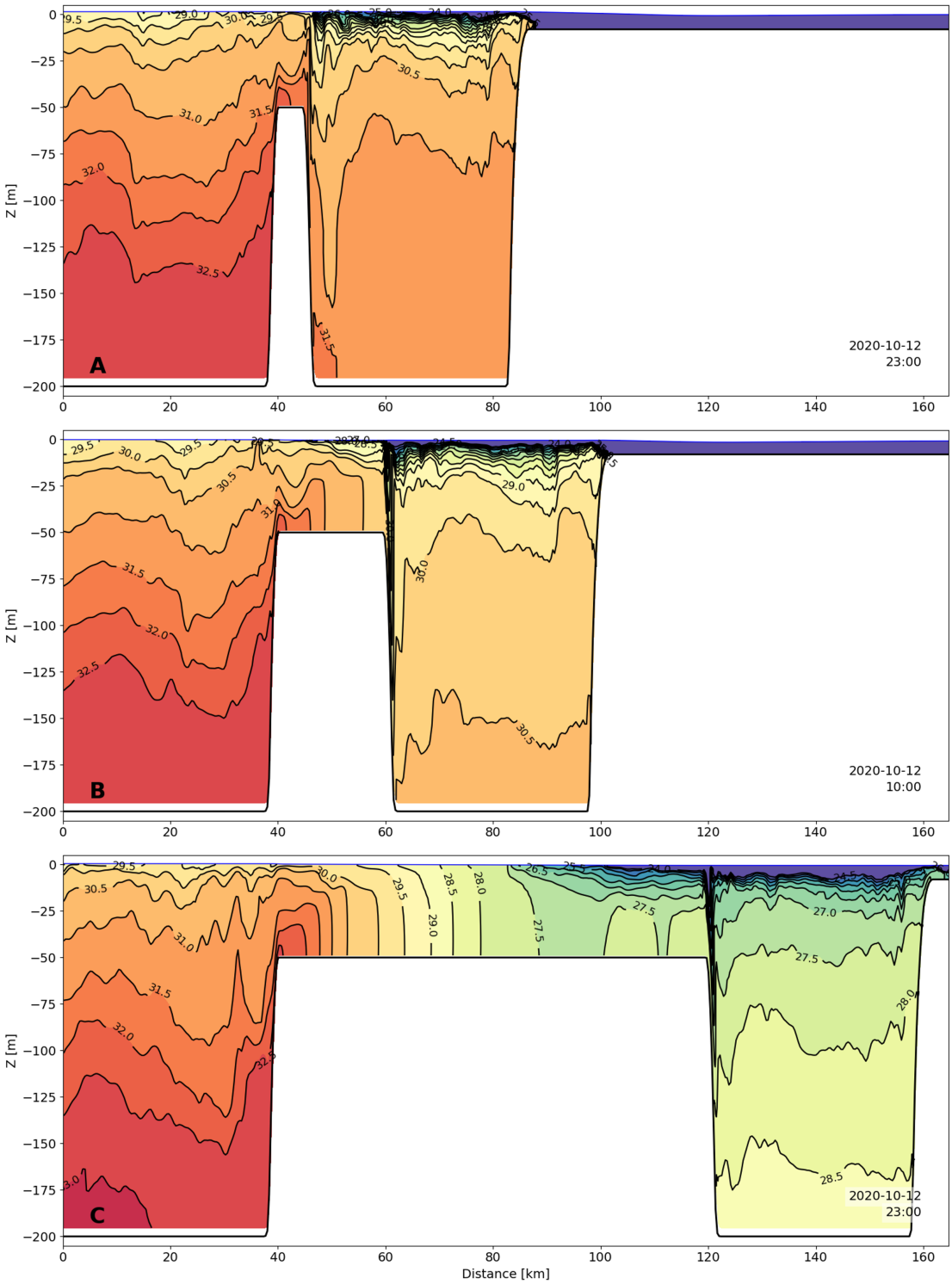

Figure 3.5: Along-estuary salinity sections at spring flood for the (A) 5 km, (B) 20 km, and (C) 80 km sill models. All panels have the same color scale. Contours are at 0.5 psu intervals, and the lowest contour is at 24 psu.

Compared to the 5 km sill model, the inner basin is approximately 1 psu fresher in the 20 km sill model, and approximately 3 psu fresher in the 80 km sill model. In both the inner and outer basins we see internal waves. Across the sill, the 5 km sill model has isohalines that are relatively flat, although there is a sharp plunging feature at the landward end of the sill. This is reversed on the ebb, although the feature at the seaward end of the sill is not as strong. Similar effects were found in observations and modeling of Knight Inlet Sill, where there was an asymmetry between the large internal lee waves that developed on the flood tide, and delayed, smaller-amplitude lee waves on the ebb tide [Klymak and Gregg, 2003]. In the 20 km sill model the isohalines begin to slope more across the sill. In the 80 km sill model, the isohalines slope strongly across the sill at neap tide, and are near vertical indicating well-mixed conditions on the spring tide. This portion of the estuary on the long sill resembles a partially mixed estuary.

3.3.2 Total Exchange Flow decomposition

Figure 3.6 shows time series of the TEF exchange flow salt transport $Q_{in}\Delta s$ across all five ensemble members for a single section b3 at the middle of the sill. Figure 3.7 shows time series of the TEF variables, also at section b3, which combine to make the salt transport. The results are similar for the other sections along the sill (not shown). Unlike the standard decomposition which is very sensitive to the section placement, the TEF salt transport has less spatial variability because it includes the contributions from both gravitational and tidal processes.

Figure 3.8 shows parametric plots of these quantities as a function of the spring-neap cycle, represented by Q_{prism}. In the shorter sill models (5 km-20 km) the exchange flow Q_{in} increases at spring tides, while the salinity difference Δs decreases slightly. The result of these competing effects is that the salt transport increases at spring tides for the 5 km and 10 km sill models, and decreases at spring tides for the 20 km sill model. As the sills become longer, there is increasing hysteresis in the behavior of Δs over the spring-neap cycle, and a stronger negative correlation between Δs and Q_{prism}. For the 40 km sill model, the exchange flow Q_{in} decreases at spring tides, so the net result is weaker salt transport at spring tides. Interestingly, the exchange flow Q_{in} in the 80 km model has a V-shaped curve on the parametric plot, such that at very high values of Q_{prism}, the exchange flow becomes larger again. This occurs when well-mixed conditions are present during the spring tide, as in panel C of Figure 3.5, and the exchange flow becomes noisier in time,

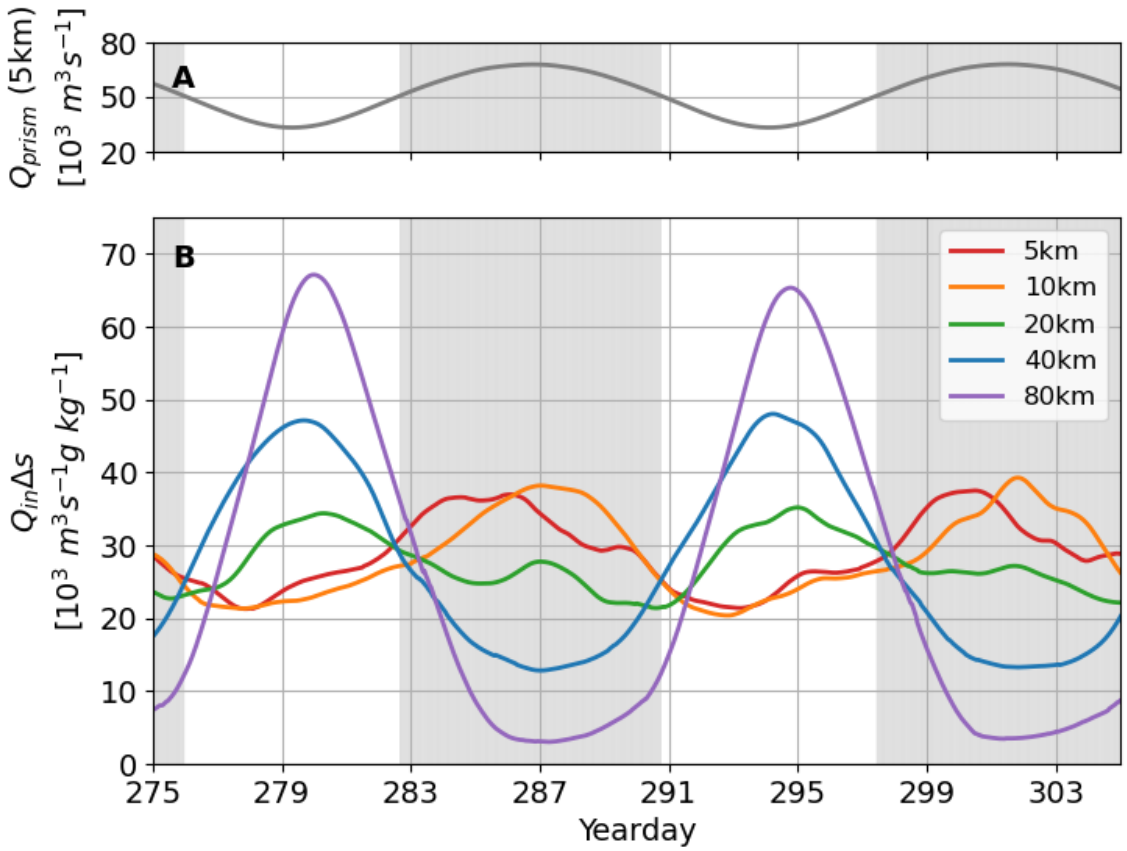

Figure 3.6: (B) Exchange flow salt transport at section b3 (middle of the sill) for all five models. Grey shading shows the timing of spring tide (peaks of Q_{prism} in panel A).

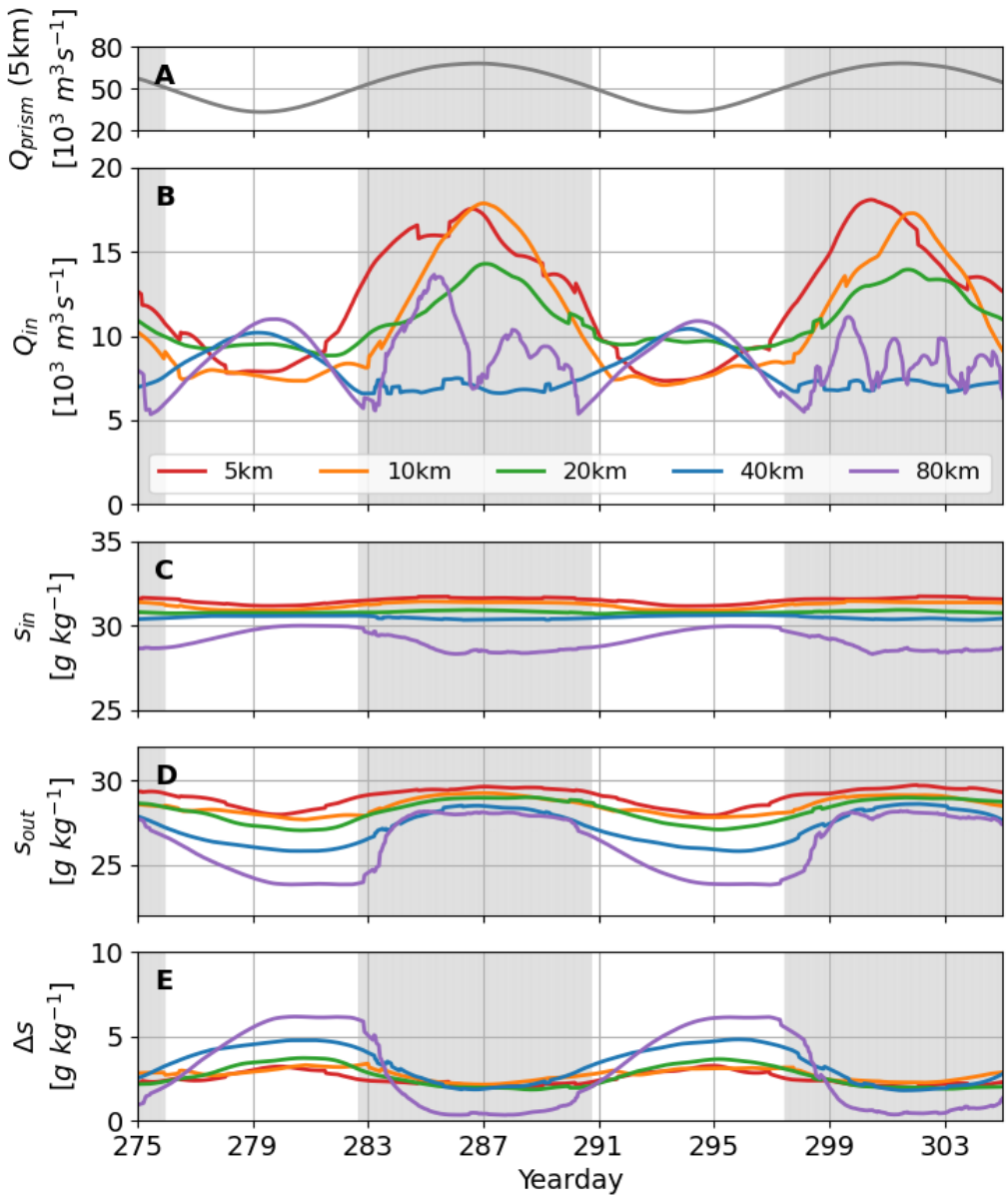

Figure 3.7: (B,C,D,E) TEF variables at section b3 (middle of the sill) for all five models. Panels C, D, and E have the same vertical scaling. Grey shading shows the timing of spring tide (peaks of Q_{prism} in panel A).

Table 3.2: TEF salt transport $Q_{in}\Delta s$ at section b3 for the five models, with a four-month average as well as neap and spring values. $Q_{in}\Delta s$ is also plotted in panel B of Figure 3.6, and the neap and spring values shown in this table correspond to the first neap and spring shown in that figure.

Model	Average salt transport $[10^3\ \mathrm{m^3 s^{-1} g\ kg^{-1}}]$	Neap salt transport $[10^3\ \mathrm{m^3 s^{-1} g\ kg^{-1}}]$	Spring salt transport $[10^3\ \mathrm{m^3 s^{-1} g\ kg^{-1}}]$
5km	28.94	24.48	35.23
10km	28.44	22.37	38.05
20km	28.05	33.21	27.60
40km	27.44	46.84	12.91
80km	26.37	63.37	3.13

which can be seen in the grey shaded areas in panel B of Figure 3.7. At these times the exchange flow has little salinity difference to act upon, and is therefore less “efficient" in producing salt transport [MacCready and Geyer, 2024]. The strong negative correlation of Δs with Q_{prism} means that the overall salt transport is smaller at spring tides. Table 3.2 summarizes the magnitude of the salt transport in the different models at spring tide, neap tide, and over a four-month average. We can see that the average salt transport is very similar across all models, but the longer sill models have more spring-neap variability.

MacCready and Geyer [2024] give scaling expectations for the size of the exchange flow Q_{in} and salinity difference Δs in the case of gravitational circulation and tidal pumping with variations in the tidal velocity scale U_T. Over spring-neap variation in U_T, i.e. when the timescale of variation is shorter than the adjustment timescale for the salinity gradient, both Q_{in} and Δs are expected to scale linearly with U_T in the case of tidal pumping. However, there is no strong rationale for this scaling, and we do not find any evidence for Δs scaling linearly with U_T (panel B of Figure 3.8), even when there is a positive correlation between U_T and the exchange flow (panel A of Figure 3.8). Alternatively, in the case of gravitational circulation, the exchange flow is expected to scale as $1/U_T$ and Δs as $1/U_T^2$. Across our five models, values of U_T are approximately the same, and have a factor of two variation over the spring-neap cycle, such that the tidal excursion is approximately $10\ \mathrm{km}$ at neap tide and $20\ \mathrm{km}$ at spring tide. Comparing our results from the TEF decomposition as shown in Figure 3.8 with the scaling expectations, we see that for all models, the salinity difference decreases with increasing tides, which is more consistent with the expectation for gravitational circulation. However, the exchange flow Q_{in} and the salt transport $Q_{in}\Delta s$ have a positive correlation with the strength of the tides for shorter sill and a negative correlation for longer sills. The transition occurs at

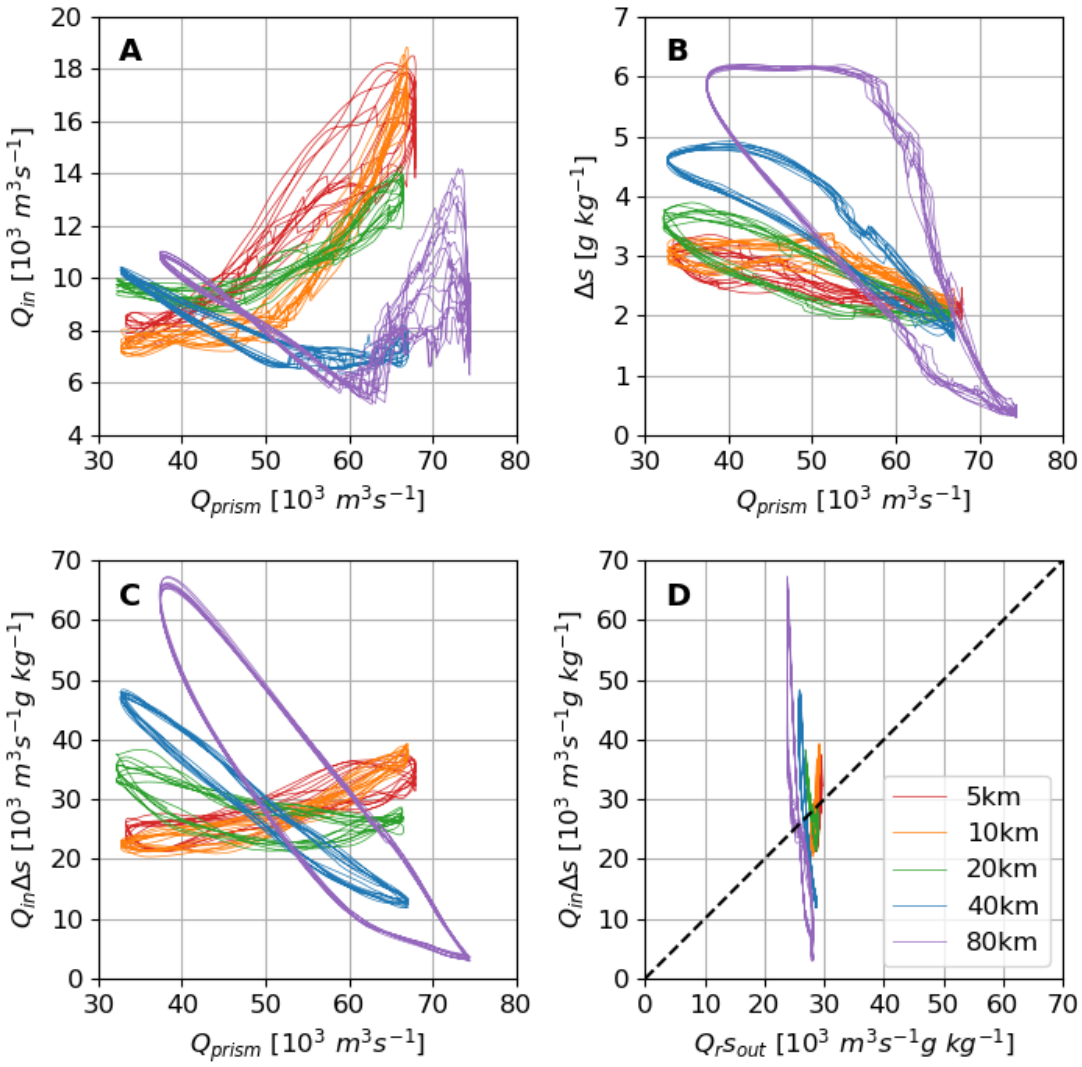

Figure 3.8: Parametric plots of (A,B) TEF variables Q_{in} and Δs, and (C) the exchange flow salt transport $Q_{in}\Delta s$, as a function of the spring-neap cycle, represented by Q_{prism}. (D) The exchange flow salt transport $Q_{in}\Delta s$ plotted against the river salt transport $Q_r s_{out}$, with a 1:1 dashed line. If there is no change in the total salt content of the landward basin, the parametric curves should lie on the dashed line. For all five models the quantities shown are for section b3 (middle of the sill).

the $20\ \mathrm{km}$ sill length, when the exchange flow has a weak positive correlation and the stratification has a weak negative correlation with Q_{prism}, resulting in a salt transport which varies very little over the spring-neap cycle. This is consistent with the results found by MacCready and Geyer [2024] at the seaward end of Admiralty Inlet (their figures 10 and 11), where the exchange flow is positively correlated with Q_{prism} and the salt transport is negatively correlated with Q_{prism}. Both the $20\ \mathrm{km}$ sill idealized model and Admiralty Inlet have $L_S/L_T \approx 1$, where L_S is the length of the sill and L_T is the spring tidal excursion.

The tidal conversion ratio Q_{in}/Q_{prism} measures how efficiently tidal inflow is transformed into net exchange [Chen et al., 2012]. Using time-averaged values of Q_{in} and Q_{prism} for section b3 (see Figure 3.8 panel A), we find tidal conversion rates of ~ 0.23 for the $5\ \mathrm{km}$ sill model, ~ 0.21 for the $10\ \mathrm{km}$ and $20\ \mathrm{km}$ sill models, and $\sim 0.15 - 0.16$ for the $40\ \mathrm{km}$ and $80\ \mathrm{km}$ sill models. Therefore, although the differences are not dramatic, the tidal conversion rate decreases as the sill length increases. Similarly, Chen et al. [2012] found that the long (as defined by salinity intrusion length) Hudson river had a lower tidal conversion rate ($\sim 0.20 - 0.45$) compared to the short Merrimack river (~ 0.65). Throughout the Salish Sea, including at Admiralty Inlet, MacCready and Geyer [2024] found a tidal conversion rate of about 1/3.5, or ~ 0.29.

Chen et al. [2012] and Garcia and Geyer [2023] showed the importance of the length of an estuary relative to its tidal excursion in determining the driving processes of up-estuary salt flux. Tidal processes become more dominant in shorter estuaries. We have expanded upon this result to show that for estuaries with sills, it is the length of the sill relative to the tidal excursion L_S/L_T that is important. When the sill is long, water at the middle of the sill never encounters the sharp bathymetry at the ends where tidal pumping is more likely to occur, whereas when the sill is short, a water parcel may pass over an end (or even both ends) of the sill on every tidal cycle.

Panel D of Figure 3.8 shows the exchange flow salt transport $Q_{in}\Delta s$ plotted against the river salt transport $Q_r s_{out}$. From Equation 3.5, if there is no change in the salt content of the landward basin (or more precisely the volume enclosed by section b3), these curves should lie on the 1:1 dashed line. However, the curves are near vertical, indicating that the storage term in the salt budget is significant and the system does not fully adjust over spring-neap time scales.

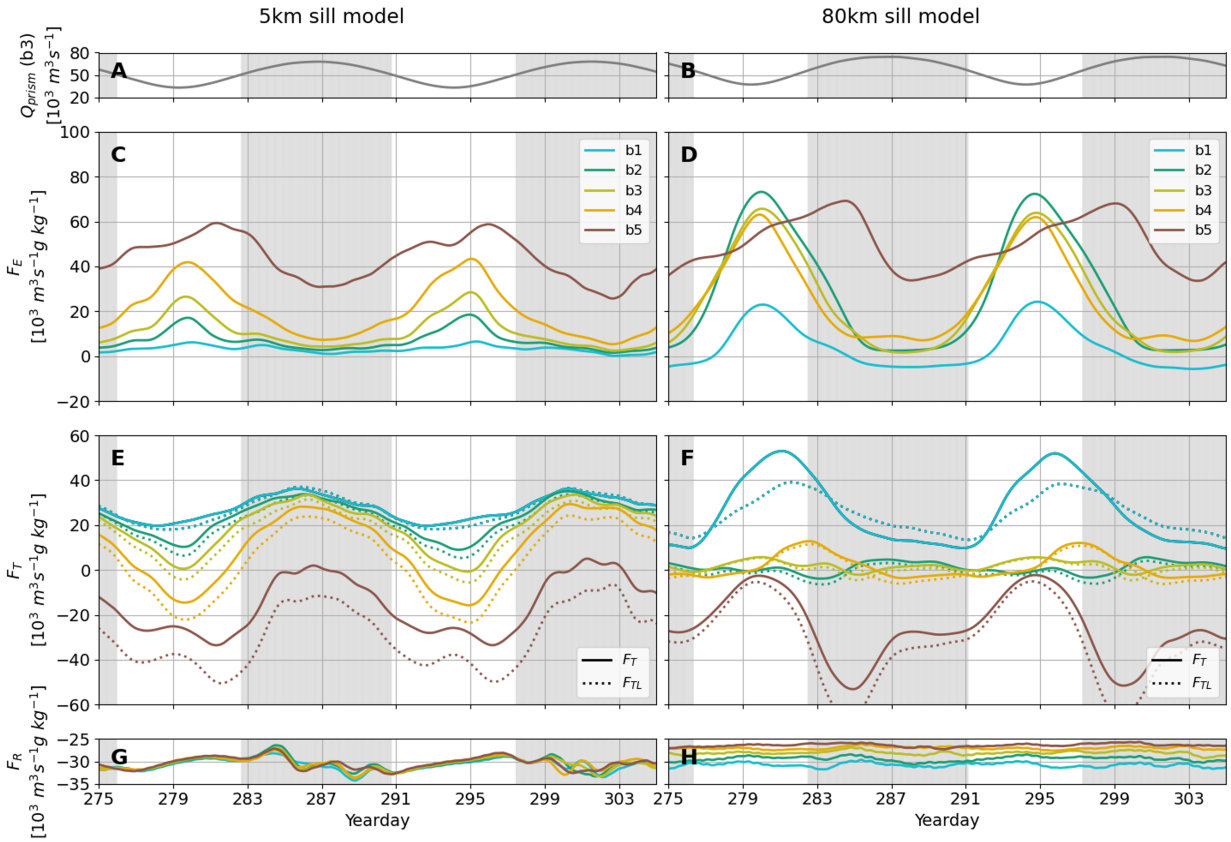

Figure 3.9: Standard decomposition time series at 5 sections along the sill for the 5 km and 80 km sill models. b1 is the seaward end of the sill and b5 is the landward end. The dotted lines in panels E and F show the lateral contribution F_{TL} to the tidal term F_T. Grey shading shows the timing of spring tide (peaks of Q_{prism} in panels A and B).

3.3.3 Standard decomposition and Dronkers and van de Kreeke decomposition

Figure 3.9 shows the results of the standard decomposition at five sections along the sill for the 5 km and 80 km sill models, alongside Q_{prism}, which represents the spring-neap cycle. The river term F_R is nearly constant across all sections and between models, although there is slightly more spread between the sections in the 80 km sill model.

Aside from the b5 (landward) section, the exchange term F_E is greatest at neap tides and much smaller at spring tides. The middle sections on the sill (b2 to b4) have a more exchange-driven salt flux compared to the seaward end (b1), and F_E on the sill at neap tides is twice as large in the longest sill model (80 km) compared to the shorter sill models.

In the short sill model the tidal term F_T is largest during spring tides across the sill (excluding the

landward end at section b5, which will be discussed below). This is expected as tidal pumping should increase when tides are stronger. For the longer sills, the tidal term is very small in the center of the sill. The tidal term is still important at the ends of the sill in the $80\ \mathrm{km}$ model. However, contrary to expectations, the tidal term is largest during the neap tide rather than spring, although, as discussed below, the standard decomposition is very sensitive to the cross section location. The dotted lines in panels E and F of Figure 3.9 show the lateral contribution to the tidal pumping term. At most of the sections, the tidal pumping term is primarily laterally organized. This could be due to horizontal flow separation and jet-sink structure at the ends of the sill, as well as Coriolis effects which cause the fresher outflow to flow preferentially along the northern side of the sill.

In all models there is negative F_T at section b5. This negative salt flux is likely associated with the sharp plunging feature at the landward end of the sill, as shown in Figures 3.4 and 3.5. Section b5 passes through these features where the salinity gradient ds/dx is reversed on the flood. The plunging isohalines result in a local freshening of the cross-sectionally averaged salinity on the flood tide. On the ebb tide (not pictured), this plunging feature is not present at the landward end of the sill, causing the average salinity there to be relatively higher. The result is that tidal cycles of the velocity and salinity fields are negatively correlated, leading to negative tidal salt transport. A similar effect has been found in the Hudson river, where counter-gradient tidal salt flux occurs at a deep hole approximately $18\ \mathrm{km}$ upstream from the mouth, caused by the hydraulic response of the flow as it passes over the sharp bathymetry [Chen et al., 2012; Engel, 2009; Geyer and Nepf, 1996]. The inverse effect could also occur at the seaward end of the sill, which would reinforce the positive tidal salt transport, although it would likely be less important as the plunging features which occur at the seaward end on the ebb are less pronounced.

Figure 3.10 shows the exchange and tidal terms as a function of the along-estuary distance for the $20\ \mathrm{km}$ sill model, calculated using the finely spaced cross sections placed at every grid cell. The tidal and exchange terms F_E and F_T tend to mirror one another. At each end of the sill there is a sharp peak with positive tidal pumping at the seaward end and negative tidal pumping at the landward end, with the effect being more pronounced for the spring tides (dashed lines). The dotted vertical lines show the locations of the cross sections used for the salt transport decompositions, and we can see that the decomposition is highly sensitive to the placement of the sections. While we represent the negative tidal pumping at the landward

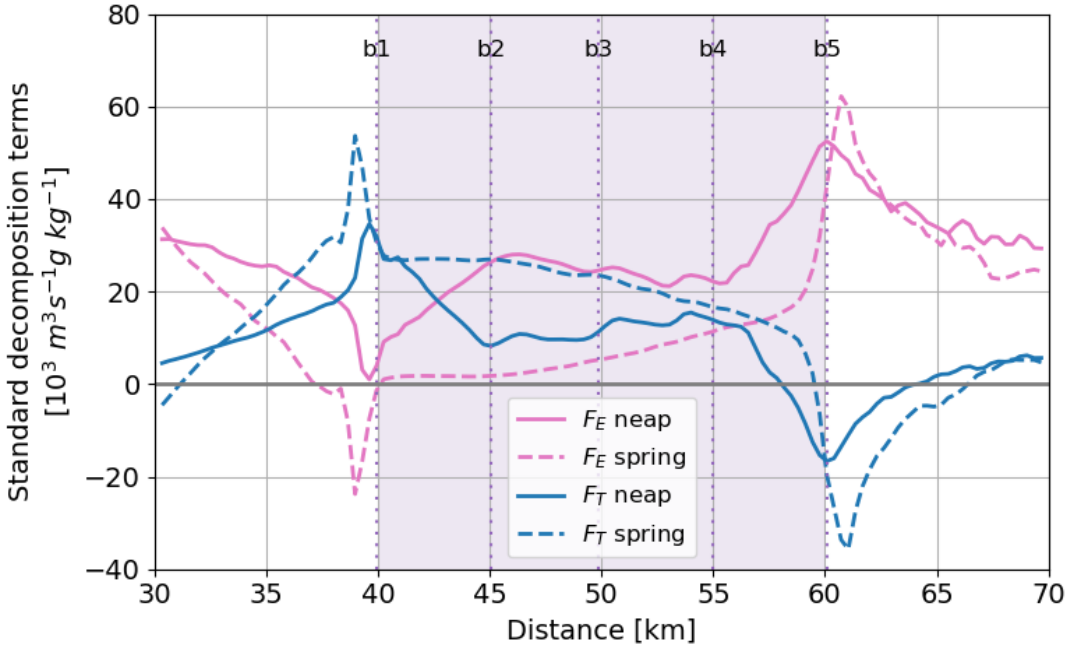

Figure 3.10: Along-estuary profile of the standard decomposition terms F_E and F_T around the sill for the 20 km sill model. Solid lines represent neap tides and dashed lines represent spring tides. Purple shading shows the location of the sill and vertical dotted lines show the locations of the sections b1-b5.

end of the sill (section b5) in Figure 3.9, we do not capture the negative exchange term F_E that would be seen if a section slightly seaward of b1 were chosen. This is consistent with previous studies which found high spatial variability in the partitioning of salt fluxes in the Eulerian reference frame, particularly in areas with sharp bathymetric gradients [MacCready, 2011; Chen et al., 2012; Geyer and MacCready, 2014].

It is important to note that the decomposition terms F_R, F_E, and F_T although generally associated with river flow, gravitational circulation, and tidal pumping, do not strictly differentiate between salt transport resulting from different physical mechanisms. Rather the decomposition separates different spatial and temporal organizations of the flow. The total salt transport remains approximately constant along the estuary, but the organization is modified along the sill. Similarly, Geyer and Nepf [1996] showed that tidal pumping is only locally important in a partially mixed estuary and is not an independent mechanism. Instead, they argue that tidal pumping results from spatial distortion of the mean estuarine shear flow through halocline motion, which redistributes the total salt flux between the Eulerian and tidal pumping components.

The exchange term F_E does not capture the total salt transport $Q_{in}\Delta s$ calculated from the TEF decom-

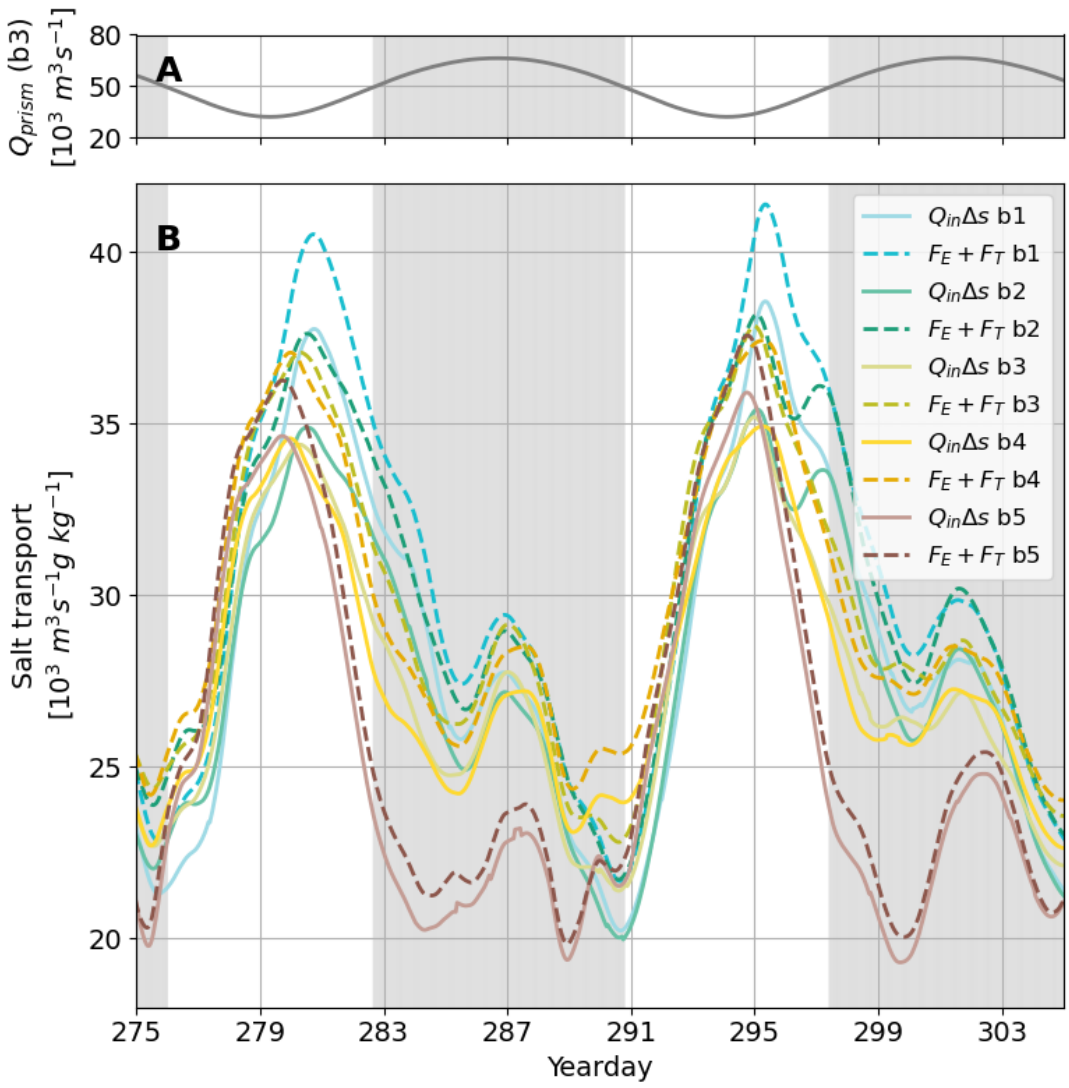

Figure 3.11: Comparison of the TEF salt transport $Q_{in}\Delta s$ with the combined standard decomposition terms $F_E + F_T$ for the 20 km sill model. b1 is the seaward end of the sill and b5 is the landward end. Grey shading shows the timing of spring tide (peaks of Q_{prism} in panel A).

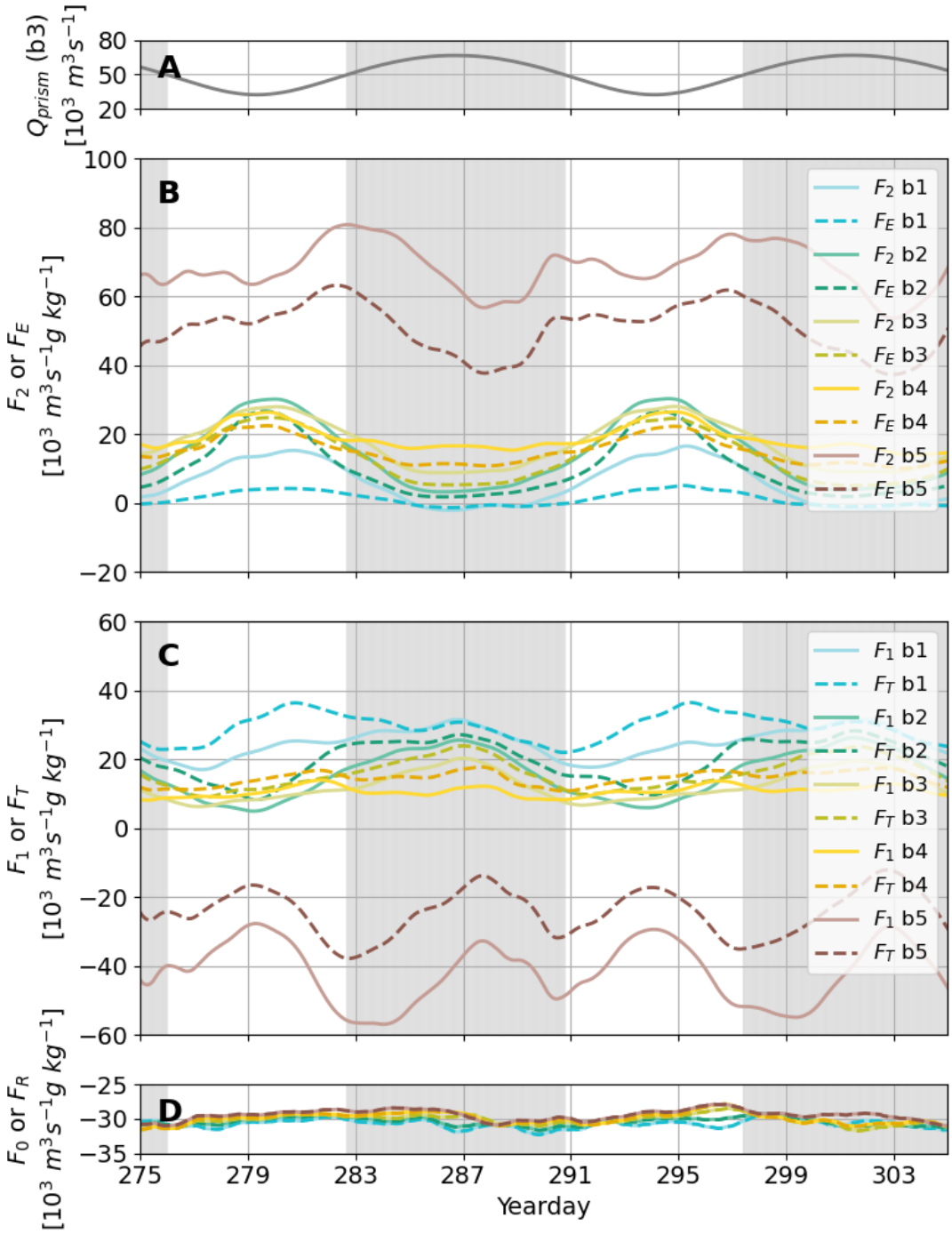

Figure 3.12: Comparison of the Dronkers and van de Kreeke decomposition terms with the standard decomposition terms for the 20 km sill model. b1 is the seaward end of the sill and b5 is the landward end. Grey shading shows the timing of spring tide (peaks of Q_{prism} in panel A).

position. However, the sum of both the exchange and tidal terms $F_E + F_T$ produces a very similar result to the TEF salt transport, as shown in Figure 3.11.

Figure 3.12 shows a comparison of the Dronkers and van de Kreeke decomposition with the standard decomposition for the $20\ \mathrm{km}$ sill model. The F_0 and F_R terms are nearly identical. However, the other terms differ slightly because of the different order of cross-sectional and tidal averaging. In the standard decomposition, the tidal oscillatory salt flux F_T is calculated from the tidally and cross-sectionally varying quantities, whereas in the Dronkers and van de Kreeke decomposition, the tidal oscillatory or "nonlocal" salt flux F_1 is calculated from the tidally varying and cross-sectionally averaged velocity and salinity. Similarly, the exchange term F_E is due to steady shear dispersion [Lerczak et al., 2006], while the local dispersive salt flux F_2 is due to both steady and oscillatory shear dispersion [Garcia and Geyer, 2023; Bowden, 1965; Taylor, 1953]. However, the F_T and F_1 follow similar patterns, as do the F_E and F_2. For the $20\ \mathrm{km}$ sill model, F_T is slightly larger than F_1, and F_E (which does not include the oscillatory shear dispersion) is slightly smaller than F_2. This shows that nonlocal processes, which occur within one tidal excursion of the section, significantly contribute to the tidal salt flux. At the seaward end of the sill (section b1), the tidal salt transport is almost entirely due to nonlocal processes during spring tides (grey shading).

3.3.4 Momentum balance

The primary momentum balance in a gravitationally-driven flow is expected to be between the baroclinic pressure gradient and vertical stress divergence. Time series of the flux-weighted momentum balances are shown in Figure 3.13. The forces are generally larger on the spring tide, regardless of the sill length or position on the sill.

In both models, we can see that the forces at the seaward and landward ends of the sill (panels C,D and G,H) are larger than the forces at the middle of the sill (panels E and F). Furthermore, the ends of the sill have a primary balance between the pressure gradient and advection, in both the inflowing and outflowing layers. Although there is no formal way of diagnosing tidal pumping from the momentum budget, this suggests that gravitational circulation is of secondary importance at the ends of the sill. The advection term is also likely to be more important when flow separation occurs. In contrast, the middle of the sill does have a balance between the pressure gradient and stress divergence.

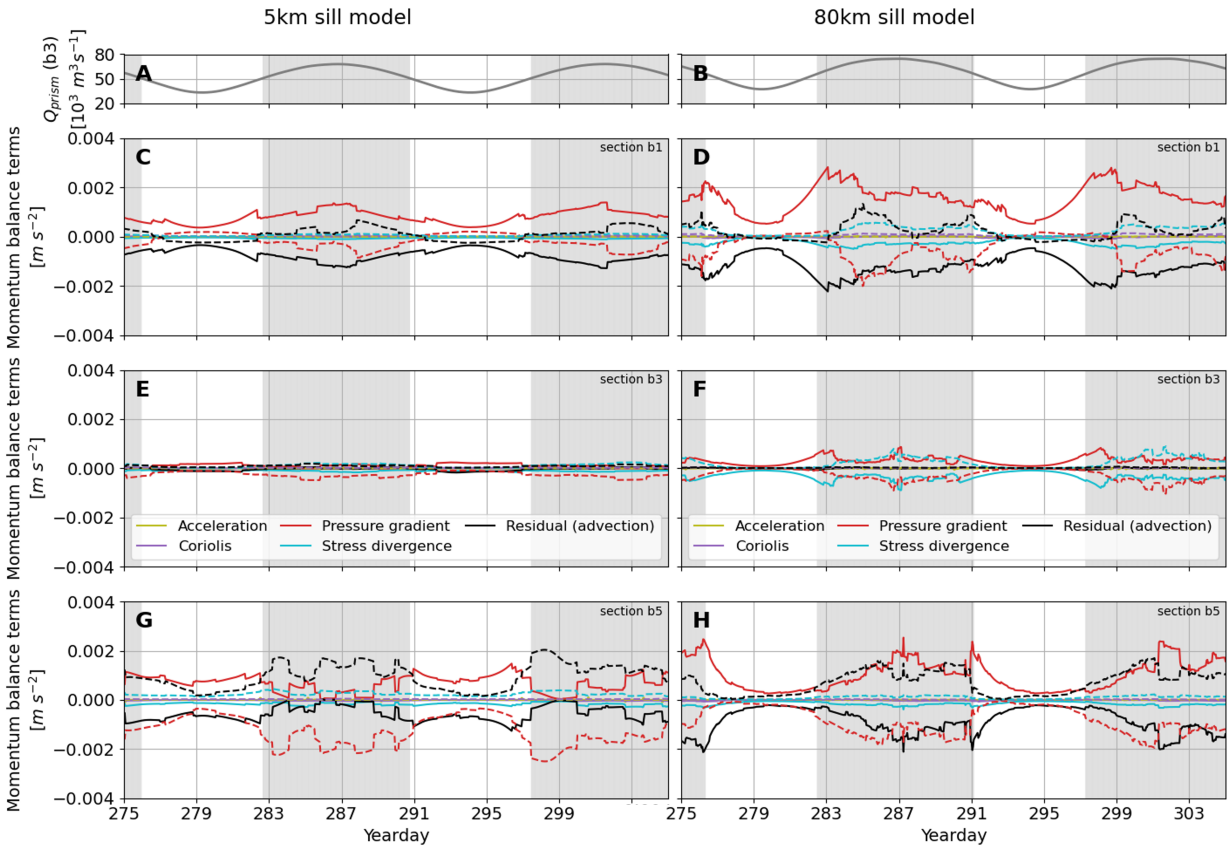

Figure 3.13: Flux-weighted momentum balances for the inflow and outflow defined by the TEF decomposition for the 5 km and 80 km sill models. Solid lines represent inflow and dashed lines represent outflow. Grey shading shows the timing of spring tide (peaks of Q_{prism} in panels A and B).

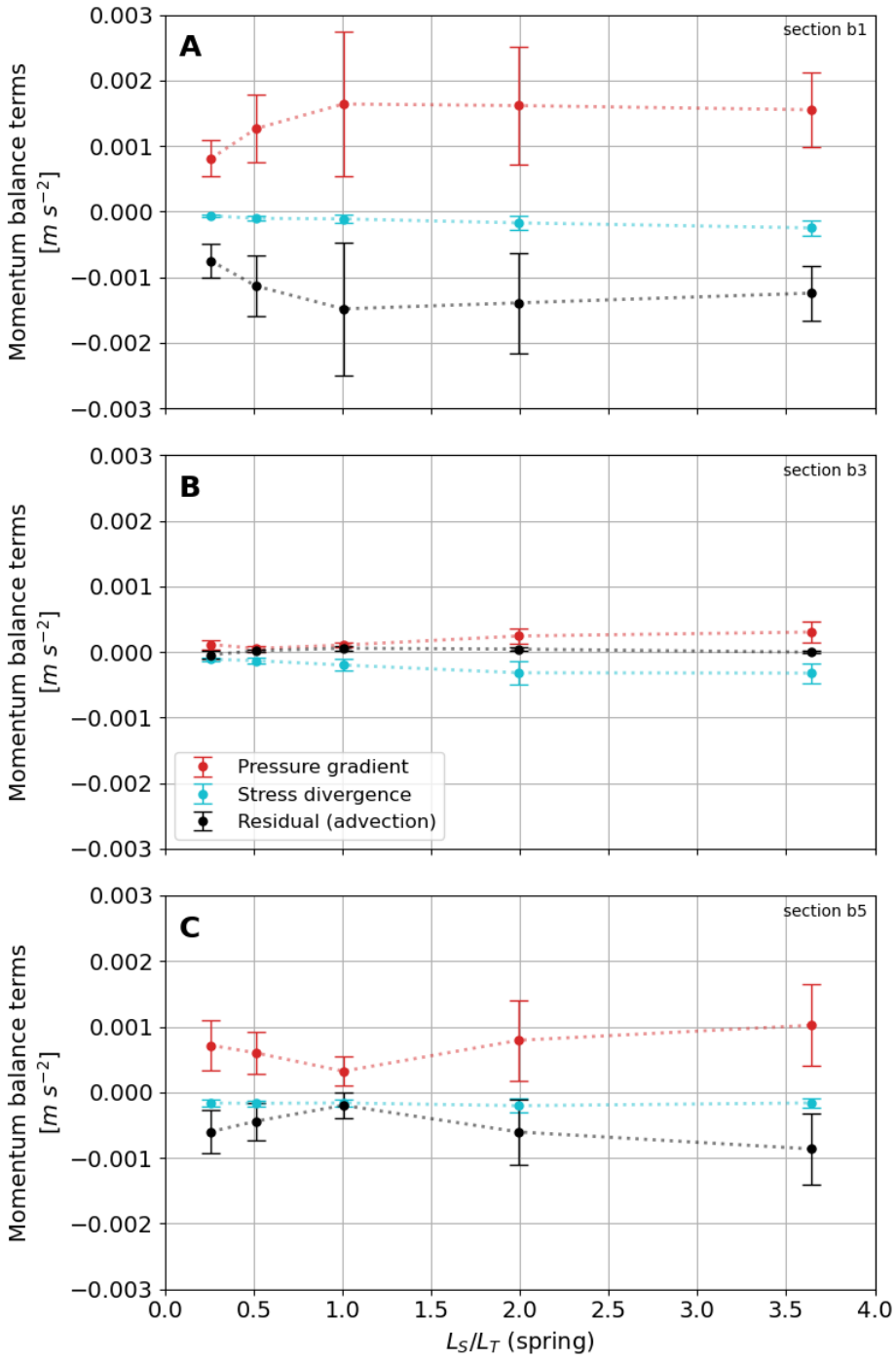

Figure 3.14: Flux-weighted momentum balance terms for the inflow only across all five models at the (A) seaward end of the sill section b1, (B) middle of the sill section b3, and (C) landward end of the sill section b5. Dots represent the mean for the term and bars show the standard deviation.

This pattern is found in all ensemble members, as shown in Figure 3.14, which gives a summary of the size of the momentum balance terms for the inflowing layer as a function of the nondimensionalized sill length L_S/L_T. The balance between the pressure gradient and the vertical stress divergence at the middle of the sill grows stronger with increasing sill length, indicating a strengthening of the gravitational circulation.

3.3.5 Along-channel salinity gradient

Looking at the depth-mean salinity in all five model ensemble members (Figure 3.15), we can see that all five models have similar conditions in the outer basin between 0 and $40\ \mathrm{km}$. The depth-mean salinity remains relatively constant (between $30\ \mathrm{psu}$ and $31\ \mathrm{psu}$) throughout the outer basin. For a steady, exchange dominated estuary, the along-estuary salinity gradient is expected to scale as

$$\frac{\partial \bar{s}}{\partial x} \sim \frac{s_{ocn} K}{H^2 c} \left(\frac{\bar{u}}{c}\right)^{\frac{1}{3}} \tag{3.30}$$

where K is the vertical eddy diffusivity, s_{ocn} is the oceanic salinity, H is the depth, c is the maximum two-layer internal wave speed, and $\bar{u}$ is the mean velocity due to river flow [MacCready, 1999]. Regardless of the sill length, all of our models have the same sill depth, ocean salinity, river flow, and tidal velocities, so it is sensible that the longitudinal salinity gradients would also be alike. Across the sill, the horizontal salinity gradients are slightly stronger for the shorter sills, but the large variation in sill lengths means that the salinity drop across the sill is greater for the longer sill models. Therefore, the inner basin salinity decreases with increasing sill length. Within the inner basin, the depth-mean salinity remains relatively constant across the five sections.

Figure 3.16 shows time series of the along-estuary salinity gradient ds/dx calculated from the difference in depth-mean salinity between cross sections on the sill. Note that because of the orientation of the estuary and coordinate system, we expect ds/dx to be negative, transitioning from salty ocean water at the western mouth to fresh river water in the east. For spring-neap variation in a system with a long adjustment time, it is expected that ds/dx would remain constant [MacCready, 1999; MacCready and Geyer, 2024].

The dashed lines in Figure 3.16 show the average salinity gradient ds/dx across the whole sill. Although the salinity of the inner basin in our models does not adjust significantly over spring-neap timescales, as shown in Figures 3.4, 3.5, and 3.15, ds/dx does vary over the spring-neap cycle. For the shorter sill models,

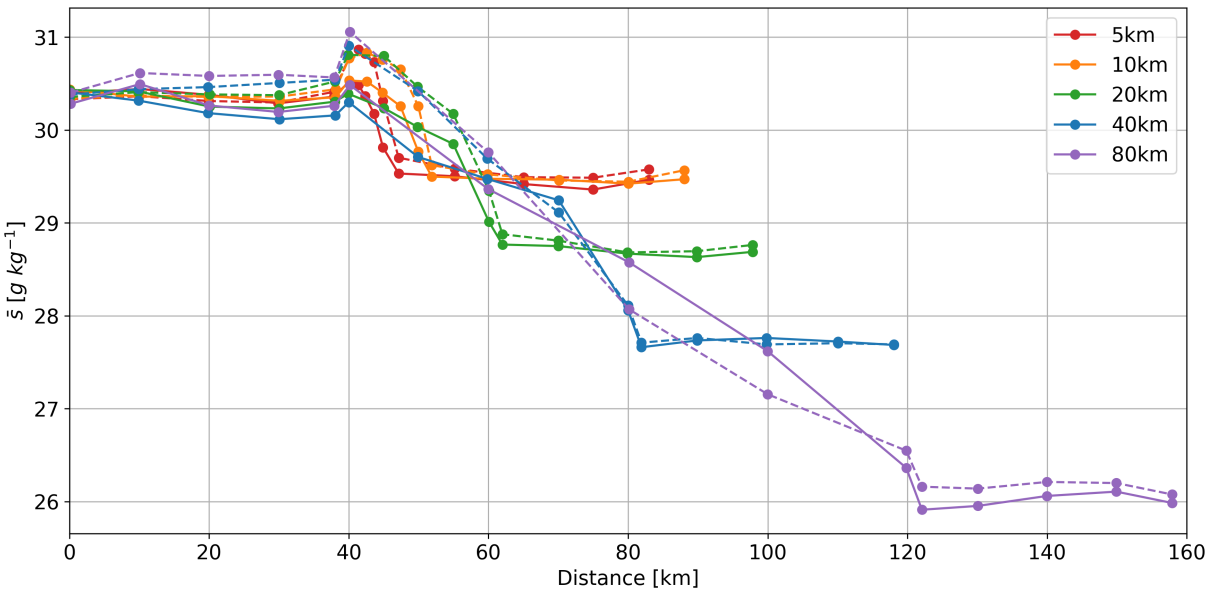

Figure 3.15: Depth-mean salinity $\bar{s}$ at fifteen sections along the model estuaries. Solid lines represent neap tides and dashed lines represent spring tides, with the dots showing the location of the sections. The sill starts at the 40 km mark for all five ensemble members.

ds/dx becomes weaker on the spring tide, which is consistent with end-to-end salinity gradient behavior at Admiralty Inlet [MacCready and Geyer, 2024]. The salinity structure may become more homogenized by mixing on the sill, which increases during spring tides. Contrarily, in the longer sill models, ds/dx across the sill becomes weaker at neap tides.

In addition to the differences between models in the end-to-end salinity gradient across the sill, different spring-neap variation of ds/dx is observed in individual regions of the sill, as shown by the colored lines in Figure 3.16. For the short 5 km sill, the three seaward segments of the sill have weaker ds/dx at spring tides, and in fact the salinity gradient reverses on the spring tide at the seaward end. For the longer 40 km sill, the segments in the middle of the sill have a greater magnitude of ds/dx at spring tides, while the ends of the sill have greater ds/dx at neap tides. In both cases, the overall salinity gradient follows the same trend as the segments in the middle of the sill.

Although we do not have theoretical predictions directly linking the spring-neap variation of ds/dx to gravitational circulation or tidal pumping mechanisms, we can observe different behavior in the salinity structure between the short and long sill models, as well as between the middle and ends of the sill. It

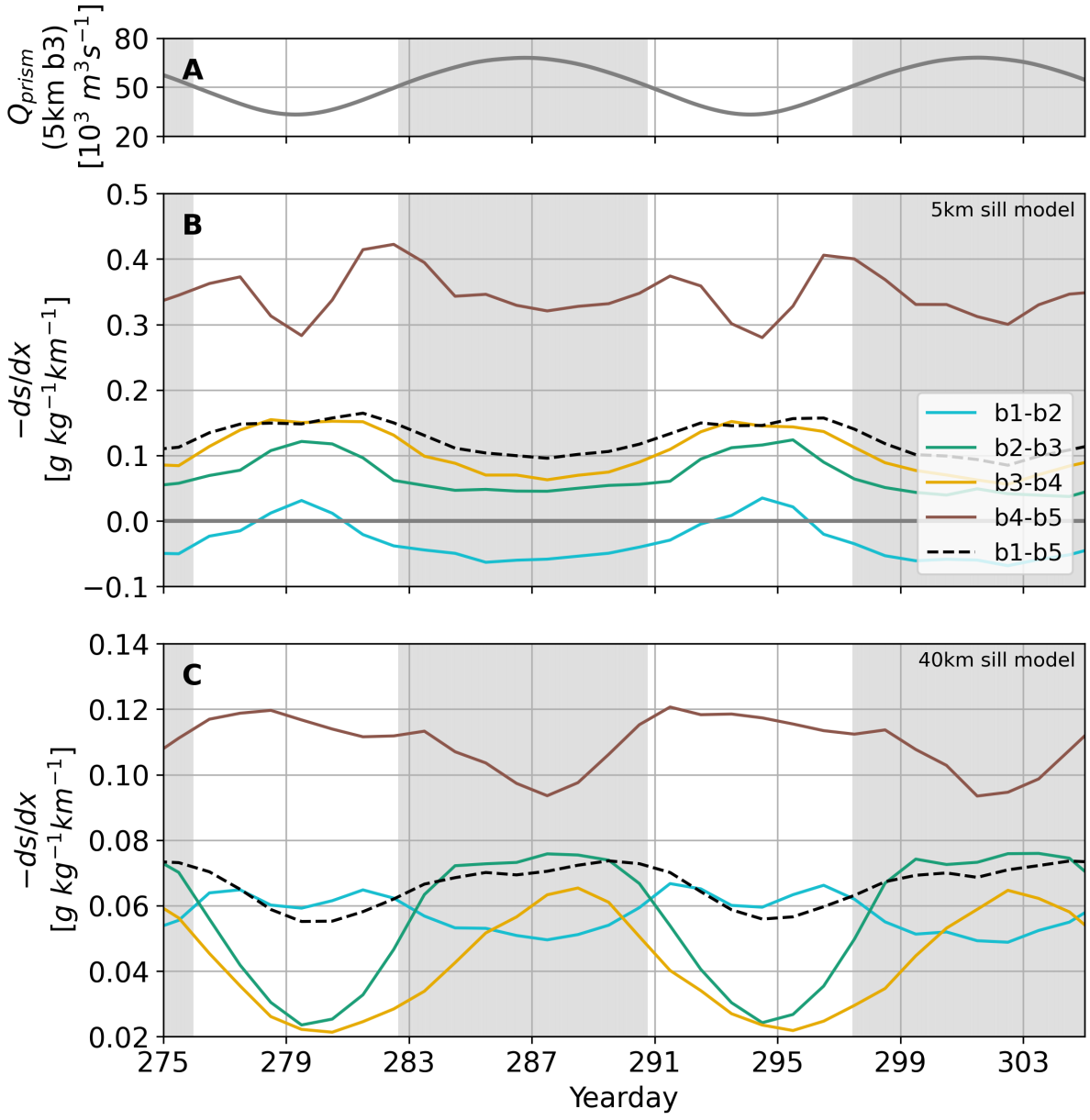

Figure 3.16: Along-estuary salinity gradient ds/dx calculated between pairs of sections for the (B) 5 km and (C) 40 km sill models. Note that the sign of ds/dx has been reversed on the figure y-axis, as the salinity is expected to become fresher as the model x-coordinate increases towards the river end of the estuary. Black dashed lines show the overall salinity gradient across the length of the sill. Note that the vertical scale in panel B is five times larger than in panel C. Grey shading shows the timing of spring tide (peaks of Q_{prism} in panel A).

is important to note that the results presented here use the tidally-averaged salinity gradient, which may not resemble the instantaneous salinity gradient. Previous studies have suggested that the tidally averaged salinity gradient may not be dynamically important in short estuaries [Jay and Smith, 1990; Ralston et al., 2010; Garcia and Geyer, 2023], and this could also be the case for our short sill models.

3.4 Summary and conclusions

Through multiple lines of evidence we have shown four clear patterns in the exchange flow at sills of varying lengths.

1. **At the ends of the sill, where abrupt bathymetric changes occur, tidal pumping is important, regardless of sill length.** The tidal pumping term F_T is large at both ends of the sill in all models, but is also locally negative at the landward end due to the phasing between the deepening surface layer and barotropic tides. Nonlocal processes occuring within one tidal excursion of the section make up a large part of the tidal salt flux.

   From the momentum balance we find that at the ends of the sill, the pressure gradient is not balanced by the vertical stress divergence as expected from a classical gravitational balance, but instead by advection. This is more consistent with tidal processes such as the jet-sink asymmetry where advection and flow separation are important. The forces are also much larger at the ends of the sill than in the middle.

2. **In the middle of the sill, gravitational exchange intensifies as the sill lengthens, and more spring-neap variability develops.** We see this effect in the standard decomposition, where F_E becomes larger in the longer sill models, especially at neap tides. Similarly, we also see that the total exchange flow Q_{in} at the middle of the sill becomes negatively correlated with Q_{prism} (larger on neap tide) as the sill lengthens. The longitudinal salinity gradient also transitions from being stronger at spring tides to stronger at neap tides with longer sill lengths. In the longer sill cases, because the tidal excursion is shorter than the sill length, the water over the middle of the sill does not interact with the sharp bathymetric changes at the sill ends. In the momentum balance, the pressure gradient is balanced by vertical stress divergence, as expected for gravitational circulation, and the forces become larger as

the sill gets longer.

3. **As the sill length exceeds the tidal excursion, there is a transition from tidally-driven to gravitationally-driven exchange.** From the Total Exchange Flow analysis, we found that the salt transport $Q_{in}\Delta s$ changes from increasing at spring tide to decreasing at spring tide around $L_S/L_T = 1$. Therefore, our main conclusion is that the sill length to tidal excursion ratio L_S/L_T is an important nondimensional parameter for describing the salt dynamics in estuaries with sills. Even when they lie in the same part of the estuarine parameter space, estuaries differentiated only by L_S/L_T have different exchange flow mechanisms and salt transport behavior.

4. **The inner basin becomes fresher as sill lengthens.** The average salinity gradient on the sill is approximately the same in all models, so with a longer distance to act over, the salinity difference between the ocean and inner basin increases.

Several avenues for future study that may also benefit from an idealized modeling approach readily present themselves. First, how would these results change as other dimensions of the sill, such as its height and width, are varied? The sill used in this study has a 50 percent horizontal constriction and 25 percent of the total depth. As the sill becomes more or less horizontally constricted, how does this affect the total tidal pumping and its lateral and vertical contributions? If the sill height is reduced, at what point will it cease to act as a sill, rendering the sill length to tidal excursion parameter L_S/L_T unimportant? Also, what ultimately controls the total magnitude of the salt flux? Is it determined by the sills or, as suggested by Dronkers and van de Kreeke [1986] and Geyer and Nepf [1996], is the tidal pumping simply a redistribution of the gravitational circulation set in the deep basins?

Chapter 4

Enhanced reflux at long sills extends estuarine residence times

Abstract

Particle tracking experiments in an ensemble of idealized numerical estuary models are used to investigate the effect of sill length on residence times in fjord estuaries. The estuary bathymetry in each model consists of two large, deep basins separated by a shallow, narrow sill. The five idealized models have sill lengths varying from $5\ \mathrm{km}$ to $80\ \mathrm{km}$, with a tidal excursion of $20\ \mathrm{km}$ in the sill region. Approximately 36 000 numerical particles are evenly distributed throughout the estuary and tracked using an offline particle-tracking algorithm for 120 days following their release. The particle tracks are used to calculate several transport time scales for the whole estuary and its inner basin. Longer sill lengths lead to more retention, and this effect is primarily due to particles reentering the domain. The Total Exchange Flow (TEF) decomposition is applied at cross sections along the estuary and used to calculate volume, freshwater, and saltwater flushing times. Efflux-reflux coefficients for the sill region, which characterize mixing and recirculation, are calculated from a box model constructed using the TEF variables. The amount of reflux is also estimated from the tidally-averaged particle tracks. In both cases, longer sills are found to have enhanced reflux, with the inner basin reflux fraction reaching ~ 0.5 for the $80\ \mathrm{km}$ sill model. A time-dependent version of the efflux-reflux coefficients is proposed, and reflux in shown to be greatest during spring tides, with longer sill models

exhibiting more spring-neap variability. The tidal excursion relative to the sill length regulates the duration that particles spend on the sill as well their maximum extent reached along the sill, which determines how many particles are able to transit the sill to the opposite basin.

4.1 Introduction

Transport time scales provide a useful way to describe the retention of water and tracers in estuaries and other aquatic systems. Understanding the flushing of estuaries has significant implications for predicting and managing water quality and the fate of contaminants. Depending on the system, materials of concern may include bacteria [Banas et al., 2015], pollutants from land-based runoff [Alahmed et al., 2022], treated and untreated wastewater [Premathilake and Khangaonkar, 2022; Wang et al., 2004], industrial effluent [Wang et al., 2004], waste from aquaculture sites [Brooks et al., 1999], oil spills [Rayson et al., 2016], or sediments [Ralston, 2022]. The renewal of water within the system also influences cycling of nutrients and dissolved gases [Monsen et al., 2002], thereby affecting the dynamics of primary productivity and the development of hypoxia and harmful algal blooms. Physical transport time scales, such as the residence time, characterize the circulation in a way that can be easily compared with other biogeochemical time scales to understand their interactions and relative importance [Monsen et al., 2002].

A variety of physical factors play important roles in determining the residence time and other transport time scales in a water body. Freshwater discharge, the strength of tides, and other external forcing such as winds, influence how quickly a volume is flushed. Within the estuary, stratification, mixing, and the estuarine circulation affect particle trajectories and how uniformly the water volume is renewed. There may also be interplay between the time dependence of each of these elements [Xiong et al., 2021b]. The geometry of the estuary dictates not only the size of the volume to be flushed, but also the circulation patterns and connectivity between different regions. Complex bathymetry may cause stagnant areas to form, or allow for processes such as hydraulic control or flow separation. In this study, we will focus on one specific type of bathymetric feature: shallow sills that separate deeper basins within the estuary. Sills are a common feature in fjords, where they may be formed by the terminal moraines of glaciers or areas of resistant bedrock. These sills can restrict the circulation between basins and with the ocean, and typically exhibit elevated tidal velocities. The length of sills varies widely across fjord systems around the world, from hundreds of

meters up to tens of kilometers, such as Admiralty Inlet at the entrance to Puget Sound. We are interested in developing a rigorous understanding of how sill lengths affect transport time scales.

Transport time scales can be calculated and expressed in various ways, making a precise definition essential for understanding the implications of the specific measure used. First, is the time scale represented as a single value for the entire system, or is there a distribution of time scales that varies in space and/or time? While a single integrated value may be easier to estimate and compare across systems, it may also obscure important information about the processes driving renewal or areas that are more stagnant or retentive compared to the estuary as a whole. We can additionally distinguish between time scales derived from an Eulerian formulation, which considers transport through the boundaries of the domain, and Lagrangian techniques that track water parcel trajectories over time. Many transport time scales incorporate strong assumptions about the system. For instance, the flushing time, defined as the ratio of a system's volume to the flow rate through it ($T_F = V/Q$) is most meaningful for a well-mixed system, where it may be interpreted as the e-folding time of water in the volume. In real estuaries, the e-folding time is often longer than the flushing time due to conditions within the estuary, such as incomplete tracer homogenization [MacCready et al., 2021] or tidal eddies [Brooks et al., 1999]. The residence time refers to the duration a water parcel, starting at a given location in the estuary, takes to exit the volume, whereas the related measure of age quantifies the time a parcel has already spent in the estuary since entering at a boundary. In a well-mixed and steady-state system, the residence time at a given location considers a water parcel's future trajectory and generally does not depend on its origin. In contrast, a single location may have a distribution of ages, which characterize the past history of the water parcels, and are influenced by which boundaries the parcels enter through.

The return of water parcels into the estuary after their initial exit significantly complicates transport time scale measurements and requires consideration of multiple physical processes. This can be expressed in various ways. The distinction between strict residence time and residence time, as defined by Delhez et al. [2004], relies on whether the time of a parcel's first or final exit from the volume is counted as its residence time. Similarly, the exposure time measures the total duration that a parcel spends in the estuary, regardless of gaps between subsequent entries. In the tidal prism method for estimating flushing times for systems primarily flushed by tides, a return flow factor must be applied to account for the portion of the water that

exited the estuary on ebb tide and then returned on the flood tide [Monsen et al., 2002].

The significance of returning parcels may vary depending on the nature of the system and the definition of its boundaries. The nature of the domain boundaries and particularly, their “arbitrariness" is a critical factor in determining how to treat returning parcels [Delhez et al., 2004]. If the location of the boundary has physical significance or if parcels are transformed or exposed to distinct conditions upon exiting the domain, the strict residence time may be a more appropriate measure [Delhez et al., 2004]. These considerations are also relevant to the related concepts of returning particles, tracers, or dye.

Numerous processes can contribute to returning particle tracks. First, diffusion and advection of particles near the boundaries can cause them to exit and reenter the volume without traveling over long distances. In most estuaries, the tidal cycle is a major driver of particle returns. Even in the absence of any residual flow, particles will exit and reenter the volume over the tidal cycle, and the number of particles affected by this process depends on the length of the tidal excursion.

When considering the estuarine exchange flow, particle returns may be understood through the efflux-reflux theory of Cokelet and Stewart [1985]. In this tidally-averaged framework, some fraction of the water in the outflowing branch of the two-layer exchange flow is vertically mixed or advected to rejoin the inflow, and vice versa, typically in a dynamically active area, such as a sill. This recirculating fraction of the water is called the reflux, while the remaining fraction which continues in its original layer is called the efflux. Since the estuarine exchange flow is usually much larger than river flow, exchange flow controls estuary residence times [MacCready et al., 2021].

Reflux is often enhanced in regions with vigorous mixing, such as sills. Cokelet and Stewart [1985] describe fjord systems as a network of quiescent deep basins separated by energetic mixing zones at sills. The intensity of this mixing determines how much reflux occurs over the sill. Reflux is one of several processes that extend the residence time of an estuary. MacCready et al. [2021] proposed two hypotheses for why residence times in the Salish Sea are longer than the flushing time: reflux or incomplete homogenization within the estuary volume. Using tracer experiments in a box model of the Salish Sea, they found that both factors contribute to increased residence times, but incomplete homogenization is more important in the Salish Sea. The characteristics of sills and their interaction with the tidal cycle influence their transport capacity [Armi and Farmer, 1986; Farmer and Armi, 1986; Stigebrandt, 1977; Helfrich, 1995]. Using idealized models of

sills in glacial fjords, Bao and Moffat [2024] found that sill height influences the circulation regime, with implications for warming and glacial melting. Shallow sills were found to increase cooling by restricting inflow of warm ocean water, while also reducing the stratification, with the competition between these two effects determining the degree of submarine melting [Bao and Moffat, 2024]. In Chapter 3, we showed that the sill length to tidal excursion ratio plays a key role in determining the exchange flow mechanisms and salt transport behavior. The tidal excursion, which is the distance that a water parcel travels over a tidal cycle, also regulates whether water can transit the sill in a single flood or ebb tide, or whether it remains on the sill, experiencing mixing, over several tidal cycles. Therefore, the sill length to tidal excursion ratio is likely to affect residences times and connectivity between basins in fjord estuaries.

Our objective in this study is to investigate how variations in sill length control residence times and reflux in fjord estuaries, with implications for water quality and ecosystem function. We utilize an idealized model ensemble with estuaries of varying sill lengths, in combination with particle tracking experiments and exchange flow decompositions, to tackle this problem from multiple perspectives. In Section 4.2, we outline the idealized model ensemble, and residence time analysis procedures from both box model and Lagrangian formulations. In Section 4.3, we present and discuss the results. We will explore the following questions:

- How do residence times and other transport time scales vary with sill length?
- How significantly do returning particles and reflux affect retention?
- How does the tidal excursion influence the trajectories of particles on the sill?
- How do Lagrangian particle tracking results compare with calculations from box models?

In Section 4.4, we summarize the conclusions.

4.2 Methods

4.2.1 Idealized model ensemble

To study the effect of varying sill lengths on residence times, we use an ensemble of five idealized models developed using the Regional Ocean Modeling System (ROMS) [Shchepetkin and McWilliams, 2005]. The dimensions of the model estuaries are loosely based on the geometry of Puget Sound and its sill at Admiralty

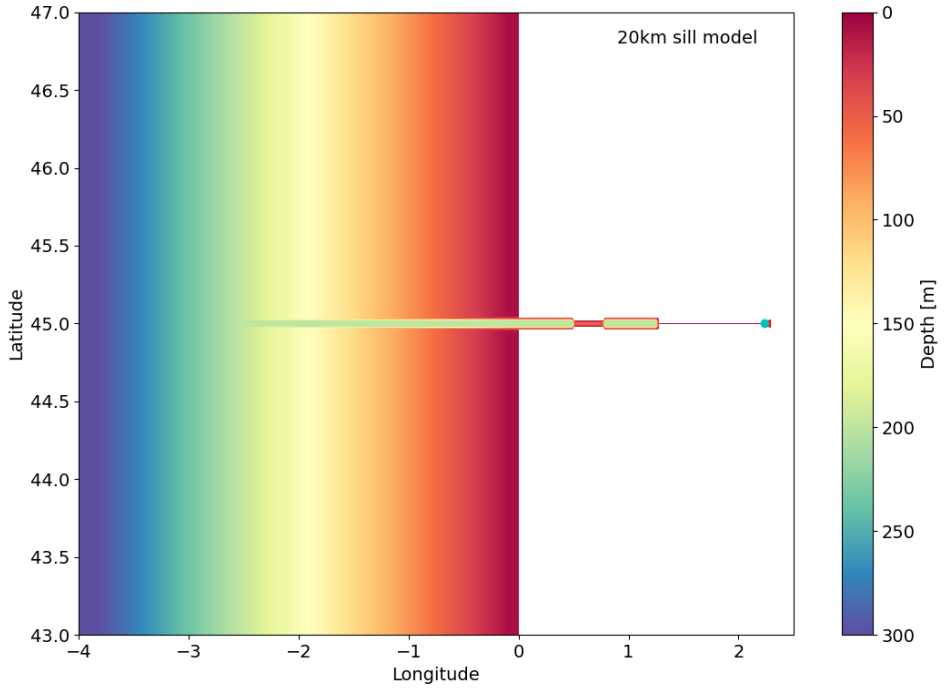

Figure 4.1: Idealized model grid for the $20\ \mathrm{km}$ sill ensemble member. Colormap shows bathymetry. Red line shows the river channel ($5\ \mathrm{m}$ deep), blue dot shows the cell where river input is added, and red triangle indicates the side of the cell where the point source is located and its flow direction. All other ensemble members have the same domain and coast bathymetry with the estuary and river located at the same latitude. See Figure 4.2 for the estuary bathymetry in all ensemble members.

Inlet. The model domain covers 4° latitude, centered at 45° N, and 6.5° longitude, with a north-south coastline at 0° longitude. The estuary is located at 45°N. The cell dimensions vary from $320\ \mathrm{m}$ in the estuary to $2.5\ \mathrm{km}$ at the oceanic boundaries, with 30 s-coordinate terrain-following vertical layers. Each model features an estuary with two basins, each $40\ \mathrm{km}$ long, $8\ \mathrm{km}$ wide, and $200\ \mathrm{m}$ deep, separated by a shallow and narrow sill that is $4\ \mathrm{km}$ wide and $50\ \mathrm{m}$ deep. The five models have different sill lengths: $5\ \mathrm{km}$, $10\ \mathrm{km}$, $20\ \mathrm{km}$, $40\ \mathrm{km}$, and $80\ \mathrm{km}$. The $20\ \mathrm{km}$ sill model grid (Figure 4.1) is designed to be most similar to Admiralty Inlet. A close-up of the estuary portion of the grid in all 5 models is shown in Figure 4.2. While the deep basins used here are more characteristic of fjords than coastal plain estuaries, they function mainly as less dynamically active regions surrounding the dynamically active sill.

The river flow is a constant $1000\ \mathrm{m^3\ s^{-1}}$ delivered at the landward end of the estuary by a single river

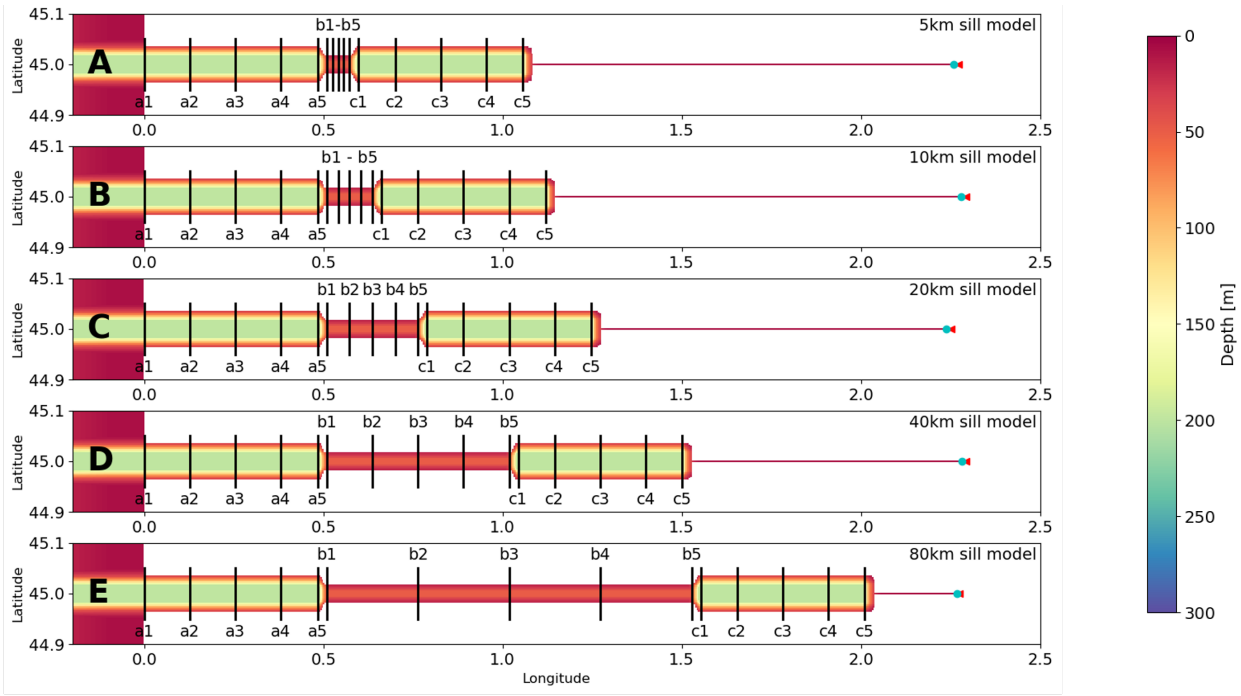

Figure 4.2: Model estuaries with (A) 5 km, (B) 10 km, (C) 20 km, (D) 40 km, and (E) 80 km sills. Black lines show the cross sections used for exchange flow decompositions. Colormap shows bathymetry, and color scale is the same as in Figure 4.1. Red lines show the river channels (5 m deep), blue dots show the cells where river input is added, and red triangles indicate the sides of the cells where the point sources are located and their flow direction. The inner and outer basins are 40 km long in all models. Each basin and the sill has five sections approximately evenly spaced across it, except that sections a5, c1, and c5 are shifted 2 km towards the middle of their respective basins (otherwise they would coincide with sections b1, b5, and the end of the estuary, respectively).

Table 4.1: Amplitudes of the M2 and S2 tidal forcing used for each model. The tidal excursion and U_T values shown are calculated using the section-averaged tidal velocities through section b3 (center of the sill) at the spring and neap tides closest to 10 October in the model run. The spring tidal excursion and U_T are calculated using the maximum range of the tidal velocity during the spring tide. The tidal amplitudes used in the $80\ \mathrm{km}$ sill model are 2.7 times smaller than in the $5\ \mathrm{km}$ sill model.

Model sill length	M2 amplitude [m]	S2 amplitude [m]	Spring tidal excursion [km]	Neap tidal excursion [km]	Spring U_T [m/s]	Neap U_T [m/s]
5km	2.25	0.75	20.50	9.69	1.47	0.69
10km	2.091	0.697	20.01	9.46	1.43	0.68
20km	1.8	0.6	19.92	9.44	1.42	0.67
40km	1.383	0.461	20.07	9.35	1.43	0.67
80km	0.83333	0.27777	22.10	10.60	1.58	0.76

with a depth of $5\ \mathrm{m}$. There is no atmospheric forcing and the water temperature is $10°$Cthroughout. The ocean boundary is forced with M2 and S2 tides, creating a simple spring-neap cycle. The ocean (west of $0°$longitude) is initialized with a vertical salinity stratification of $1\ \mathrm{psu}/50\ \mathrm{m}$, ranging from $30\ \mathrm{psu}$ at the surface to $34\ \mathrm{psu}$ at depths of $200\ \mathrm{m}$ and beyond. This stratification is also maintained as the ocean boundary condition. The estuary is initialized with entirely fresh water, which promotes a faster spin-up of an estuarine exchange flow. The model is run for one year, with the first eight months serving as spinup time, and the last four months allocated for analysis. Figure 4.3 shows the mean salinity in the estuary and in the inner basin over the full year and the final four months used in the analysis. The salinities adjust rapidly from their initial state, and most of the spinup is complete after the first four months. The model is not perfectly equilibrated after eight months, and there is some slight upward drift in the mean salinities during the final four months used for analysis. However, this drift is small compared to the spring-neap variation in the mean salinity, and we consider it to be acceptable for the purposes of this study.

The tidal excursion L_T refers to the distance that a water parcel travels along the estuary during a tidal cycle:

$$L_T = \frac{U_T T}{\pi} \tag{4.1}$$

where U_T is the amplitude of the tidal velocity and T is the tidal period. We determine U_T from half the range of the sectionally-averaged velocity through a cross section at the midpoint of the sill (section b3, see

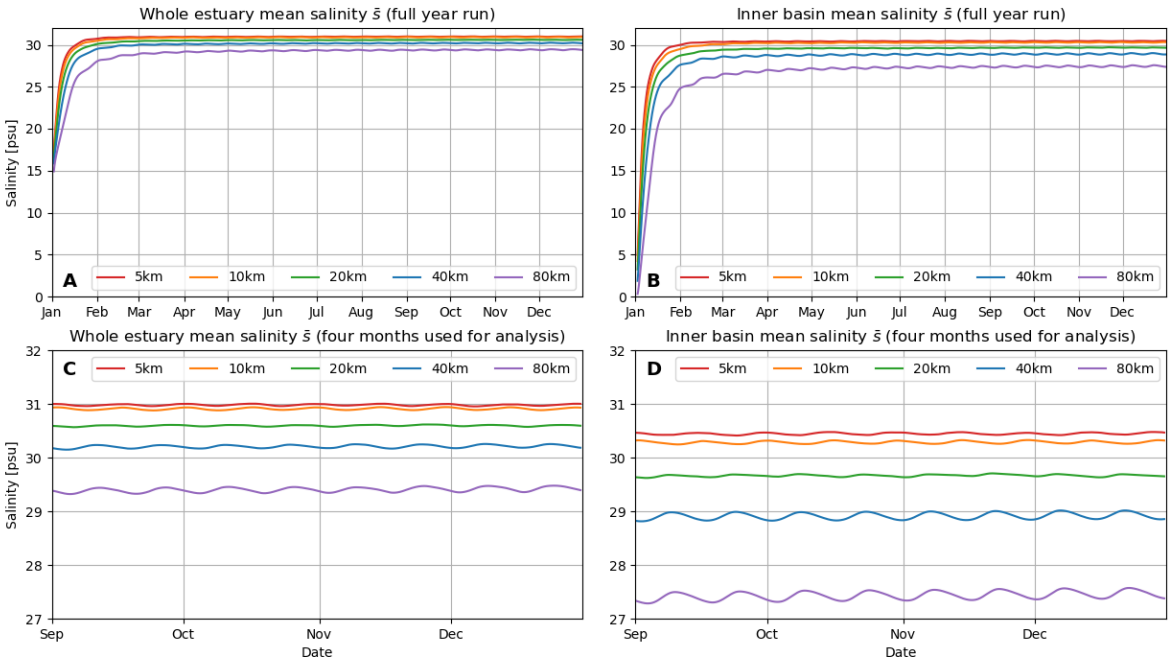

Figure 4.3: Mean salinity of (A,C) the whole estuary and (B,D) inner basin across the five models. Panels A and B show the full year-long idealized model run, while Panels C and D show the final four months which are used for the analysis in this project. The curves have been tidally averaged using the Godin filter. While there is still some drift in the salinity in the final four months, it is smaller than the effect of the spring-neap cycle, and most of the model spinup occurs in the first four months. The models are initialized with fresh water ($s = 0$) in the estuary.

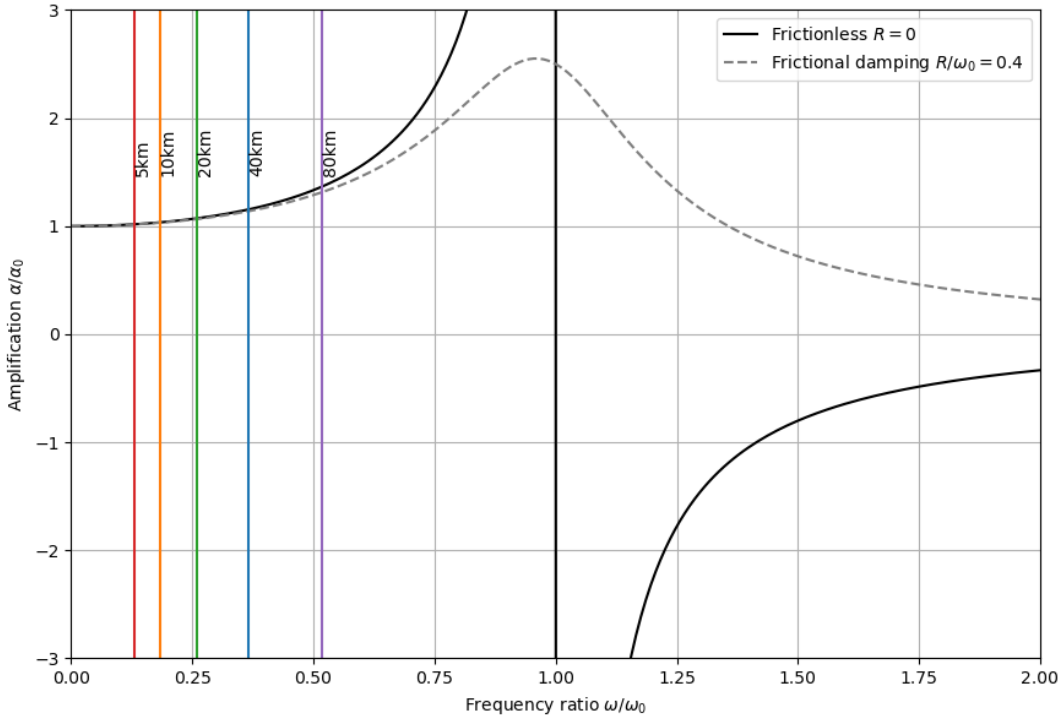

Figure 4.4: Theoretical resonance curves for a channel and bay system acting as a Helmholtz resonator. The solid black line shows the curve for a frictionless system, while the dashed grey line shows the an example with linear frictional damping in the channel. ω is the tidal forcing frequency and ω_0 is the natural resonant frequency of the bay. Vertical colored lines show the estimated frequency ratio for each of the five idealized models. The 80 km sill model is closer to resonance and therefore has greater amplification of the sea surface heights in the inner basin.

Figure 4.2). To create an ensemble of models with similar tidal excursions, it was necessary to account for the effects of tidal resonance in the inner basin when setting the amplitudes of the tidal forcing. The large inner basin and the narrow sill combine to produce a system analogous to a Helmholtz resonator [Mehta and Özsoy, 1978; Miles and Lee, 1975]. Approximating the sill with a rectangular cross section (50 m by 4 km) and the inner basin with a rectangular surface area (8 km by 40 km), we estimate the natural resonant periods of the system to be approximately 1.58 h, 2.23 h, 3.15 h, 4.46 h and 6.30 h, from shortest to longest sill. Figure 4.4 shows the theoretical amplification curves for tidal resonance in the inner basin, with and without friction (the example frictional curve shown is for linear frictional damping with $R/\omega_0 = 0.4$). The colored vertical lines show the frequency ratio between the tidal forcing (period of 12.21 h), and the natural frequency of the inner basin in the five models. The longer sill models are closer to resonance and therefore have greater amplification of the sea surface height in the inner basin. This in turn increases the tidal velocities and tidal excursion over the sill. Additionally, the longer sills also exhibit a lag between the sea surface height amplitudes in the inner and outer basins, with a lag of approximately one hour for the 80 km sill model. We tune the amplitudes of the M2 and S2 forcing such that all models have similar tidal excursion to the 5 km sill model. We hold the M2 and S2 amplitudes at a 3:1 ratio, which creates spring tides twice as large as neap tides, and reduce the amplitudes until the maximum (spring) tidal excursion is approximately 20 km. Table 4.1 shows the tidal forcings used for each ensemble member and their resultant tidal excursions. The values of U_T on the sill in the five models range from 1.42 m/s to 1.58 m/s at spring tide and 0.67 m/s to 0.76 m/s at neap tide. Note that a reduction in the tidal amplitudes by a factor of up to 2.7 (for the 80 km sill model relative to the 5 km sill model) is required to match the tidal excursions.

4.2.2 Box model analysis

Total Exchange Flow decomposition

We create a box model of the estuary to calculate flushing times and efflux-reflux coefficients. To do this, we need to calculate flow rates in and out of the volumes of interest. Since we expect that the estuarine exchange flow controls residence times, we use the Total Exchange Flow (TEF) decomposition to calculate the flow rates in and out of different parts of the estuary, following MacCready [2011]. The TEF method uses binning in salinity classes instead of spatial coordinates to find the inflow Q_{in} and outflow Q_{out} through a

cross section. To calculate the TEF decomposition, we bin the volume and salinity transport through a section into 1000 salinity classes, tidally average the transport in each class, and then group the transports into inflowing and outflowing layers using the dividing salinity method of Lorenz et al. [2019]. If there are multiple inflowing or outflowing layers, they are then combined into an equivalent two-layer flow. The flux-weighted salinities associated with the inflow and outflow are s_{in} and s_{out}, respectively. We calculate the TEF decomposition at fifteen cross sections, including five cross sections along the sill. The locations of the cross sections for each model are shown in Figure 4.2.

The exchange flow transports Q_{in} and Q_{out} can be combined with the river flow Q_r to create a volume budget for the estuary:

$$\frac{d}{dt}\left\langle \int_v dV \right\rangle = Q_r + Q_{in} + Q_{out} \tag{4.2}$$

where the sign convention is that Q_{out} is negative, while Q_{in} and Q_r are positive. The salt transport through the section can be decomposed as an inflow term $Q_{in}s_{in}$ and an outflow term $Q_{out}s_{out}$. We can then express the salt budget for the estuarine volume V enclosed by a given cross section in terms of the TEF variables:

$$\frac{d}{dt}\left\langle \int_v sdV \right\rangle = Q_{in}s_{in} + Q_{out}s_{out} \tag{4.3}$$

where s is the salinity and angle brackets $\langle\rangle$ denote tidal averaging. Assuming volume changes are negligible, we may substitute $Q_{in} + Q_{out} = -Q_r$ to rewrite the salt budget as

$$\frac{d}{dt}\left\langle \int_v sdV \right\rangle = Q_{in}\Delta s - Q_r s_{out} \tag{4.4}$$

where Q_r is the river flow and $\Delta s = s_{in} - s_{out}$. In this formulation $Q_{in}\Delta s$ represents landward salt transport due to the exchange flow, while $Q_r s_{out}$ represents seaward salt transport due to river flow. Equation 4.4 can also be rearranged to give a time-dependent version of Knudsen's 1900 relations [MacCready, 2011; Burchard et al., 2018].

Flushing times

The first timescale that we want to calculate is the flushing time, which is a single-valued, system-wide timescale. A simple expression for the flushing time is

$$T_F = \frac{V}{Q} \tag{4.5}$$

where T_F is the flushing time, V is the volume of the system, and Q is a characteristic flow rate through the volume. If the system can be modelled as a continuously stirred tank reactor, where the volume is instantaneously homogenized, then the flushing time is equivalent to the e-folding time of the original water present in the system. Alternatively, for a plug flow reactor, where a parcel of fluid passes through the volume without mixing, the flushing time is the time for the entire volume to be fully renewed. A real estuary will differ from both of these idealized models, as there is incomplete and spatially variable mixing, and the water parcels do not follow uniform or straightforward paths through the estuary.

In addition to the total volume flushing time, we also determine the flushing times for freshwater and seawater. These time scales are useful for understanding the retention of tracers which are known to originate from either oceanic or riverine sources. To accomplish this, we consider the water volume and flow rates as a mixture of freshwater ($s = 0$) and ocean water ($s = s_{ocn}$). The fraction of saltwater and freshwater in the volume can be derived from its average salinity $\bar{s}$:

$$V_f = \frac{s_{ocn} - \bar{s}}{s_{ocn}} V, \;\; V_s = \frac{\bar{s}}{s_{ocn}} V \tag{4.6}$$

$$V_f + V_s = V \tag{4.7}$$

Similarly, the flow rate can be separated into fresh and saltwater components, using the outflow salinity s_{out}:

$$Q_f = \frac{s_{ocn} - s_{out}}{s_{ocn}} Q, \;\; Q_s = \frac{s_{out}}{s_{ocn}} Q \tag{4.8}$$

$$Q_f + Q_s = Q \tag{4.9}$$

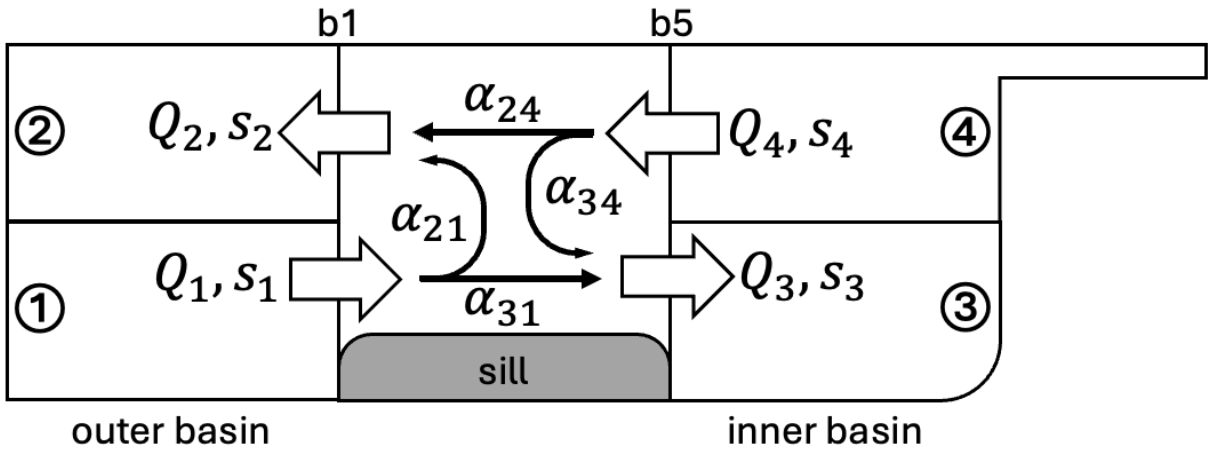

Figure 4.5: Diagram of the efflux-reflux box model framework.

Then the freshwater and saltwater flushing times may be expressed as

$$T_{Ff} = \frac{V_f}{Q_f} = \frac{s_{ocn} - \bar{s}}{s_{ocn} - s_{out}} \frac{V}{Q}, \;\; T_{Fs} = \frac{V_s}{Q_s} = \frac{\bar{s}}{s_{out}} \frac{V}{Q} \tag{4.10}$$

We calculate the volume, freshwater, and saltwater flushing times for the inner basin and whole estuary in the five different models. We use $-Q_{out}$ from the TEF decomposition (at section a1 for the whole estuary and section b5 for the inner basin) as the flow rate Q because it is the sum of $Q_{in} + Q_r$. For $\bar{s}$, s_{out}, and Q_{out}, we use the time average over seven spring-neap cycles. The constant volume V is calculated from the bathymetry assuming zero sea surface height, and $s_{ocn} = 34$ is the maximum ocean salinity in the models.

Efflux-reflux fractions

To calculate the efflux-reflux fractions, we use the TEF transports and salinities to create a box model of the sill region. The inputs and outputs to the sill region box come from four adjacent boxes representing the two-layer exchange flow in the inner and outer basins. The upper boxes are the fresher outflowing layer of the exchange flow, and the bottom boxes are the saltier inflowing layer. A schematic of the box model is shown in Figure 4.5.

Within the sill region, water may pass through and exit into the opposite basin in the same layer (efflux), or it may turn around and rejoin the other layer, returning to its original basin (reflux). Note that the terms efflux and reflux have not been used with consistent meaning throughout the literature, and the term efflux

is sometimes used to instead refer to the fraction of the deep inflow that is mixed upwards and rejoins the outflow (α_{21} in Figure 4.5)[MacCready et al., 2021; Xiong et al., 2021a; Engel and Stacey, 2024]. Here we follow the terminology and notation from Cokelet and Stewart [1985]. The efflux-reflux coefficients α define the how the two inputs to the sill region box are proportioned into the outputs. These coefficients must sum to 1, i.e. $\alpha_{21} + \alpha_{31} = 1$ and $\alpha_{24} + \alpha_{34} = 1$. By using conservation of mass and salt, we can deduce what these efflux and reflux fractions must be. The reflux fractions α_{21} and α_{34} give the fraction of the horizontal inflow that is mixed or advected into the other layer.

From volume conservation across the sill, we obtain two equations:

$$\alpha_{21}Q_1 + \alpha_{24}Q_4 = Q_2 \tag{4.11}$$

$$\alpha_{31}Q_1 + \alpha_{34}Q_4 = Q_3 \tag{4.12}$$

We can obtain two additional equations from a salt balance for the sill region:

$$\alpha_{21}Q_1 s_1 + \alpha_{24}Q_4 s_4 = Q_2 s_2 \tag{4.13}$$

$$\alpha_{31}Q_1 s_1 + \alpha_{34}Q_4 s_4 = Q_3 s_3 \tag{4.14}$$

This forms a system of four equations with the four unknown efflux-reflux fractions α:

$$\begin{bmatrix} Q_1 & Q_4 & 0 & 0 \\ Q_1 s_1 & Q_4 s_4 & 0 & 0 \\ 0 & 0 & Q_1 & Q_4 \\ 0 & 0 & Q_1 s_1 & Q_4 s_4 \end{bmatrix} \begin{bmatrix} \alpha_{21} \\ \alpha_{24} \\ \alpha_{31} \\ \alpha_{34} \end{bmatrix} = \begin{bmatrix} Q_2 \\ Q_2 s_2 \\ Q_3 \\ Q_3 s_3 \end{bmatrix} \tag{4.15}$$

The solutions for the efflux-reflux fractions are:

$$
\begin{aligned}
\alpha_{21} &= \frac{Q_2}{Q_1}\frac{s_2 - s_4}{s_1 - s_4} \\
\alpha_{24} &= \frac{Q_2}{Q_4}\frac{s_1 - s_2}{s_1 - s_4} \\
\alpha_{31} &= \frac{Q_3}{Q_1}\frac{s_3 - s_4}{s_1 - s_4} \\
\alpha_{34} &= \frac{Q_3}{Q_4}\frac{s_1 - s_3}{s_1 - s_4}
\end{aligned}
\tag{4.16}
$$

We use sections b1 and b5 (see Figure 4.2) as the horizontal boundaries of the boxes, and use the TEF variables at those sections to define the flow rates and salinities between the boxes, such that:

$$
\begin{aligned}
Q_1 = Q_{in}^{b1},\ s_1 = s_{in}^{b1} \\
Q_2 = Q_{out}^{b1},\ s_2 = s_{out}^{b1} \\
Q_3 = Q_{in}^{b5},\ s_3 = s_{in}^{b5} \\
Q_4 = Q_{out}^{b5},\ s_4 = s_{out}^{b5}
\end{aligned}
\tag{4.17}
$$

To calculate the efflux and reflux fractions, a single value is required for each of the flow rates and salinities. The TEF variables are averaged over seven spring-neap cycles. The assumptions of the efflux-reflux framework [Cokelet and Stewart, 1985] require that the following conditions on the salinity values are met:

$$
\begin{aligned}
s_4 \leq s_2 < s_1 \\
s_4 < s_3 \leq s_1
\end{aligned}
\tag{4.18}
$$

We perform small adjustments to the averaged TEF variables to ensure that volume and salt are exactly conserved within the sill region, and that the salinity conditions in Equation 4.18 are met. The only instance where the salinities need to be adjusted due to Equation 4.18 is in the $5\ \mathrm{km}$ sill model, where the original value of s_3 is slightly greater than s_1. We follow the adjustment procedure of Hager et al. [2022], which

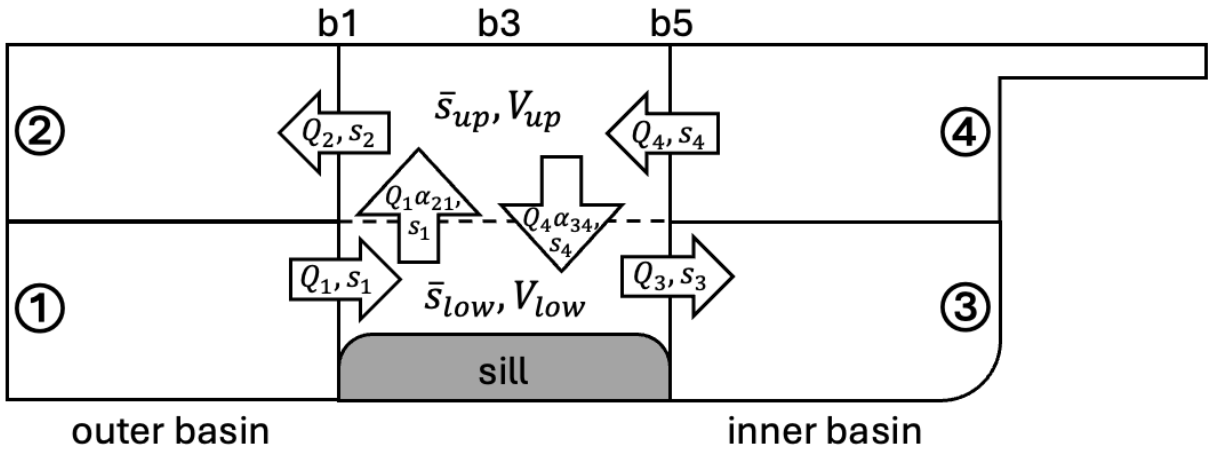

Figure 4.6: Diagram of the two-layer sill box model used to calculate the time-dependent efflux-reflux coefficients.

attempts to partition the volume and salt residuals evenly between the inputs and outputs to the sill region unless a different partitioning is required to satisfy Equation 4.18.

Time-dependent efflux-reflux coefficients

By relaxing some of the assumptions in the efflux-reflux framework, we develop a time-dependent version of the efflux-reflux coefficients. This allows us to determine how reflux at the sill varies over the spring-neap cycle. We modify the original box model shown in Figure 4.5 to partition the sill region into an upper and lower layer, with the reflux coefficients α_{21} and α_{34} determining the transports between the two boxes. A diagram of the two-layer box model is shown in Figure 4.6. We still assume that volume is conserved in each of the two boxes and in the sill region as a whole; therefore the efflux and reflux coefficients must still sum to 1. However, we allow the salt content of each of the two layers to vary over time.

We can solve for the α coefficients using the volume and salt budgets for either the upper or lower box. For the upper box, the volume budget (assuming no changes in volume) is:

$$Q_4 - Q_4\alpha_{34} + Q_1\alpha_{21} - Q_2 = 0 \tag{4.19}$$

Substitute $\alpha_{24} = 1 - \alpha_{34}$:

$$Q_4\alpha_{24} + Q_1\alpha_{21} - Q_2 = 0 \tag{4.20}$$

For the upper layer salt budget, we have:

$$Q_4 s_4 - Q_4 \alpha_{34} s_4 + Q_1 \alpha_{21} s_1 - Q_2 s_2 = \frac{d}{dt} \int_{V_{up}} s dV \tag{4.21}$$

where V_{up} is the volume of the upper layer and the right-hand side represents salt storage in the upper layer. Again substituting $\alpha_{24} = 1 - \alpha_{34}$:

$$Q_4 \alpha_{24} s_4 + Q_1 \alpha_{21} s_1 - Q_2 s_2 = \frac{d}{dt} \int_{V_{up}} s dV \tag{4.22}$$

We can now combine Equations 4.20 and 4.22 to solve for α_{21} and α_{24}. Multiplying Equation 4.20 by s_4 and subtracting from Equation 4.22 leads to:

$$Q_1 (s_1 - s_4) \alpha_{21} - Q_2 (s_2 - s_4) = \frac{d}{dt} \int_{V_{up}} s dV \tag{4.23}$$

$$\alpha_{21} = \frac{Q_2}{Q_1} \frac{s_2 - s_4}{s_1 - s_4} + \frac{1}{Q_1 (s_1 - s_4)} \frac{d}{dt} \int_{V_{up}} s dV \tag{4.24}$$

Notice that the first term on the right-hand side is the same as the expression for α_{21} given in Equation 4.16. To find α_{24}, multiply Equation 4.20 by s_1 and subtract from Equation 4.22:

$$Q_4 (s_4 - s_1) \alpha_{24} - Q_2 (s_2 - s_1) = \frac{d}{dt} \int_{V_{up}} s dV \tag{4.25}$$

$$\alpha_{24} = \frac{Q_2}{Q_4} \frac{s_1 - s_2}{s_1 - s_4} - \frac{1}{Q_4 (s_1 - s_4)} \frac{d}{dt} \int_{V_{up}} s dV \tag{4.26}$$

The other two coefficients can be found from $\alpha_{31} = 1 - \alpha_{21}$ and $\alpha_{34} = 1 - \alpha_{24}$. Alternatively, a similar derivation can be performed using the volume and salt budgets for the lower layer box, which give α_{31} and α_{34} directly:

$$\alpha_{31} = \frac{Q_3}{Q_4} \frac{s_3 - s_4}{s_1 - s_4} + \frac{1}{Q_4 (s_1 - s_4)} \frac{d}{dt} \int_{V_{low}} s dV \tag{4.27}$$

where V_{low} is the volume of the lower layer.

$$\alpha_{34} = \frac{Q_3}{Q_4}\frac{s_1 - s_3}{s_1 - s_4} - \frac{1}{Q_4(s_1 - s_4)}\frac{d}{dt}\int_{V_{low}} sdV \tag{4.28}$$

We calculate the time-dependent efflux-reflux coefficients from both the upper and lower layer budgets, using the same TEF variables shown in Equation 4.17. However, we do not perform any averaging or adjustments for perfect volume and salt conservation, and the inequalities in Equation 4.18 are not necessarily satisfied at every time step. To compute the storage terms, we assume that the volumes of the upper and lower boxes are constant and each equal to half the volume of the sill region (with zero sea surface height) V_{sill}. We approximate the mean salinity of the upper and lower boxes with the TEF salinities at section b3 (the midpoint of the sill), such that $\bar{s}_{up} = s^{b3}_{out}$ and $\bar{s}_{low} = s^{b3}_{in}$. This simplifies the storage terms to:

$$\frac{1}{Q_1(s_1 - s_4)}\frac{d}{dt}\int_{V_{up}} sdV = \frac{1}{Q_1(s_1 - s_4)}\frac{V_{sill}}{2}\frac{d}{dt}\left(\bar{s}_{up}\right) \tag{4.29}$$

$$\frac{1}{Q_4(s_1 - s_4)}\frac{d}{dt}\int_{V_{low}} sdV = \frac{1}{Q_4(s_1 - s_4)}\frac{V_{sill}}{2}\frac{d}{dt}\left(\bar{s}_{low}\right) \tag{4.30}$$

Because the time series of the TEF salinities sometimes have discontinuities or large spikes we use a median filter to remove outliers in the salinity data. Any points that have a difference of more that 0.5 psu from the median of the salinities in a nine-hour window around the data point are set to this median value. We also smooth all the TEF variables with a Savitzky-Golay filter (third order, 71 hour window length), and use the Savitzky-Golay filter to perform the salinity dervatives $d/dt(s^{b3}_{out})$ and $d/dt(s^{b3}_{in})$ directly. These smoothed time series of TEF variables and salinity derivatives are used to estimate the time-dependent efflux-reflux coefficients over seven spring-neap cycles.

4.2.3 Lagrangian analysis

Particle tracking experiments

In conjunction with the box model approach, we employ a Lagrangian analysis strategy utilizing simulated particle tracking experiments. The particle tracks provide additional information about the spatial and temporal distribution of residence times. Unlike other types of simulated tracer experiments such as model dye

releases, particle tracking has the advantage of providing the entire history of a particle's trajectory over time.

For each model run, we initialize the estuary with evenly spaced particles. The particles are positioned at the centers of each horizontal cell (which are uniformly sized in the estuary with a resolution of $320\ \mathrm{m}$), with eight vertical layers stacked $25\mathrm{m}$ apart (see Figure 4.8), giving a total number of particles released ranging from 35277 in the $5\ \mathrm{km}$ sill model to 38509 in the $80\ \mathrm{km}$ sill model. We use the Tracker 2 particle-tracking software package outlined in Xiong and MacCready [2024], with additional improvements as described in Brasseale and MacCready [2025]. Tracker 2 is an offline particle-tracking package which uses the hourly ROMS model output files to calculate particle trajectories. The particle tracking algorithm allows three-dimensional motion for the particles, using a fourth-order Runge-Kutta integration scheme based on nearest-neighbour velocities, along with diffusion and additional vertical random walk to account for turbulent motion [Xiong and MacCready, 2024; Brasseale and MacCready, 2025]. We track the particles for 120 days with an integration time step of 5 minutes, and the particle locations and properties are saved every hour. We can then sort the particle tracks based on properties such as their initial location, depth, current basin, or salinity.

Figure 4.7 shows a map view of example particle tracks for the 120 day experiment in the $20\ \mathrm{km}$ sill model. Note that only 250 sample tracks out of approximately total 36 000 tracks are shown. The Coriolis effect is evident, with most particles advected northwards along the coast when they exit the estuary. The particles traveling along the northern boundary of the model domain are likely due to the model's open boundary conditions (radiation with nudging) and not realistic. However, this should not affect our results inside and near the estuary. Figure 4.8 shows the starting and ending locations of particles released along the centerline of the estuary (45°latitude) in the inner and outer basin (particles released on the sill are not shown). Only a subset of track lines are shown. Few particles released in the outer basin remain there after 120 days, and those that end up in the inner basin are distributed at all depths. In contrast, the inner basin retains more of its original released particles, and those that are found in the outer basin after 120 days are mostly in the upper half of the water column. Many particles exit to the ocean, primarily on the slope outside of the canyon.

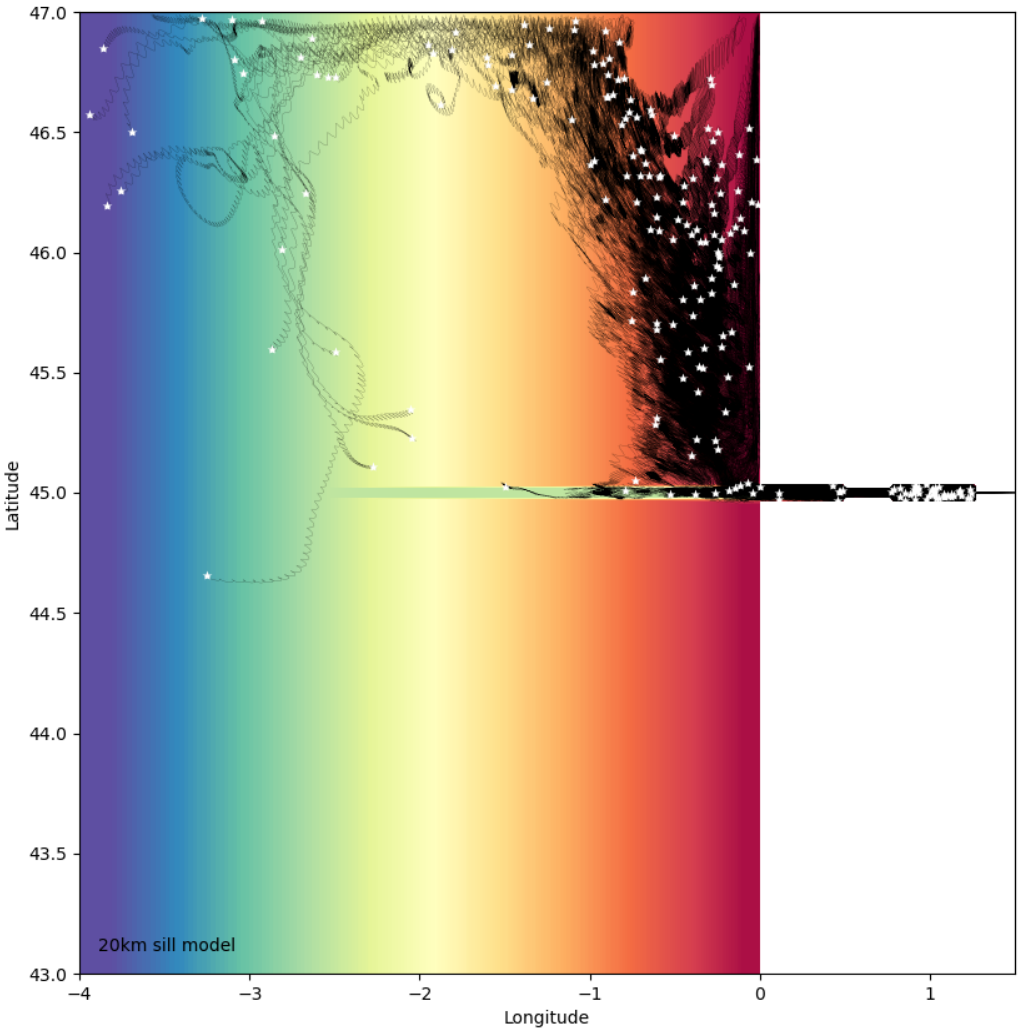

Figure 4.7: Examples of particle tracks from the 120 day particle tracking experiment in the 20 km sill model. Background colormap shows bathymetry with the same color scale as Figure 4.1. 250 sample tracks (out of 35988 total tracks) are shown as the black lines, with white stars showing the end points of the particles after 120 days. All particle tracks start in the estuary.

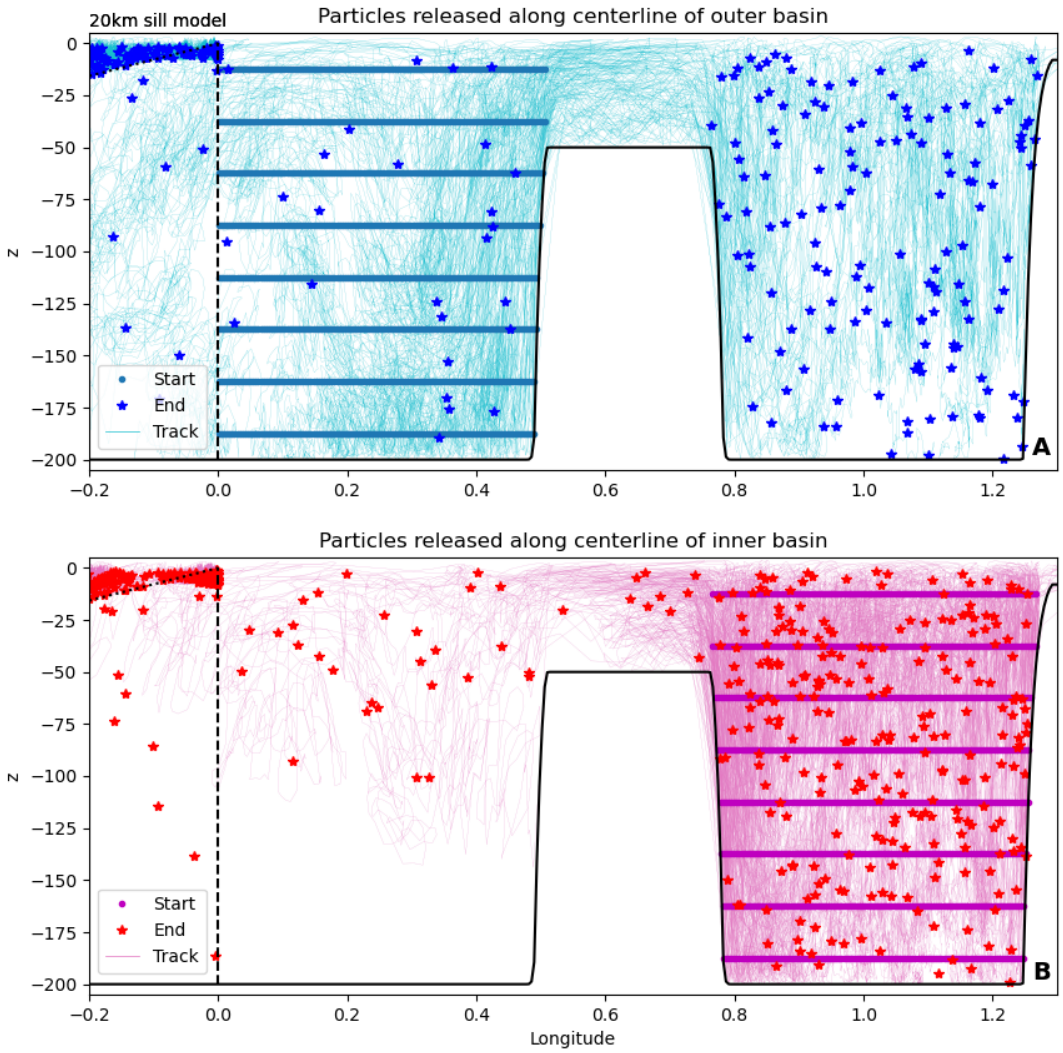

Figure 4.8: Section view of particles released along the centerline (45° latitude) of (A) the outer basin and (B) the inner basin in the 20 km sill model. The particles are tracked for 120 days. An example subset of approximately 25 sample tracks (out of approximately 1000 total tracks originating along the centerline in each basin) are shown as lines in each panel. The start (dots) and end points (stars) are not subsampled. Vertical dashed lines show the location of the coastline and dotted lines show the slope of the continental shelf, outside of the canyon extending from the estuary.

e-folding times

For a bulk measure of water retention, we can analyze the number of particles initialized in a particular region (e.g. inner or outer basin, or whole estuary) that remain in that volume over time. Assuming that the number of particles remaining will exponentially decrease over time, we can calculate the e-folding time T_e for the volume, which is the timescale over which the number of particles remaining N will be reduced by a factor of $1/e$:

$$N(t) = N_0 e^{-t/T_e} \tag{4.31}$$

where N_0 is the initial number of particles at $t = 0$. We categorize the particles based on their starting region and tally the number remaining over time. The total count of particles includes those that have exited and subsequently reentered the region. We also create a time series of the particle count excluding particles after they have left the domain for the first time. These time series are tidally averaged using a Godin filter. The particle counts at the beginning and end of the particle tracking runs can provide a quick estimate of the e-folding time:

$$T_e = \frac{120d}{ln\left(N(t = 120d)/N(t = 0)\right)} \tag{4.32}$$

Alternatively, we can fit an exponential curve to the particle time series and use the curve fitting parameters to determine the e-folding time and its uncertainty. We use Equation 4.31 as a two-parameter model for the data, where N is the number of particles and N_0 and T_e are the parameters to fit. We use nonlinear least-squares curve fitting with the tidally averaged particle count data (using the curve_fit function in SciPy). To improve the performance of the curve fitting algorithm and matrix conditioning, we scale the particle counts and time coordinate so that they vary between 0 and 1:

$$t_* = \frac{t}{120d} \tag{4.33}$$

$$N_* = \frac{N}{N(t = 0)} \tag{4.34}$$

Then we fit a curve of the form:

$$N_* = Ae^{-t_*/b} \tag{4.35}$$

with initial parameter guesses of 1 for both A and b. The e-folding time in days can be found from the fit value of b:

$$T_e = b \cdot 120d \tag{4.36}$$

We calculate the e-folding times for the whole estuary and inner basin, with and without including reentering particles.

Residence times and exposure times

Taking full advantage of the the spatial and temporal information contained in the particle tracks, we can calculate the residence time, a local measure that varies with the release location of the particles. Although the residence time may also vary over time, we cannot resolve this with a single particle tracking release. We compute the residence times for the inner basin and the entire estuary using section b5 or a1 as the volume boundary, respectively. The particle track longitudes are used to find the strict residence time and exposure time. The strict residence time is defined as the first moment a particle crosses the boundary section's longitude, whereas the exposure time describes the total duration that the particle spends within the volume during the particle tracking experiment. Therefore, the exposure time includes the effect of reentering particles. Note that due to the finite time of the particle tracking experiment, we are not able to resolve residence times longer than 120 days, which may influence our results, particularly where residence times are averaged together.

To see the spatial variability in the residence and exposure times, we use the initial particle release locations, which are evenly distributed on a grid in eight vertical layers, to make maps of the time scales at different depths in the estuary. We also used bin averaging to examine how the strict residence time varies with initial x-position, salinity, and depth of the particles. Finally, we can find the average strict residence time and exposure times for the whole estuary and inner basin to create a single-valued time scale that can be compared with the e-folding times and flushing times.

Efflux-reflux from particle tracking

The particle tracks can also be used to quantify the amount of reflux that occurs in the sill region. Because the efflux-reflux framework considers the tidally-averaged flows in the sill region, we tidally average the particle tracks (specifically the particles' longitude data) with the Godin filter. To estimate the efflux and reflux coefficients α (see Figure 4.5) we consider individual "visits" to the sill. A particle's tidally-averaged longitude data is used to create a time series representing which region it is located in over time: outer basin/ocean, sill region, or inner basin. The boundaries between the regions are defined as section b1 (between the outer basin and sill) and section b5 (between the inner basin and sill) as shown in Figure 4.2. Consecutive times when a particle is located in the sill region are considered as a single visit to the sill. For each visit, we record the basins in which the particle was located at the times immediately preceding and following the visit. We also count instances where particles are recorded going directly from the inner basin to the outer basin (or vice versa). These represent visits to the sill lasting less than one hour, such that the particle's location is not recorded on the sill in the hourly particle track data. For visits originating in the inner basin, we consider the fraction that do not continue to the outer basin as an estimate of the downwards reflux coefficient (α_{34}). Similarly, the fraction of particles entering the sill region from the outer basin that do not continue to the inner basin is used as an estimate of the upwards reflux coefficient (α_{21}). Note that the interval at which the particle track data is saved will influence the results, as the number of reflux visits lasting less than one hour cannot be measured. We also do not include visits when a particle is located on the sill at the beginning or end of the particle tracking experiment, as we cannot determine the starting or ending basin. This particle-based approach to evaluating efflux-reflux complements the traditional box model efflux-reflux calculation presented in Section 4.2.2 and allows the importance of reflux to be estimated without any salinity information.

Particle visits to the sill

Using a similar approach to the particle-based efflux-reflux calculation above, we characterize the experience of particles during their time on the sill in the five models. However, in this case, we use the unfiltered particle tracks instead of the tidally-averaged tracks. For each visit to the sill, we use the starting and ending basins to classify the particles as "returning" if they return from the sill region to the same basin they

originated from, or “transiting" if they exit the sill region to the opposite basin. We calculate the duration that particles spend on the sill based on the number of hours that the particle is recorded in the sill region in the hourly track data. For particles that transit the sill in less than one hour, with no position recorded on the sill, the duration of the visit is assigned as zero hours (this only occurs in the $5\ \mathrm{km}$ sill model). Note that the hourly resolution of the saved track data limits which particles are captured in the returning category. Particles that spend less than one hour on the sill may not be recorded in the sill region and therefore would not be counted as having visited the sill at all. For the returning particles, we also calculate the maximum extent that the particle reaches along the sill during its visit. This distance is measured from the end of the sill that the particle enters from.

4.3 Results and discussion

4.3.1 Model velocity and salinity

Contours of tidally-averaged salinity on an along-estuary section are shown in Figures 4.9 and 4.10 for neap and spring, respectively. The outer basins have a similar stratification in all of the models, which is comparable to the ocean salinity boundary forcing, whereas the salinity of the inner basin varies greatly between models. The short $5\ \mathrm{km}$ sill model has a very salty inner basin, with maximum salinities reaching $31.5\ \mathrm{psu}$. Compared to the $5\ \mathrm{km}$ sill model, the inner basin is approximately $1\ \mathrm{psu}$ fresher in the $20\ \mathrm{km}$ sill model, and approximately $3\ \mathrm{psu}$ fresher in the $80\ \mathrm{km}$ sill model. This indicates that the freshwater flushing times must be longer in the models with longer sills.

Across the sill, the $5\ \mathrm{km}$ sill model has isohalines that are relatively flat. In the $20\ \mathrm{km}$ sill model the isohalines begin to slope more across the sill and are steeper on the spring tide. In the $80\ \mathrm{km}$ sill model, the isohalines slope strongly across the sill at neap tide, and are near vertical near the midpoint of the sill on the spring tide indicating well-mixed conditions. This portion of the estuary on the long sill resembles a partially mixed estuary. Looking across the three models, we can see that the salinity structure is fairly similar in the regions where the sills overlap, but a longer sill is required for partially mixed conditions to develop away from the edges.

Figures 4.11 and 4.12 show sections of the tidally-averaged along-channel velocity. At neap tide, there

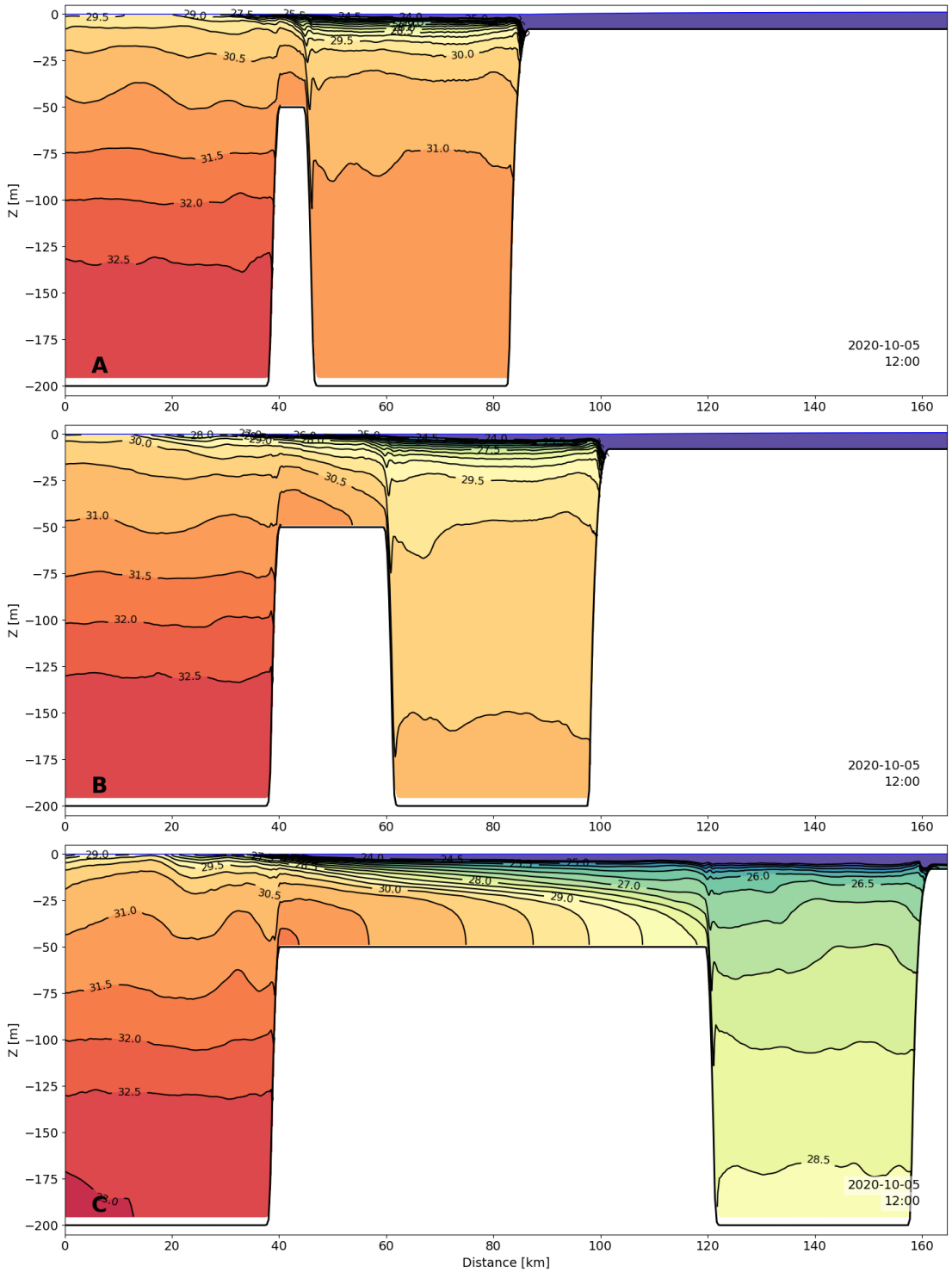

Figure 4.9: Along-estuary sections of tidally-averaged salinity at neap tide for the (A) 5 km, (B) 20 km, and (C) 80 km sill models. All panels have the same color scale. Contours are at 0.5 psu intervals, and the lowest contour is at 24 psu.

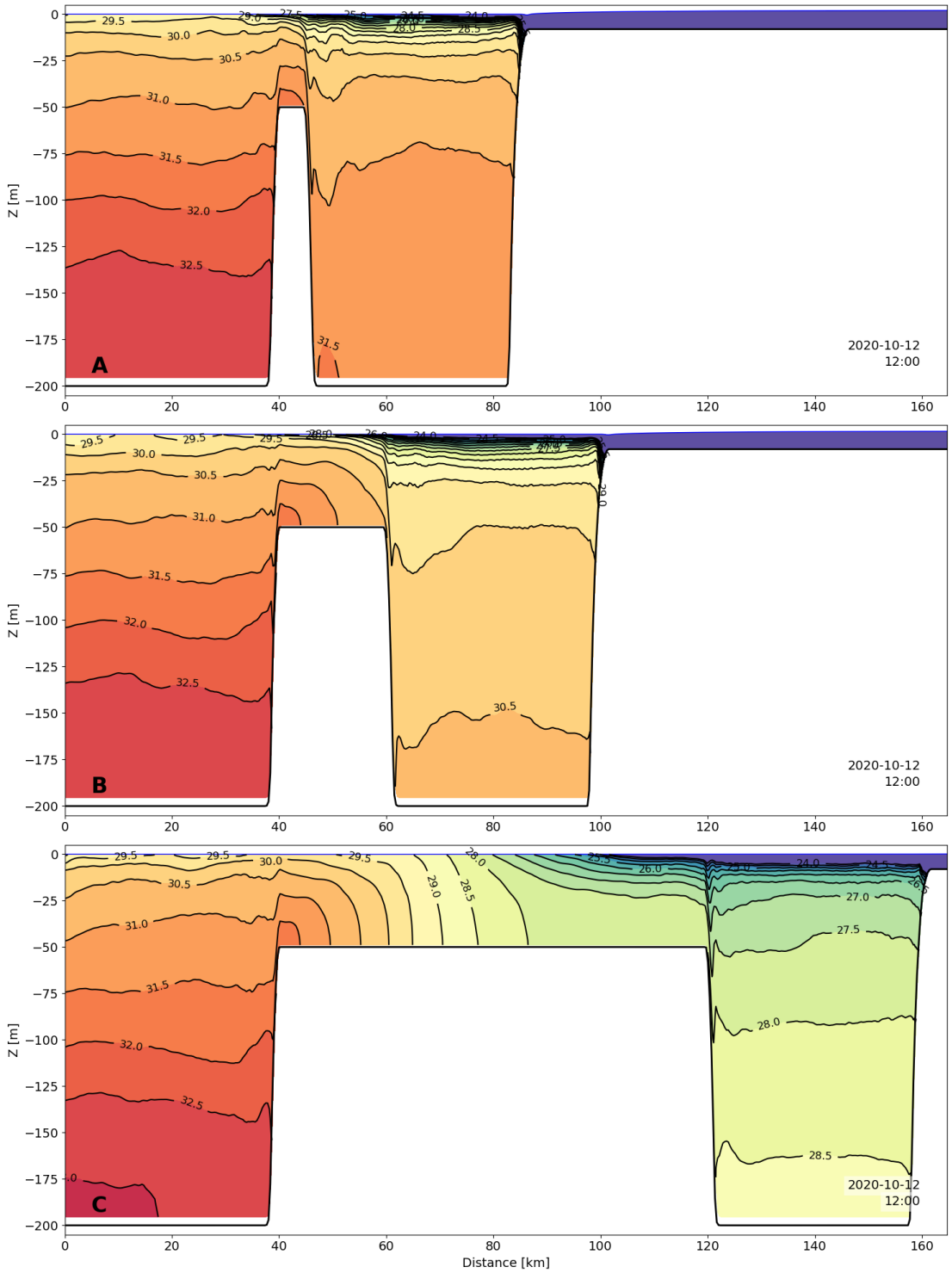

Figure 4.10: Along-estuary sections of tidally-averaged salinity at spring tide for the (A) 5 km, (B) 20 km, and (C) 80 km sill models. All panels have the same color scale. Contours are at 0.5 psu intervals, and the lowest contour is at 24 psu.

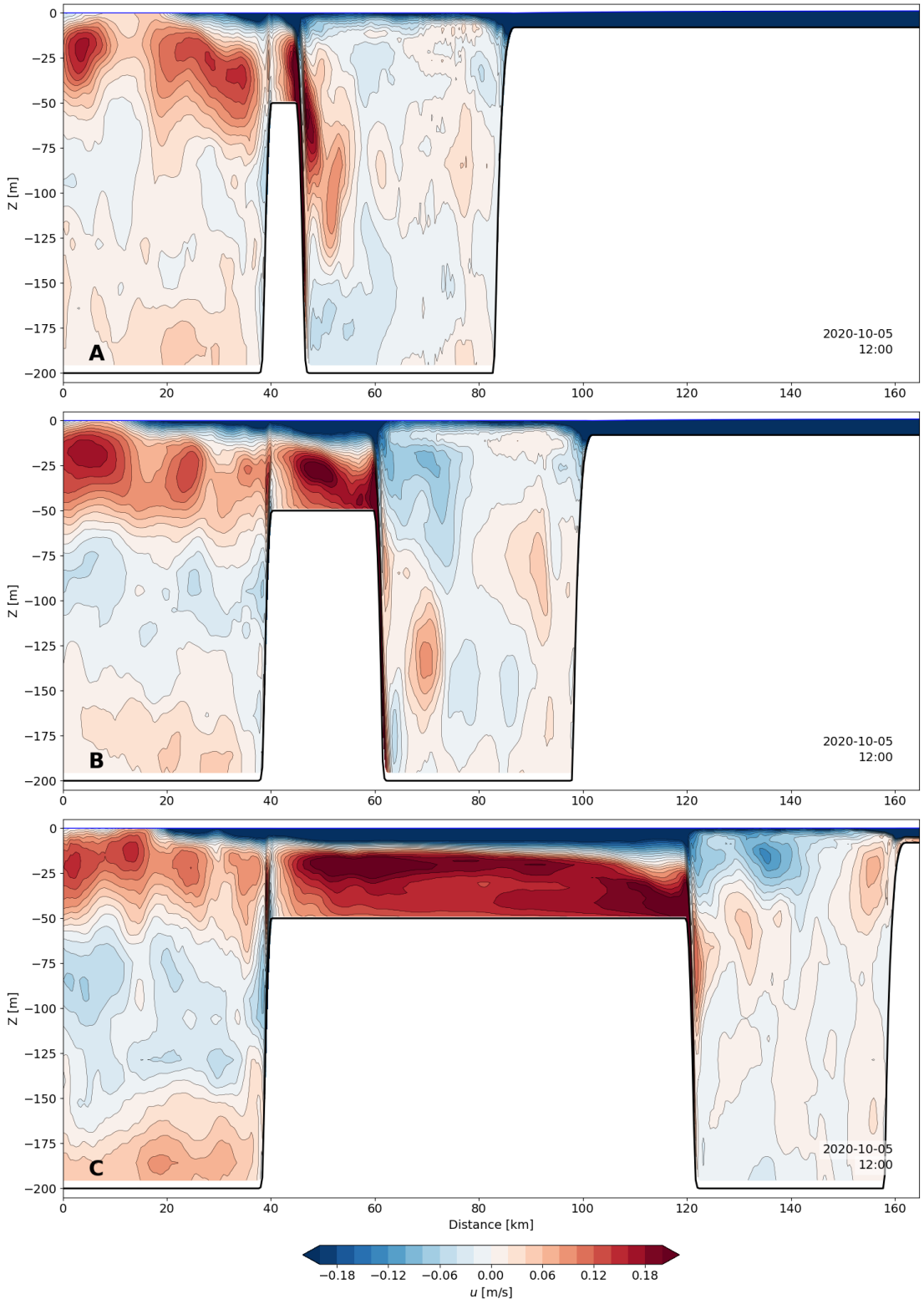

Figure 4.11: Along-estuary sections of tidally-averaged along-channel velocity at neap tide for the (A) 5 km, (B) 20 km, and (C) 80 km sill models.

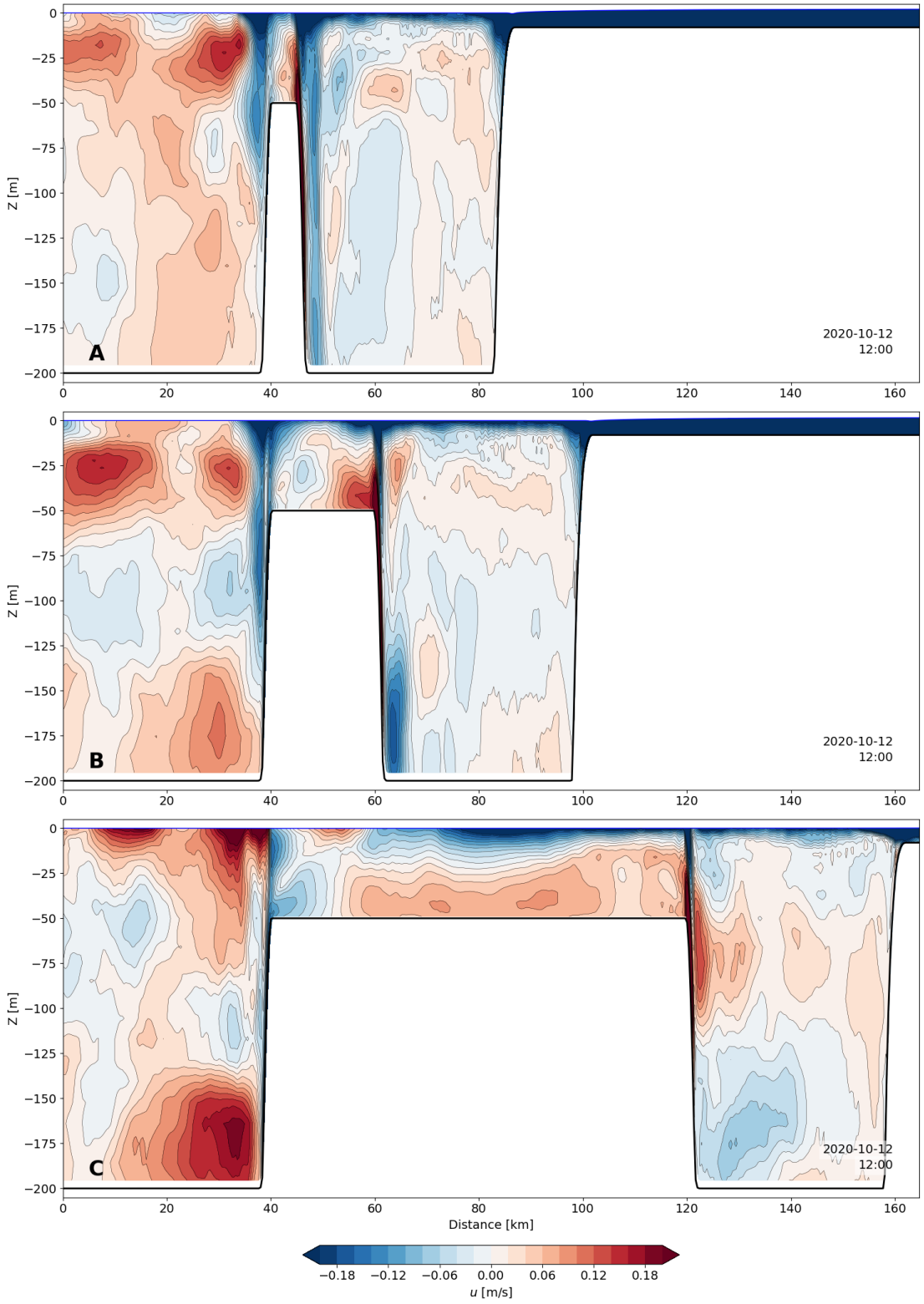

Figure 4.12: Along-estuary sections of tidally-averaged along-channel velocity at spring tide for the (A) 5 km, (B) 20 km, and (C) 80 km sill models.

is a strong two-layer exchange flow, especially in the longer sill models. Velocities on the sill are weaker during the spring tide, and the two-layer exchange is less defined. At both spring and neap there are sharp fronts at the ends of the sills. There is also lateral structure is the flow field which is not shown. The width of the estuary (8 km in the basins and 4 km at the sills) means that Coriolis effects are also significant. Additionally, the vertical velocities, while small, play an important role particularly at the edges of the sills.

4.3.2 Transport time scales

Flushing times

Figure 4.13 show the volume, freshwater, and saltwater flushing times for the whole estuary and the inner basin for different sill lengths. For the inner basin, the average exchange flow at the landward end of the sill is slightly weaker in the long sill models, which leads to increased flushing times. The freshwater flushing times, which increase for longer sills, are consistent with the fresher inner basin shown in Figures 4.9 and 4.10. The freshwater is flushed more quickly than the inner basin as a whole, which would be expected if most of the river water joins the outflowing layer of the exchange flow. In the estuary as a whole, there is no clear trend in the volume flushing times, and the saltwater flushing time closely follows the volume flushing time because the salinity of the estuary is high. However, the freshwater flushing time increases significantly as the sill length grows, because the fresher inner basin decreases the mean salinity of the estuary. We use the outflow Q_{out} as the characteristic flow rate flushing the estuary, but other choices are possible. For example, the freshwater filling time would instead use the river flow Q_r. However, in our system, and many realistic estuaries, the exchange flow is much larger than the river flow, so we expect that the freshwater filling time would not be representative of retention in the estuary. Time-varying flushing times could also be calculated using the time series of volume and Q_{out}. In our case, the average values are more informative because the flushing times are longer than the spring-neap cycle.

e-folding times

Figure 4.14 shows the number of particles remaining in the inner and outer basins over time for the five different sill lengths. The dotted lines show the exponential curve fits to the tidally-averaged particle counts, which are used to find the e-folding times. For the outer basin, the time series are very similar regardless

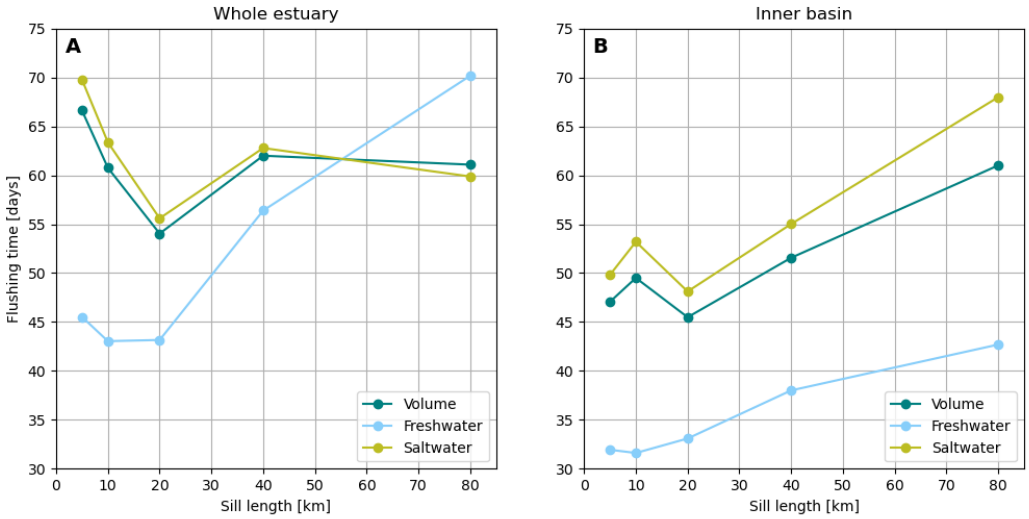

Figure 4.13: Volume, freshwater, and saltwater flushing times for (A) the whole estuary and (B) the inner basin as a function of sill length.

of sill length. Interestingly, the intermediate length $20\ \mathrm{km}$ sill model has the fastest e-folding time for the outer basin. For the inner basin, the sill length has a much larger influence on the retention of particles in the basin. Longer sills have greater e-folding times, with the exception of the $5\ \mathrm{km}$ and$10\ \mathrm{km}$ models which exhibit very similar behavior. In the left panel of Figure 4.14, we can see oscillations in the particle curves due to the spring-neap cycle. However, the timing is not the same in all models. The $40\ \mathrm{km}$ and $80\ \mathrm{km}$ sill models have steeper slopes at neap tide while the $5\ \mathrm{km}$ and$10\ \mathrm{km}$ sill models have steeper slopes at spring tide. The intermediate $20\ \mathrm{km}$ sill model shows much less spring-neap variability. This is consistent with the results of Chapter 3, where we found that the salt transport at the sill transitions from increasing at spring tide to decreasing at spring tide when the sill length exceeds the tidal excursion ($20\ \mathrm{km}$).

Figure 4.15 shows the particle counts for the two basins grouped by their initial release depth, above or below sill height. The e-folding times are not strongly influenced by their starting location within the basin. The two curves for each model represent the particles that remain in their starting basin or more restrictively, within their starting depth bin within the basin. In the inner basin, there is a wide separation between these curves, indicating that many of the retained particles are displaced from their original depth and the basin is relatively homogenized.

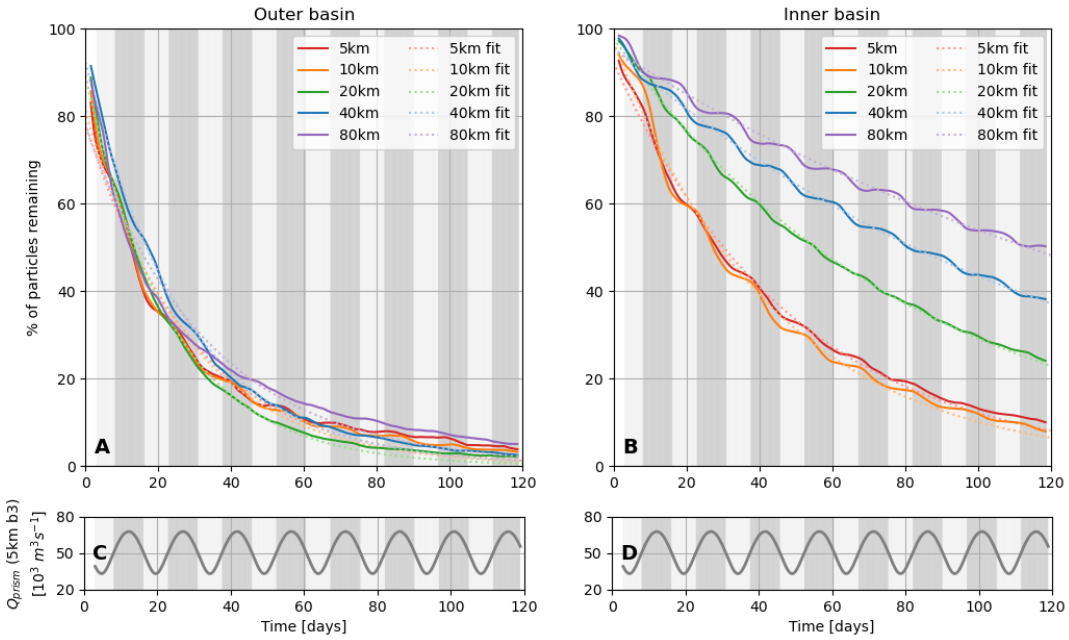

Figure 4.14: Percentage of particles released in the (A) outer and (B) inner basins remaining in those basins over time. Particles that have exited the basin and reentered are included in the total. The curves have been tidally averaged using the Godin filter. The dotted lines are an exponential fit to the tidally-averaged curves. The fitting parameters are used to calculate the e-folding time for each basin. Grey shading shows the timing of the spring-neap cycle (peaks of Q_{prism} in the 5 km sill model at section b3 as shown in panels C and D).

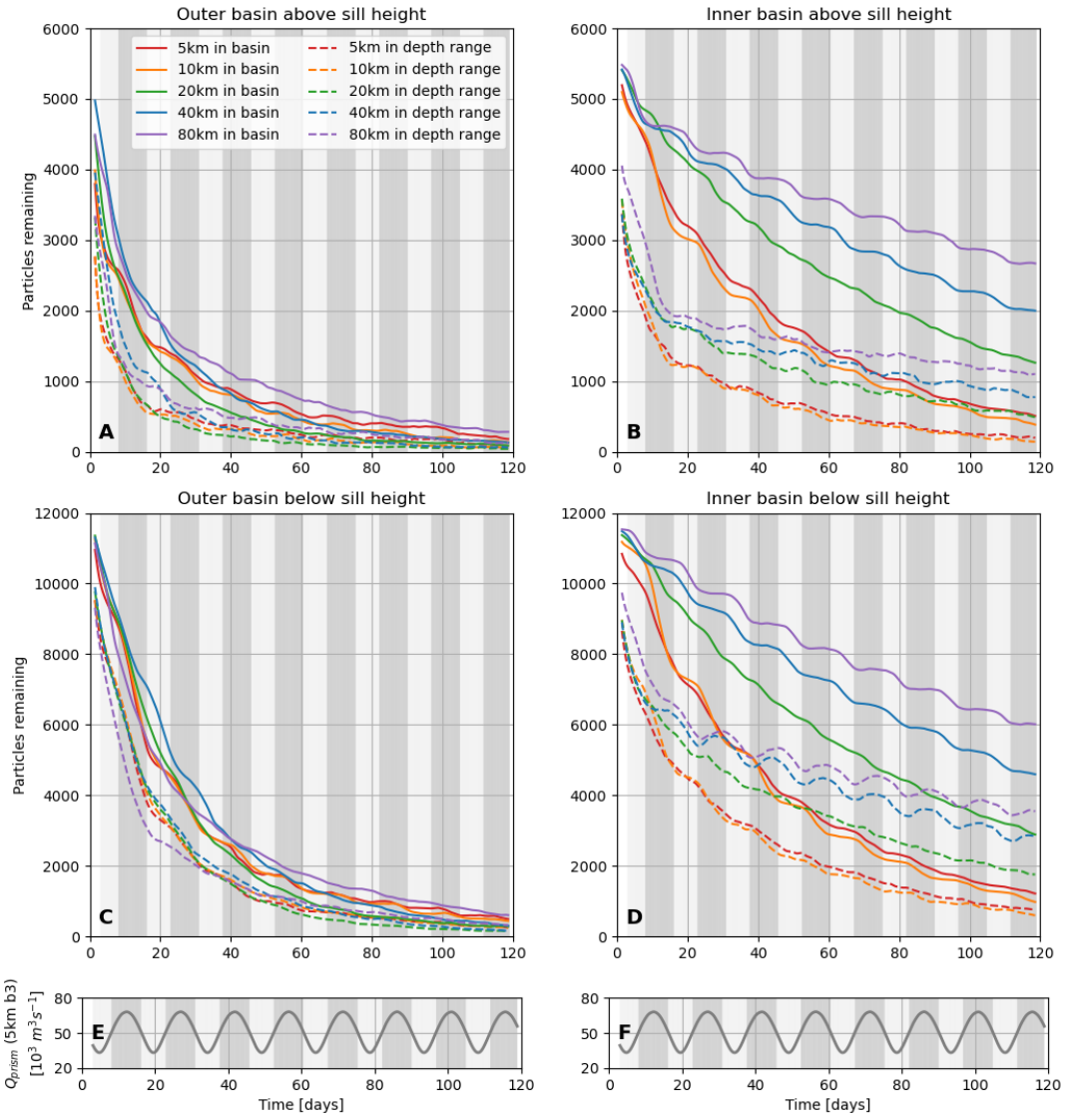

Figure 4.15: Particles released (A,B) above and (C,D) below sill height in the outer and inner basins. Solid lines show particles remaining in their original basin, while dotted lines show particles remaining in their initial depth range in the original basin. Particles that have exited the volume and reentered are included in the total. The curves have been tidally averaged using the Godin filter. Grey shading shows the timing of the spring-neap cycle (peaks of Q_{prism} in the 5 km sill model at section b3 as shown in panels E and F).

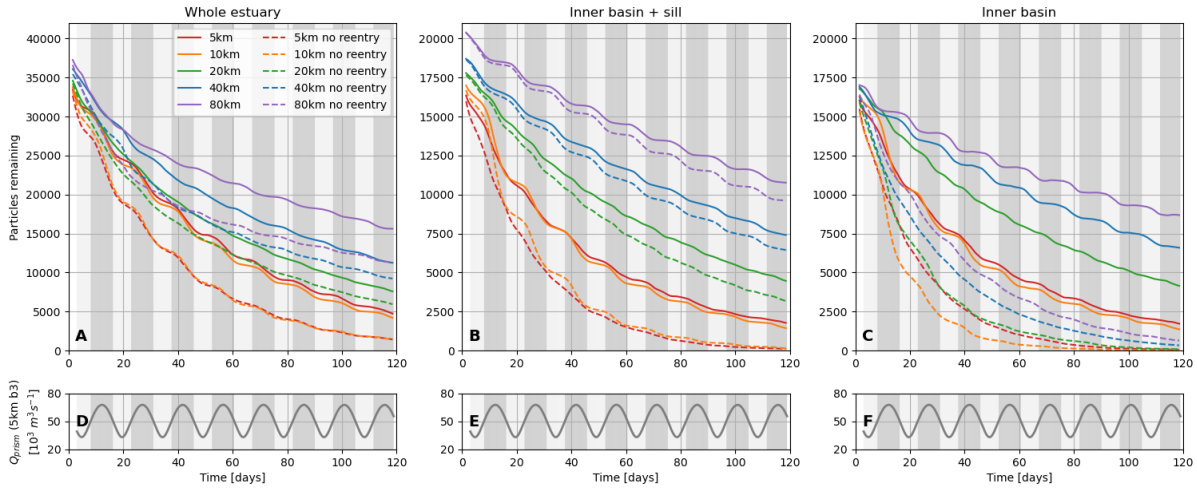

Figure 4.16: Particles released in three different subvolumes of the estuary: (A) the whole estuary, (B) the inner basin and sill, and (C) the inner basin, remaining over time. Solid lines show the total number of particles remaining in the subvolume, including particles that have exited and reentered, while dashed lines count only the particles that have never exited the subvolume. The curves have been tidally averaged using the Godin filter. Grey shading shows the timing of the spring-neap cycle (peaks of Q_{prism} in the 5 km sill model at section b3 as shown in panels D-F).

Figure 4.16 shows a comparison of the particle counts with and without reentering particles. For the inner basin, the particle counts are greatly reduced when reentering particles are excluded, and show much less spring-neap variation. By the end of the 120 day experiment, most of the difference in particle counts between the different models is due to particle reentry. At first glance, this may seem inconsistent with the results of MacCready et al. [2021], who found that incomplete homogenization was more important than reflux in determining residence times in the Salish Sea. However, we must emphasize the importance of the domain boundary. If we consider Panel B of Figure 4.16, which shows the particle counts for a subvolume combining the inner basin and sill, the particle counts with and without reentry are much more similar, especially for the longer sills. Additionally, because the geometry of our idealized models are substantially simpler than that of the Salish Sea and Puget Sound, it is likely that the inner basin is indeed more homogenized that these realistic estuaries. This is supported by the relative insensitivity of the e-folding time and strict residence time (see Section 4.3.2) to the particle release depth.

Residence times and exposure times

The residence time and exposure time are local measures of water retention, with every particle release point having a unique time scale. Figures 4.17 and 4.18 show maps of the strict residence time and exposure time for the $5\ \mathrm{km}$ and $80\ \mathrm{km}$ sill models at the top and bottom particle release layers. In the strict residence time for the whole estuary (panels A and E in both figures), we can see impact of the Coriolis effect where particles along the northern side of the estuary exit fastest. When we instead consider the exposure time, which is the total time that a particle spends in the domain during the experiment, incorporating the effect of particle reentry, this effect is no longer visible. The exposure time must always be greater than or equal to the strict residence time. For the short $5\ \mathrm{km}$ sill model, the exposure times and strict residence times are similar, which indicates that particle reentry is less important. Also, the transport time scales in the inner basin are similar whether considering the whole estuary domain or the inner basin domain. This indicates that particles exiting the inner basin proceed to promptly exit the estuary to the ocean. In contrast, for the long $80\ \mathrm{km}$ sill model, the strict residence times for the inner basin (panels B and F) are much shorter than the exposure times or the strict residence time calculated using the estuary mouth boundary. This indicates that most of the particles return to inner basin after their initial exit, and may visit the sill region several times before transiting to the outer basin and exiting the estuary.

Figures 4.19, 4.20, and 4.21 show the average strict residence times based on the initial release properties of the particles (longitude, salinity, and depth, respectively.) In Figure 4.19 we see that the residence times generally increase with increasing distance from the boundary. Because of the sloping sides of the estuary bathymetry, particles released at the ends of the basins are at shallower depths on average, which may account for the local decrease in residence times. Particles with fresher release salinities have shorter residence times in the inner basin, as shown in Panel B of Figure 4.20. This is consistent with the flushing time results where we found that the freshwater flushing times are shorter than the saltwater or volume flushing. Note that some points in these curves of binned averages (particularly at the ends) represent only a handful of particles, which is why there can be large fluctuations. For the estuary as a whole, the trends in residence times with release salinity are not clear, but in the middle of the salinity range for each model it appears that the residence times remain relatively constant. This may be caused by competition between two effects: fresher water is more likely to be included in the outflowing layer of the exchange flow, but is also likely to

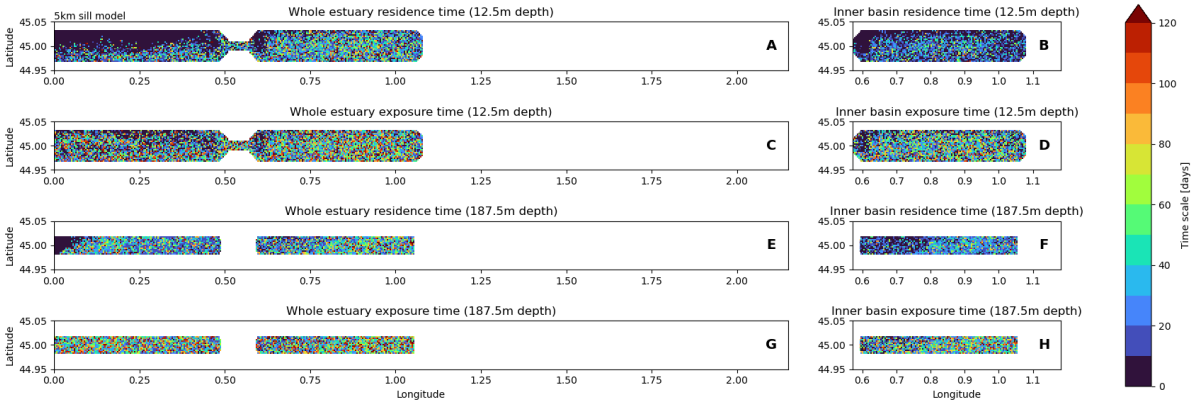

Figure 4.17: Maps of strict residence times and exposure times for the estuary and the inner basin in the 5 km sill model. Particles that never exit the domain during the particle tracking experiment have their strict residence time set to the length of the particle tracking run (120 days) plus one hour. Panels A-D show time scales for particles released in the layer closest to the surface (12.5 m depth), while panels E-H show time scales for particles released in the layer closest to the bottom (187.5 m depth).

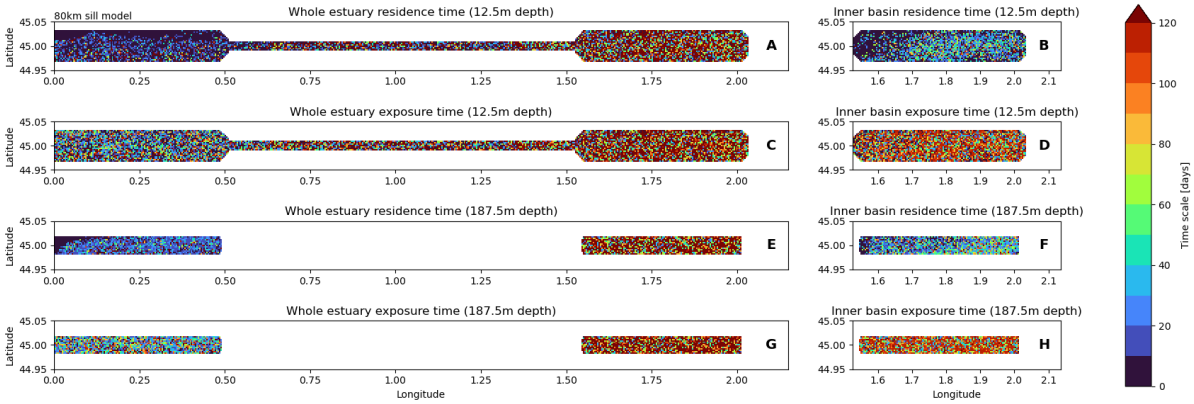

Figure 4.18: Maps of strict residence times and exposure times for the estuary and the inner basin in the 80 km sill model. Particles that never exit the domain during the particle tracking experiment have their strict residence time set to the length of the particle tracking run (120 days) plus one hour. Panels A-D show time scales for particles released in the layer closest to the surface (12.5 m depth), while panels E-H show time scales for particles released in the layer closest to the bottom (187.5 m depth).

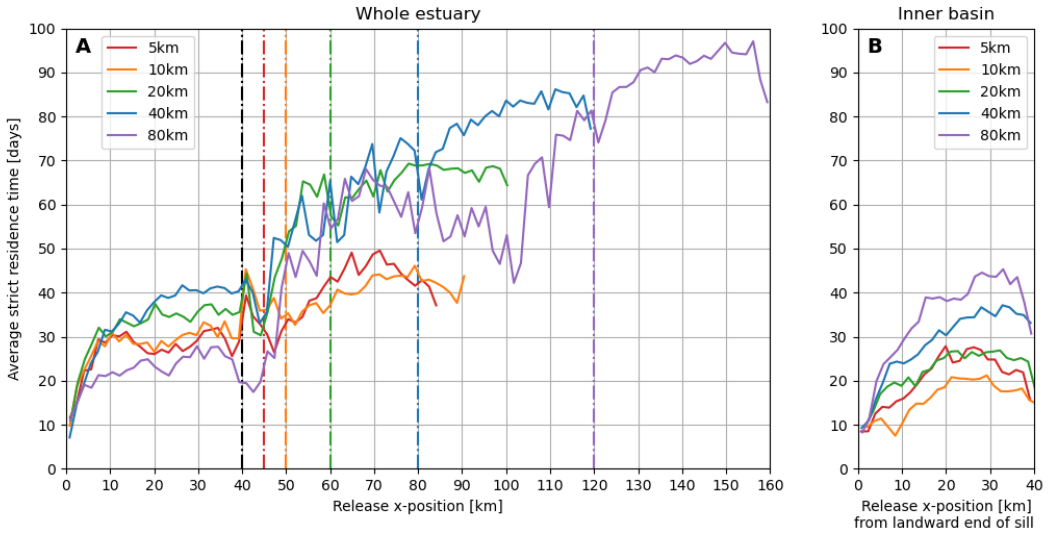

Figure 4.19: Average residence time based on x-position of particle release location for (A) the whole estuary and (B) the inner basin. The dash-dotted black line shows the location of seaward end of the sill in all models, while the dash-dotted colored lines show the location of the landward end of the sill for different sill lengths, using the same colors shown in the legend. The residence times used are the strict residence times, i.e. the time of first exit from the domain. Particles that never exit the domain during the particle tracking experiment have their strict residence time set to the length of the particle tracking run (120 days) plus one hour. Panel B has a modified x-axis showing the distance from the landward end of the sill, which means that the inner basins from all models cover the same x range.

originate further back in the estuary, away from the boundaries. Finally, in both the whole estuary and inner basin, deeper particle releases have longer residence times, but the effect is small. This is corroborated by the e-folding results for particles released above and below the depth of the sill (Figure 4.15), which show similar decay time scales regardless of release depth, and that a significant fraction of particles remaining in their original basin shift to a different depth level.

Note that both the strict residence time and exposure time are limited by the length of the particle tracking experiment. For particles that never leave the volume during the experiment, the strict residence time is set to one hour longer than the particle tracking run (120 days), although their true strict residence time may be longer.

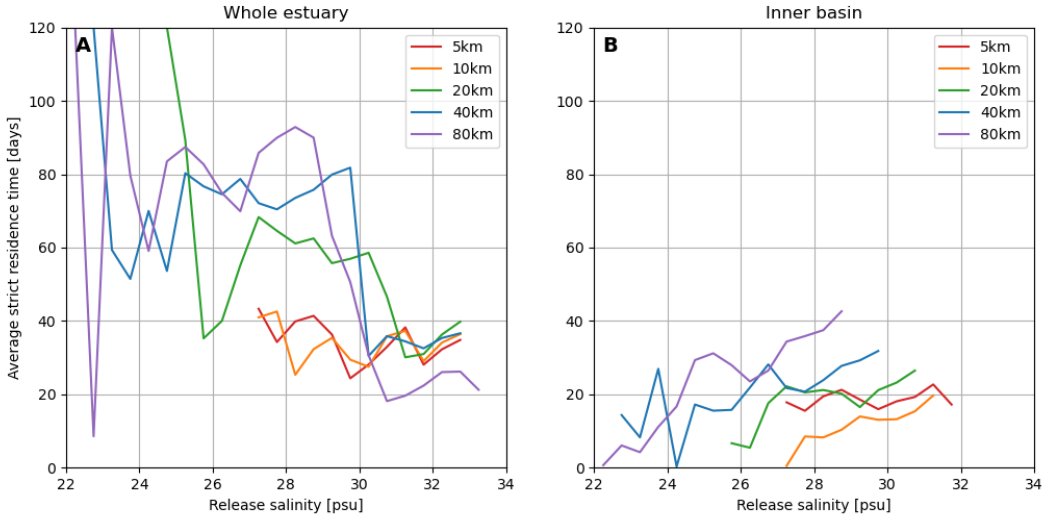

Figure 4.20: Average residence time based on initial salinity for (A) the whole estuary and (B) the inner basin. 0.5 psu bins are used for averaging. The residence times used are the strict residence times, i.e. the time of first exit from the domain. Particles that never exit the domain during the particle tracking experiment have their strict residence time set to the length of the particle tracking run (120 days) plus one hour.

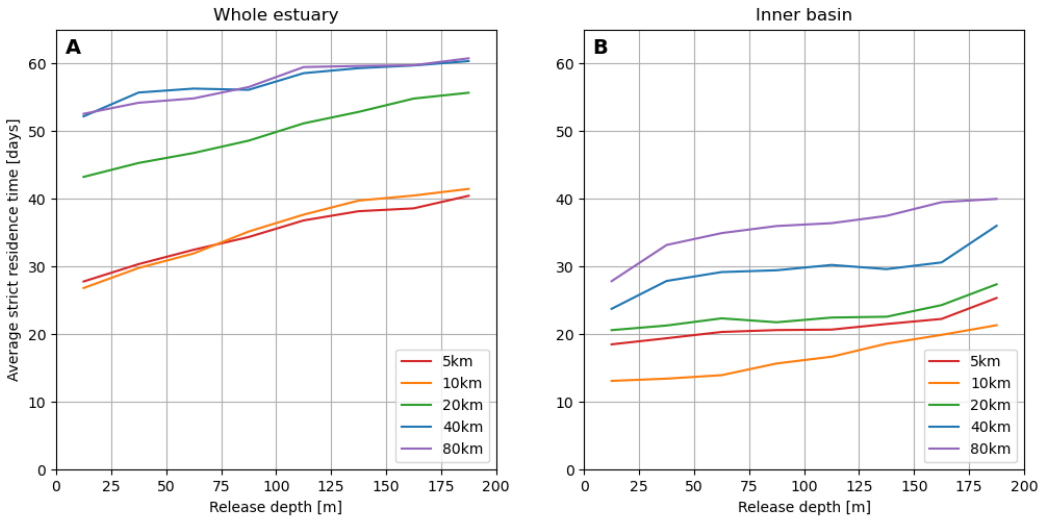

Figure 4.21: Average residence time based on initial depth for (A) the whole estuary and (B) the inner basin. $25\ \mathrm{m}$ bins are used for averaging, which groups the particles based on their initial release layer (see Figure 4.8). The residence times used are the strict residence times, i.e. the time of first exit from the domain. Particles that never exit the domain during the particle tracking experiment have their strict residence time set to the length of the particle tracking run (120 days) plus one hour.

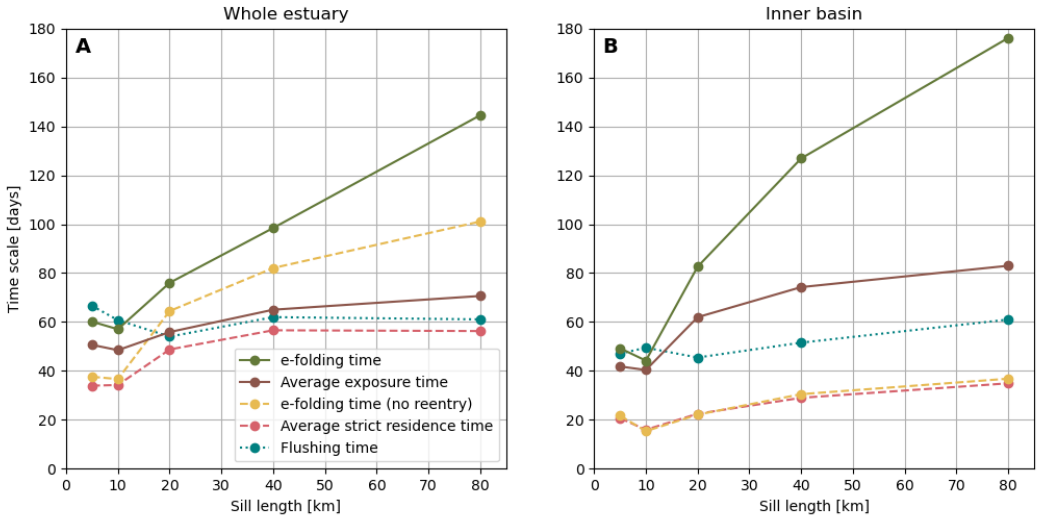

Figure 4.22: Transport time scales from particle tracking experiments for (A) the whole estuary and (B) the inner basin as a function of sill length. The e-folding time and exposure time (solid lines) include the effects of particle reentry to the domain, while the e-folding time without reentry and strict residence time (dashed lines) only consider the time of first exit. The exposure time and strict residence time are limited by the length of the particle tracking experiment (120 days). Particles that never exit the estuary during the particle tracking experiment have their strict residence time set to the length of the particle tracking run (120 days) plus one hour. The flushing time (dotted lines) is shown for reference (same as in Figure 4.13).

Importance of reentry for transport time scales

Figure 4.22 shows the five transport timescales (volume flushing time, e-folding time with and without reentry, average strict residence time, and average exposure time) for the whole estuary and inner basin as a function of sill length. All of the particle-based time scales increase with longer sill lengths. There are several possible causes which could account for differences in retention across varying sill lengths, including reentry and reflux, incomplete homogenization, or differences in exchange flow magnitude.

The e-folding times with and without reentry correspond to the particle count curves in Panels A and C of Figure 4.16, and are found from the fit parameters of exponential fits to those curves. The e-folding time without reentry must always be equal to or less than the e-folding time including reentering particles. The e-folding times with and without reentry become increasingly disparate as the sill lengthens, and this effect is amplified when considering the inner basin rather than the estuary as a whole. Therefore, extended e-folding times in the long sill models are primarily due to water returning to the domain after exiting. Similarly, the

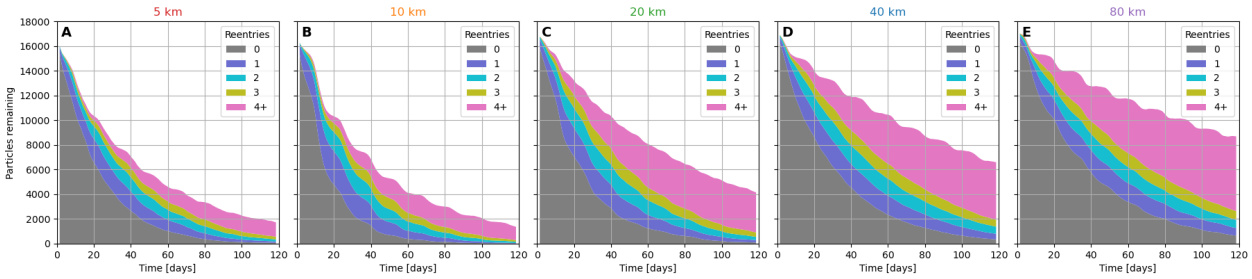

Figure 4.23: Particles initialized in the inner basin remaining over time, colored by the number of reentries from the sill region. Subplots show the different model ensemble members. The curves have been tidally averaged using the Godin filter.

difference between the average exposure time and average strict residence of the inner basin grows with increasing sill length. However, the difference is not as pronounced because the exposure times are limited by the length of the particle tracking experiment (120 days). For the inner basin, the average strict residence time and the e-folding time without reentry are nearly identical. This indicates that the inner basin could be modeled well as a continuously stirred tank reactor with exponential tracer decay, if the tracer of interest undergoes transformation or becomes otherwise irrelevant after its first exit from the basin. This is not true for the estuary as a whole, except in the short sill cases (5 km and10 km). For the inner basin, the flushing times fall between the particle-based time scales with and without reentry.

Figure 4.23 shows the particle counts in the five models for the inner basin, colored by the particles' number of reentries. We can see that the differences in particle retention between the different sill lengths is mostly attributable to particle reentry. As the sill lengthens, a growing number of particles have exited and reentered in inner basin multiple times (4+). However, there is also a slight difference between the grey areas which represent particles that have never left. This remaining difference may be due to the weaker exchange flow at the landward end of the sill, as well as incomplete homogenization or other unexplored factors.

Because reentry is such an important contributor to retention in our models, we conclude that the e-folding time is the most meaningful transport time scale for understanding how sill length affects water renewal in the estuary. Another advantage of the e-folding method is that we can estimate the time scale T_e

even when it is expected to be longer than the duration of the particle tracking experiment. The exposure time or the (non-strict) residence time, defined by Delhez et al. [2004] as the time of a particle's final exit from the domain, would become more representative if these time scales were calculated from longer particle tracking experiments.

4.3.3 Efflux-reflux

Figure 4.24 shows the reflux coefficients α_{21} and α_{34} calculated from the TEF box model and the particle tracking method. In all cases, the amount of reflux at the sill increases with increasing sill length. This supports the idea that particle reentry to the inner basin, which contributes significantly to the increased retention observed with longer sills, is not solely due to tidal "sloshing" back and forth across the sill boundaries, but is also caused by mixing and vertical advection in the sill region. The adjustments performed to satisfy the salinity conditions of Equation 4.18 and perfect volume and salt conservation across the sill do not result in significant changes to the resulting reflux coefficients. Because there is some upwards drift in the model salinity over the period used for analysis (see Figure 4.3), the adjusted reflux coefficients are slightly higher in the outer basin and lower in the inner basin. The exception is the $5\ \mathrm{km}$ sill model, where the unadjusted inner basin reflux coefficient α_{34} is slightly negative, because the inequality $s_3 \leq s_1$ is not met. This indicates that the efflux-reflux framework may not be appropriate for this shortest sill case.

The efflux-reflux coefficients estimated from the tidally-averaged particle tracks show similar trends to the box model calculations. However, the outer basin reflux is underestimated relative to the box model results, while the inner basin reflux is overestimated, especially for the shorter sills. It is important to note although the particles are evenly distributed throughout the estuary at the time of release, the sampling of particles visiting the sill may not be representative of the water entering the sill region. The number of particles visiting the sill will also vary over the course of the experiment, as more and more particles exit the estuary entirely to the ocean. Some particle visits included in the reflux may be very short, and the reflux fraction is sensitive to the temporal resolution of the particle track data. Also, we use only the longitude data from the particle tracks to categorize the visits as efflux or reflux. Therefore, we cannot determine whether the particles have actually been mixed or advected vertically into the opposing layer of the exchange flow. Incorporating depth and/or salinity information from the particle tracks may help to refine the particle-based

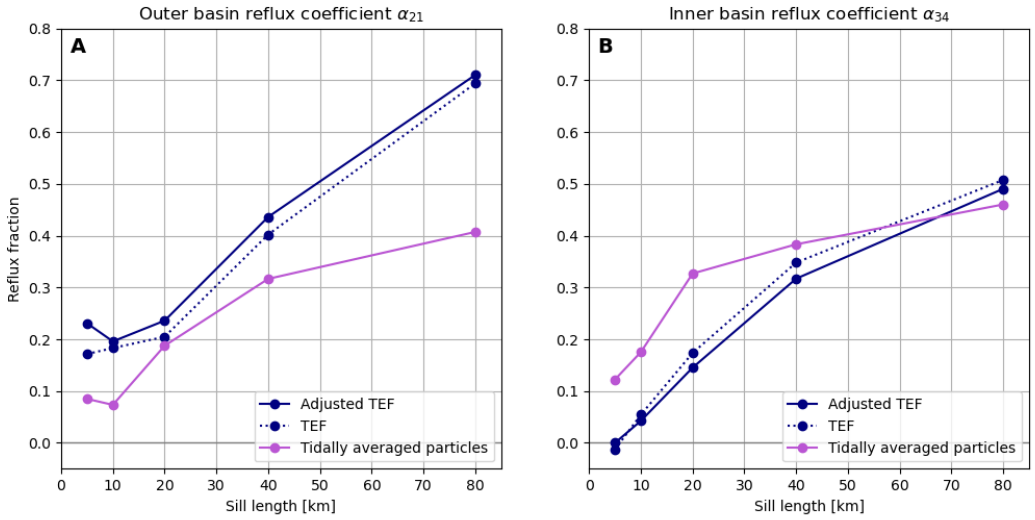

Figure 4.24: Efflux-reflux coefficients from the TEF box model and estimated from particle trajectories as a function of sill length. Refer to Figure 4.5 for a description of the four α coefficients. For the adjusted TEF and particle-based methods, the efflux and reflux coefficients from a basin sum to 1. For the particle-based calculations, all particle visits to the sill are included and sorted by their starting and ending basins.

reflux method. Different arrangements of particle releases tailored to the efflux-reflux question may also improve the results.

Figure 4.25 shows the time-dependent reflux coefficients, with background shading showing the timing of the spring-neap cycle. Reflux is enhanced on the spring tides across all sill lengths, which is expected because the tidal velocities on the sill are elevated which leads to increased mixing. However, the longer sills have much greater spring-neap variability in the amount of reflux. This is consistent with the results of Chapter 3, where we found that the long sill models exhibit greater spring-neap variability in the exchange flow salt transport $Q_{in}\Delta s$. The elevated reflux coefficients ($>= 1$) in the long sill models during spring tides also help explain the spring-neap modulation of the particle counts in the inner basin, as shown in Figures 4.14, 4.15, and 4.16. During spring tides, the particle counts in the 40 km and 80 km sill models remain approximately constant, and decrease only during neap tides.

The time-dependent efflux-reflux coefficients consist of two parts. The first part is the original expression for the α from Cokelet and Stewart [1985] (Equation 4.16) calculated using the time series of the TEF variables instead of the time-averaged and adjusted values. The second component is the storage term

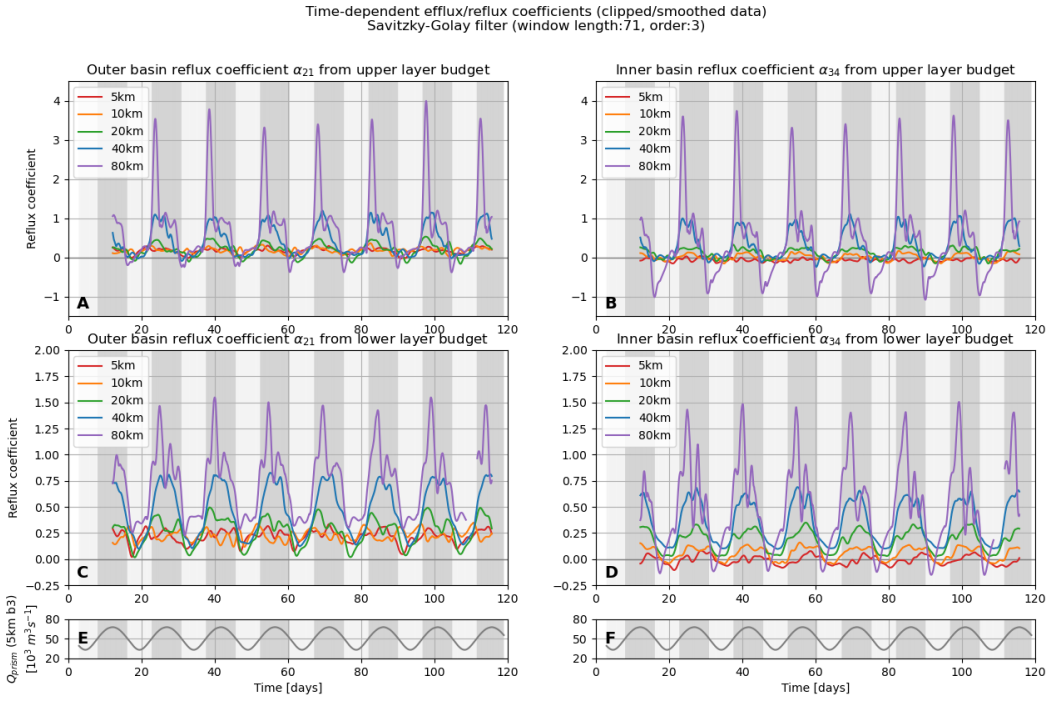

Figure 4.25: Time-dependent reflux coefficients from budgets of the (A,B) upper layer and (C,D) lower layer in TEF box model. Refer to Figure 4.5 for a description of the four α coefficients. Grey shading shows the timing of the spring-neap cycle (peaks of Q_{prism} in the 5 km sill model at section b3 as shown in panels E and F). The efflux coefficient (not shown) and reflux coefficient for a basin sum to 1.

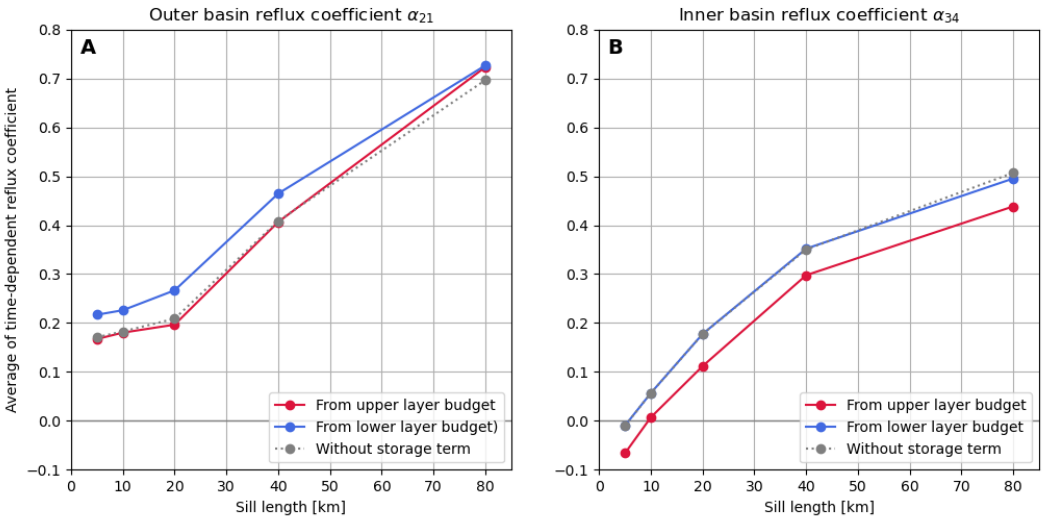

Figure 4.26: Average over seven spring-neap cycles of the time-dependent reflux coefficients from budgets of the upper and lower layer in TEF box model. The upper or lower layer budget is used to calculate the storage term in the time-dependent coefficients. The grey dotted line shows the average of the time-varying reflux coefficients without the storage term included. The efflux coefficient (not shown) and reflux coefficient for a basin sum to 1.

which accounts for changes in the salt content of the sill region, which we calculate in two ways. Panels A and B show the reflux coefficients calculated from a budget of the upper layer of the sill region, while panels C and D use a budget of the lower layer. While the overall behavior is similar, the storage term in the upper layer budget is much larger, especially for the $80\ \mathrm{km}$ sill model. In theory, the time-dependent coefficients calculated from either budget should be the same. However, to simplify the calculation, we have imposed several strong assumptions which may not be appropriate. First, we assume that the volume of each layer is constant and equal to half the volume of the sill. However, in Figure 4.11 we can see that the outflow is located in a thinner upper layer during neap tide. Comparing with Figure 4.12 we also see that there are significant differences in the velocity structure between spring and neap, which means that a constant layer volume assumption may not be justified. Because we use the TEF decomposition, which uses binning in salinity rather than spatial bins, to define the inflows and outflows at the boundaries of the sill, it is not immediately clear how to best delineate the associated volumes within the sill region. We have also assumed that the TEF salinities s_{in} and s_{out} at the midpoint of the sill are representative of the mean salinity in the upper and lower boxes, which may not be the case. If the boundary between the upper and lower boxes was more precisely defined, the mean salinity of each layer could instead be calculated directly from the model output. Figure 4.26 shows the average of the time-dependent reflux coefficients over seven spring neap cycles (the time series shown in Figure 4.25), as well as the average of the time-dependent coefficients excluding the storage term. When averaged all three give similar results. However, for the outer basin reflux α_{21}, the upper layer budget is more similar to the reflux without storage, while the lower layer budget produces more similar results for the inner basin reflux α_{34}. This simply indicates that the storage terms from those budgets average to near zero over several spring-neap cycles, which we would not necessarily expect as there is some drift in the model salinity over time.

4.3.4 Particle visits to the sill

To gain a better understanding of how the sill length and its ratio to the tidal excursion control reentry and reflux, we use the particle tracks to characterize the fate of water entering the sill region. Every particle visit to the sill is categorized as transiting or returning from the inner or outer basin. Figure 4.27 shows histograms of the duration of particle visits for the five different sill lengths. Figure 4.28 shows the average

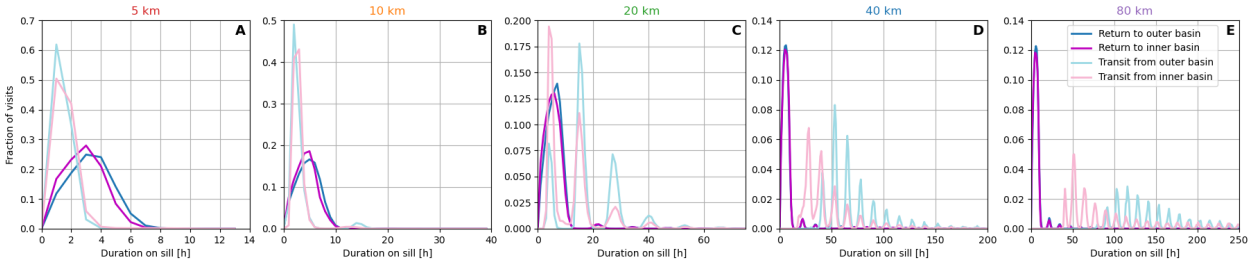

Figure 4.27: Histograms of durations that particles spend on sill for returning and transiting particles from each basin. Subplots show the different model ensemble members, note different axis scaling for each panel. Bin widths are 1 h. Subplots show the different model ensemble members. All particle visits to the sill are included and sorted by their starting and ending basins. Particles that transition from the inner basin to outer basin or vice versa in less than one hour (no position recorded on sill) are assigned a duration of 0 h.

duration for particle visits in each catergory. The durations that particles spend on the sill are linked to the tidal cycle, as shown by the peaks in the histograms, as well as the tidal excursion. In the short sill models (5 km and 10 km), particles transit the sill in less than one tidal cycle because the tidal excursion exceeds the sill length, and the transiting particles spend less time on the sill than those that return to their original basin. Except on rare occasions, particles do not remain on the sill over multiple tidal cycles. As the sill length increases to match the tidal excursion (20 km), the returning particles generally only remain on the sill during a single tidal cycle, but some transiting particles take two, three, or four, tidal cycles to cross the sill. For the long sills (40 km and 80 km), the particles cannot transit the sill in a single tidal cycle. The particles transiting from the inner basin take less time on average than those transiting from the outer basin. Correspondingly, the velocity fields shown in Figures 4.11 and 4.12 exhibit faster outflow than inflow on the sill for the 80 km sill model. The grey dotted line in Figure 4.28 shows the average duration on the sill for all particle visits. This is much closer to the average time for the returning particles in the long sill models, indicating that only a small fraction of particles succeed in crossing the long sills. This is similar to the particle-based reflux results, although the fraction of returning particle visits is greater than the reflux because the track locations are not tidally averaged.

For the returning particles only, we calculate the maximum distance that they reach along the sill before returning to their original basin. (The transiting particles all reach the full length of the sill.) Figure 4.29

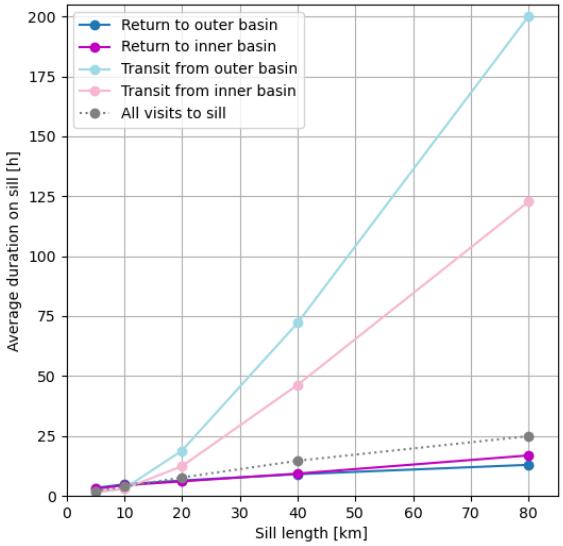

Figure 4.28: Average duration particles spend on sill as a function of sill length for returning and transiting particles from each basin. All particle visits to the sill are included and sorted by their starting and ending basins. Particles that transition from the inner basin to outer basin or vice versa in less than one hour (no position recorded on sill) are assigned a duration of 0 h.

show histograms of the distances reached by the transiting particles. It is always more common for the returning particles to travel only a short distance on the sill. However, for the short sill models, the distribution is flatter, with many particles able to reach the last kilometer of the sill before returning. However, as the sill lengthens, the distances reached by the returning particles become confined to the near end of the sill. Very few particles continue past $\sim 20\mathrm{km}$ before returning to the inner basin, or $\sim 30\mathrm{km}$ for particles originating in the outer basin. Figure 4.30 shows the distribution of distances reached based on the duration that returning particles spend on the sill, and Figure 4.31 shows the average distances and durations as a function of sill length. While the duration spent on the sill scales approximately linearly with sill length, the distance reached increases less rapidly when the sill length exceeds the tidal excursion. When the particles cannot transit the sill during a single ebb or flood tide, they will be advected in the opposite direction before continuing along the sill. Particles will also experience more mixing if they remain on the sill over multiple tidal cycles.

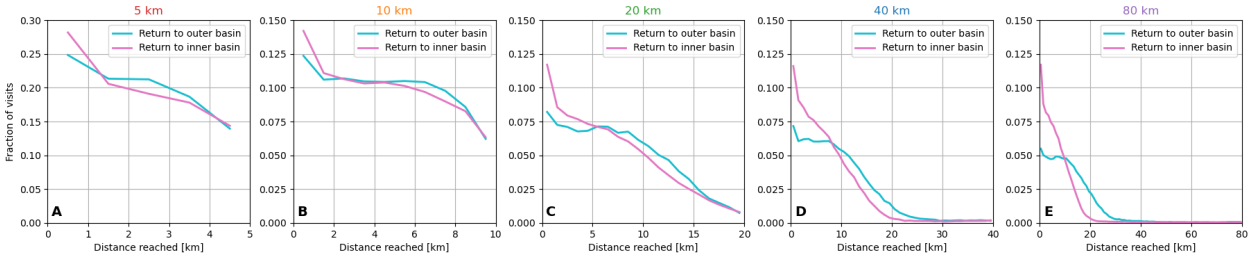

Figure 4.29: Histograms of distances that returning particles reach along the sill for each basin. Bin widths are 1 km. Subplots show the different model ensemble members. All particle visits to the sill that start and end in the same basin are included. The distance is measured from the end of the sill that particles enter from. The subplots have different axis scaling; the particles cannot reach a distance longer than the sill length (upper limit of the displayed x-axis) or they would be counted with the transiting particles.

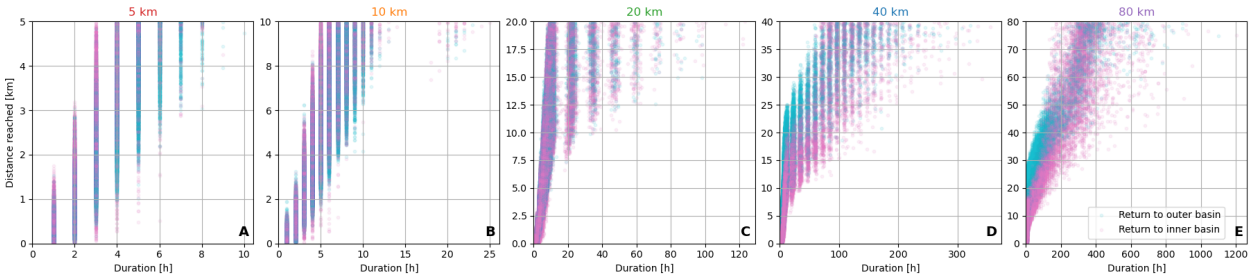

Figure 4.30: Distribution of distances that returning particles reach along the sill plotted against duration spent on the sill. Pink dots show inner basin returning particles and blue dots show outer basin returning particles. Subplots show the different model ensemble members. All particle visits to the sill that start and end in the same basin are included. The distance is measured from the end of the sill that particles enter from. The subplots have different axis scaling; vertical banding in panel A is a result of the particle track sampling time of 1 h, while the bands in panel C are due to the tidal cycle. Note that the particles cannot reach a distance longer than the sill length (top of the displayed y-axis) or they would be counted with the transiting particles.

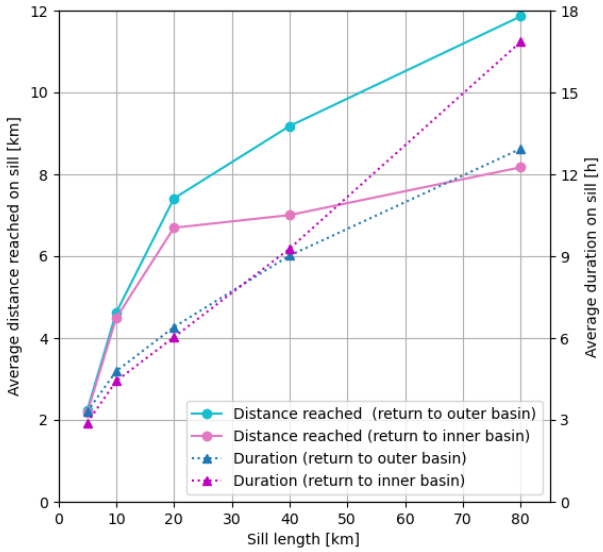

Figure 4.31: Average distance that returning particles reach along the sill as a function of sill length for each basin. The distance is measured from the end of the sill that particles enter from. Note that the particles cannot reach a distance longer than the sill length or they would be counted with the transiting particles. All particle visits to the sill that start and end in the same basin are included. The duration that the returning particles spend on the sill are shown as dotted lines on the secondary y-axis.

4.4 Summary and conclusions

We have used a collection of established and novel methods to explore residence times and reflux in estuaries with sills of varying lengths. By calculating several different transport time scales, we find that longer sills increase retention in the inner basin of the estuary. The increase in e-folding times in the models with longer sills is primarily due to the effect of particles reentering the inner basin from the sill region, often multiple times.

Using the efflux-reflux box model framework of Cokelet and Stewart [1985], we calculate the reflux fractions for the sill region and find that longer sills produce more reflux, with up to half of the water from the inner basin refluxed. Estimating the reflux fractions from the tidally-averaged particle tracks yields similar results. This indicates that mixing and vertical advection on the sill contribute to particle reentry and extended transport time scales. We also present a time-dependent version of the efflux-reflux coefficients which accounts for salt storage in the sill region. We show that reflux is greater at spring tides, when more tidal mixing occurs, and that this effect is most prominent in the long sill models.

The fate of particles entering the sill region is governed by the tidal excursion, which is $20\ \mathrm{km}$ in all of our idealized models. In the short sill models, particles are able to transit the sill in a single ebb or flood tide, and particles do not remain in the sill region for multiple tidal cycles. For the long sill models, particles must spend multiple tidal cycles on the sill in order to transit to the opposite basin. This increases the amount of mixing that the particles experience during their visit to the sill and reduces the overall number of particles transiting the sill, which in turn increases retention and residence times.

The results presented here could be improved and expanded upon in several ways. First, longer particle tracking runs would eliminate issues with residence times that are longer than the duration of the experiment, which skew the averages lower than their true values. Longer experiments would also make the exposure time or non-strict residence time more informative. Using multiple releases would reduce noise in the residence time distributions and allow the effect of release timing in the tidal and spring-neap cycles to be evaluated. These methods could also be used to test how variations in other sill properties, such as the depth or width, alter residence times and reflux.

As described previously, the particle-based method for estimating reflux could be further developed by incorporating other properties from the particle tracks, and addressing sampling bias in the particle visits.

Reflux and mixing in the estuary could also be examined in more spatial detail, for example by using a multi-box model similar to MacCready et al. [2021] or by creating salinity variance budgets similar to those implemented in Chapter 2.

Chapter 5

Conclusion

The results presented in this dissertation provide insight into the functioning of estuaries with complex bathymetry, with a focus on sills.

In Chapter 2, we discovered that the timing of mixing in the Salish Sea is tightly coupled to the river flow. Whidbey Basin, a shallow basin with large freshwater input from the Skagit River, has the most intense mixing. The many rivers feeding the Salish Sea have different annual cycles, depending on the type of watershed they are sourced from. As more watersheds shift towards rain-dominated or mixed snow and rain conditions due to climate change, we can expect the timing of mixing in the Salish Sea to shift as well. Mixing in the Salish Sea, as defined in the salinity variance framework, is extremely concentrated around river mouths. This is because the mixture of water is the Salish Sea is mostly ocean water, causing high mean salinity in the system. As a result fresh river water has very large variance, while the contribution from ocean water is small. In the past, salinity variance has been used to quantify mixing in estuaries where the mean salinity is closer to the midpoint between these two endmembers, so that both ocean and river inputs to the system are significant sources of variance. In estuaries like the Salish Sea where this is not the case, it may be wise to supplement the salinity variance method with other measures of mixing, depending on the application. Numerical mixing in ocean models is often ignored. However, it can be estimated using the residual of salinity variance budgets. We found that numerical mixing contributes approximately one-third of the total in the LiveOcean model.

In Chapter 3, we used an idealized model ensemble to study the effects of varying sill length on the

estuarine exchange flow mechanism. The dominant mechanism varies along the sill, with tidal pumping always important at the ends, and stronger gravitational circulation developing in the middle as the length increases. Short and long sills are found to exhibit different salt flux behavior over the spring-neap cycle, and the transition is shown to occur when the sill length exceeds the tidal excursion. This helps to explain the results of MacCready and Geyer [2024], who found that the exchange flow and the exchange flow salt transport in the Salish Sea can have different trends with increasing tides depending on the location within the estuary. All of our models occupy the same part of the Geyer and MacCready [2014] estuarine parameter space, as they are designed to have the same river flow and tidal velocities over the sill. The differences in their dynamics suggest that an additional nondimensional parameter is required to characterize estuaries with sills, and we recommend using the sill length to tidal excursion ratio. Other types of bathymetric features may require their own distinct nondimensional parameters.

In Chapter 4, we used particle tracking experiments to show that longer sills increase residence times in the inner basin of the estuary. Furthermore, this increase is primarily due to reentry and reflux, which suggests that transport time scales that account for these effect, such as the e-folding time, are most appropriate for our situation. We also showed the importance of carefully placing domain boundaries when investigating the contribution of reflux and other causes of extended residence times. Barring truly exceptional circumstances, the length of sills in the Salish Sea, which are hard bedrock, are unlikely to be modified within our lifetimes and long after. However, in other estuaries around the world that experience natural morphodynamic change or human intervention such as dredging, sill properties vary on much shorter timescales. In these systems it may be possible to apply the relationships found here more directly.

Central to all of this work are themes of renewal and exchange. In this context, we understand mixing, estuarine circulation, and retention not as separate processes, but as tightly intertwined factors creating the overall physical conditions in estuaries. For instance, Chapter 2, which focused on mixing, found that the total amount of mixing in the Salish Sea is directly correlated with the exchange flow salt transport. We also used the concept of mixedness to determine when mixed water is expelled from the estuary. In Chapter 3, we analyzed the subtidal salt transport, and found that its behavior over the spring-neap cycle is regulated by competition between the size of the estuarine circulation and the stratification that it acts upon, which is reduced by tidal mixing. Finally, Chapter 4 brought all of these concepts together in the framework of efflux-

reflux, where mixing at sills transfers water between the inflowing and outflowing layers of the exchange flow, increasing retention in the estuary.

In addition, we reemphasized the significant role of tides in orchestrating the dynamics of complex estuaries. In Chapter 2, we found that the timing of mixing in the Salish Sea was most strongly correlated to the river flow, rather than the spring-neap cycle. Even so, while rivers supply the salinity variance available to be mixed, the mixing itself is effectuated by the tides. Chapters 3 and 4 showed that the length of sills relative to their tidal excursion is an important nondimensional parameter for describing the outcomes of these features. In Chapter 3, this ratio determined whether tidal pumping or gravitational circulation was dominant on the sill. In Chapter 4, we found that sill lengths longer than the tidal excursion increased retention in the inner basin and reflux on the sill. In either case, although we may be interested in the tidally-averaged conditions of the estuary, they are still determined by the movement over the tidal cycle, which determines whether water interacts with the sharp bathymetry at the ends of the sills where tidal pumping is likely to occur, and whether it is able to transit the sill in a single ebb or flood tide. In addition, using the time-dependent formulation of the efflux-reflux coefficients, we showed that reflux is enhanced at spring tides. While our idealized model ensemble used a simple spring-neap cycle derived from M2 and S2 tides, real tides in the Salish Sea have additional sources of short- and long-term variability. Because the tidal excursion at Admiralty Inlet is similar to its length, it may be more sensitive to this variability which could decide whether the sill length is exceeded or not. Future sea level rise is not expected to cause large changes in the amplitudes of the main tidal constituents in the Salish Sea [Pickering et al., 2017; Miller et al., 2019]. However, other parts of the world are predicted to experience significant changes to their tidal range [Pickering et al., 2017].

Moving forward, these methods and results could be built upon by further intermingling the idealized and realistic approaches. First, different realistic elements could be brought into idealized models to study their independent effects. For example, idealized models with a series of sills instead of one could provide a better understanding of Puget Sound's Main Basin, which is bounded by sills at both ends. Another possibility would be to modify the particle tracking experiments to study how sill length affects retention for specific tracers of interest that are not neutrally buoyant, or that undergo growth or decay. Second, the relationships found in the idealized model studies presented here should be tested with models or observations of real

estuaries. Do realistic sills show the patterns of tidal pumping and gravitational circulation expressed in our results in accordance with their sill length to tidal excursion ratio? How much of the variance in residence times across different systems can be accounted for by the sill length to tidal excursion ratio, and what other factors are at play? Finally, new methods developed for our idealized modeling projects could be applied in realistic models such as LiveOcean. In particular, the particle-based efflux-reflux analysis and the time-dependent reflux formulas could be used to calculate reflux across Admiralty Inlet, Tacoma Narrows and other sills.

Bibliography

Alahmed, S., L. Ross, and S. M. C. Smith, 2022: Coastal hydrodynamics and timescales in meso-macrotidal estuaries in the Gulf of Maine: a model study. *Estuaries and Coasts*, **45 (7)**, 1888–1908, https://doi.org/10.1007/s12237-022-01067-9.

Armi, L., and D. M. Farmer, 1986: Maximal two-layer exchange through a contraction with barotropic net flow. *Journal of Fluid Mechanics*, **164**, 27–51, https://doi.org/10.1017/S0022112086002458.

Banas, N. S., L. Conway-Cranos, D. A. Sutherland, P. MacCready, P. Kiffney, and M. Plummer, 2015: Patterns of river influence and connectivity among subbasins of Puget Sound, with application to bacterial and nutrient loading. *Estuaries and Coasts*, **38 (3)**, 735–753, https://doi.org/10.1007/s12237-014-9853-y.

Banas, N. S., B. M. Hickey, P. MacCready, and J. A. Newton, 2004: Dynamics of Willapa Bay, Washington: A highly unsteady, partially mixed estuary. *Journal of Physical Oceanography*, **34 (11)**, 2413 – 2427, https://doi.org/10.1175/JPO2637.1.

Bao, W., and C. Moffat, 2024: Impact of shallow sills on circulation regimes and submarine melting in glacial fjords. *The Cryosphere*, **18 (1)**, 187–203, https://doi.org/10.5194/tc-18-187-2024.

Bo, T., and D. K. Ralston, 2022: Frontogenesis, mixing, and stratification in estuarine channels with curvature. *Journal of Physical Oceanography*, **52 (7)**, 1333 – 1350, https://doi.org/10.1175/JPO-D-21-0298.1.

Bowden, K. F., 1965: Horizontal mixing in the sea due to a shearing current. *Journal of Fluid Mechanics*, **21 (1)**, 83–95, https://doi.org/10.1017/S0022112065000058.

Brasseale, E., and P. MacCready, 2021: The shelf sources of estuarine inflow. *Journal of Physical Oceanography*, **51 (7)**, 2407 – 2421, https://doi.org/10.1175/JPO-D-20-0080.1.

Brasseale, E., and P. MacCready, 2025: Seasonal wind stress direction influences source and properties of inflow to the Salish Sea and Columbia River Estuary. *Journal of Geophysical Research: Oceans*, **130 (2)**, e2024JC022 024, https://doi.org/doi.org/10.1029/2024JC022024.

Brooks, D., M. Baca, and Y.-T. Lo, 1999: Tidal circulation and residence time in a macrotidal estuary: Cobscook Bay, Maine. *Estuarine, Coastal and Shelf Science*, **49 (5)**, 647–665, https://doi.org/10.1006/ecss.1999.0544.

Burchard, H., F. Janssen, K. Bolding, L. Umlauf, and H. Rennau, 2009: Model simulations of dense bottom currents in the Western Baltic Sea. *Continental Shelf Research*, **29 (1)**, 205–220, https://doi.org/10.1016/j.csr.2007.09.010.

Burchard, H., X. Lange, K. Klingbeil, and P. MacCready, 2019: Mixing estimates for estuaries. *Journal of Physical Oceanography*, **49 (2)**, 631–648, https://doi.org/10.1175/JPO-D-18-0147.1.

Burchard, H., and H. Rennau, 2008: Comparative quantification of physically and numerically induced mixing in ocean models. *Ocean Modelling*, **20 (3)**, 293–311, https://doi.org/10.1016/j.ocemod.2007.10.003.

Burchard, H., and H. M. Schuttelaars, 2012: Analysis of tidal straining as driver for estuarine circulation in well-mixed estuaries. *Journal of Physical Oceanography*, **42 (2)**, 261 – 271, https://doi.org/10.1175/JPO-D-11-0110.1.

Burchard, H., and Coauthors, 2018: The Knudsen theorem and the Total Exchange Flow analysis framework applied to the Baltic Sea. *Progress in Oceanography*, **165 (April)**, 268–286, https://doi.org/10.1016/j.pocean.2018.04.004.

Cannon, G., and N. Laird, 1978: Variability of currents and water properties from year-long observations in a fjord estuary. *Hydrodynamics of Estuaries and Fjords*, J. C. Nihoul, Ed., Elsevier Oceanography Series, Vol. 23, Elsevier, 515–535, https://doi.org/10.1016/S0422-9894(08)71296-0.

Casola, J., J. Kay, A. Snover, R. Norheim, and L. Whitely Binder, 2005: Climate impacts on Washington's hydropower, water supply, forests, fish, and agriculture. Tech. rep., prepared for King County (Washington) by the Climate Impacts Group (Center for Science in the Earth System, Joint Institute for the Study

of the Atmosphere and Ocean, University of Washington). URL http://cses.washington.edu/cig/outreach/workshopfiles/kingco2005/kc05whitepaper.pdf.

Chen, S.-N., W. R. Geyer, D. K. Ralston, and J. A. Lerczak, 2012: Estuarine exchange flow quantified with isohaline coordinates: Contrasting long and short estuaries. *Journal of Physical Oceanography*, **42 (5)**, 748 – 763, https://doi.org/10.1175/JPO-D-11-086.1.

Cokelet, E. D., and R. J. Stewart, 1985: The exchange of water in fjords: The efflux/reflux theory of advective reaches separated by mixing zones. *Journal of Geophysical Research: Oceans*, **90 (C4)**, 7287–7306, https://doi.org/10.1029/JC090iC04p07287.

Delhez, E. J., A. W. Heemink, and E. Deleersnijder, 2004: Residence time in a semi-enclosed domain from the solution of an adjoint problem. *Estuarine, Coastal and Shelf Science*, **61 (4)**, 691–702, https://doi.org/doi.org/10.1016/j.ecss.2004.07.013.

Deppe, R. W., J. Thomson, B. Polagye, and C. Krembs, 2018: Predicting deep water intrusions to Puget Sound, WA (USA), and the seasonal modulation of dissolved oxygen. *Estuaries and Coasts*, **41 (1)**, 114–127, https://doi.org/10.1007/s12237-017-0274-6.

Dijkstra, Y. M., H. M. Schuttelaars, and H. Burchard, 2017: Generation of exchange flows in estuaries by tidal and gravitational eddy viscosity-shear covariance (ESCO). *Journal of Geophysical Research: Oceans*, **122 (5)**, 4217–4237, https://doi.org/10.1002/2016JC012379.

Dronkers, J., and J. van de Kreeke, 1986: Experimental determination of salt intrusion mechanisms in the Volkerak estuary. *Netherlands Journal of Sea Research*, **20 (1)**, 1–19, https://doi.org/10.1016/0077-7579(86)90056-6.

Ebbesmeyer, C. C., J. Q. Word, and C. A. Barnes, 1988: Puget Sound: A fjord system homogenized with water recycled over sills by tidal mixing. *Hydrodynamics of Estuaries*, B. Kjerfve, Ed., Vol. 2, 1st ed., CRC Press, 75–84.

Engel, L., and M. Stacey, 2024: Timescales of ecological processes, settling, and estuarine transport to create estuarine turbidity maxima: An application of the Peter–Parker model. *Water*, **16 (15)**, https://doi.org/10.3390/w16152084.

Engel, P. A., 2009: Spatial and temporal variability of tide-induced salt flux in a partially mixed estuary. M.S. thesis, Joint Program in Oceanography/Applied Ocean Science and Engineering (Massachusetts Institute of Technology, Dept. of Earth, Atmospheric, and Planetary Sciences; and the Woods Hole Oceanographic Institution), Massachusetts Institute of Technology and Woods Hole Oceanographic Institution, 45 pp.

Farmer, D. M., and L. Armi, 1986: Maximal two-layer exchange over a sill and through the combination of a sill and contraction with barotropic flow. *Journal of Fluid Mechanics*, **164**, 53–76, https://doi.org/10.1017/S002211208600246X.

Farmer, H. G., and M. Rattray, 1963: A model study of the steady-state salinity distribution in Puget Sound. Technical Report 85, University of Washington Department of Oceanography. URL http://hdl.handle.net/1773/16020.

Fischer, H., and W. Matthäus, 1996: The importance of the Drogden Sill in the Sound for major Baltic inflows. *Journal of Marine Systems*, **9 (3)**, 137–157, https://doi.org/10.1016/S0924-7963(96)00046-2.

Fram, J. P., M. A. Martin, and M. T. Stacey, 2007: Dispersive fluxes between the coastal ocean and a semienclosed estuarine basin. *Journal of Physical Oceanography*, **37 (6)**, 1645 – 1660, https://doi.org/10.1175/JPO3078.1.

Garcia, A. M. P., and W. R. Geyer, 2023: Tidal dispersion in short estuaries. *Journal of Geophysical Research: Oceans*, **128 (2)**, e2022JC018 883, https://doi.org/10.1029/2022JC018883.

Geyer, W. R., and G. A. Cannon, 1982: Sill processes related to deep water renewal in a fjord. *Journal of Geophysical Research: Oceans*, **87 (C10)**, 7985–7996, https://doi.org/10.1029/JC087iC10p07985.

Geyer, W. R., and P. MacCready, 2014: The estuarine circulation. *Annual Review of Fluid Mechanics*, **46 (Volume 46, 2014)**, 175–197, https://doi.org/10.1146/annurev-fluid-010313-141302.

Geyer, W. R., and H. Nepf, 1996: Tidal pumping of salt in a moderately stratified estuary. *Buoyancy Effects on Coastal and Estuarine Dynamics*, D. G. Aubrey, and C. T. Friedrichs, Eds., American Geophysical Union (AGU), chap. 15, 213–226, https://doi.org/10.1029/CE053p0213, URL https://agupubs.onlinelibrary.wiley.com/doi/abs/10.1029/CE053p0213.

Geyer, W. R., D. K. Ralston, and J.-L. Chen, 2020: Mechanisms of exchange flow in an estuary with a narrow, deep channel and wide, shallow shoals. *Journal of Geophysical Research: Oceans*, **125 (12)**, e2020JC016 092, https://doi.org/10.1029/2020JC016092.

Giddings, S. N., and P. MacCready, 2017: Reverse estuarine circulation due to local and remote wind forcing, enhanced by the presence of along-coast estuaries. *Journal of Geophysical Research: Oceans*, **122 (12)**, 10 184–10 205, https://doi.org/10.1002/2016JC012479.

Godin, G., 1972: *The Analysis of Tides*. University of Toronto Press.

Hager, A. O., D. A. Sutherland, J. M. Amundson, R. H. Jackson, C. Kienholz, R. J. Motyka, and J. D. Nash, 2022: Subglacial discharge reflux and buoyancy forcing drive seasonality in a silled glacial fjord. *Journal of Geophysical Research: Oceans*, **127 (5)**, e2021JC018 355, https://doi.org/10.1029/2021JC018355.

Hansen, D. V., and M. Rattray, 1965: Gravitational circulation in straits and estuaries. *Journal of Marine Research*, **23 (2)**, 104–122, https://elischolar.library.yale.edu/journal_of_marine_research/1048.

Helfrich, K. R., 1995: Time-dependent two-layer hydraulic exchange flows. *Journal of Physical Oceanography*, **25 (3)**, 359 – 373, https://doi.org/10.1175/1520-0485(1995)025<0359:TDTLHE>2.0.CO;2.

Horner-Devine, A. R., R. D. Hetland, and D. G. MacDonald, 2015: Mixing and transport in coastal river plumes. *Annual Review of Fluid Mechanics*, **47 (Volume 47, 2015)**, 569–594, https://doi.org/10.1146/annurev-fluid-010313-141408.

Jay, D. A., and J. D. Musiak, 1994: Particle trapping in estuarine tidal flows. *Journal of Geophysical Research: Oceans*, **99 (C10)**, 20 445–20 461, https://doi.org/10.1029/94JC00971.

Jay, D. A., and J. D. Smith, 1990: Residual circulation in shallow estuaries: 1. highly stratified, narrow estuaries. *Journal of Geophysical Research: Oceans*, **95 (C1)**, 711–731, https://doi.org/10.1029/JC095iC01p00711.

Klymak, J. M., and M. C. Gregg, 2003: The role of upstream waves and a downstream density pool in the growth of lee waves: Stratified flow over the Knight Inlet sill. *Journal of Physical Oceanography*, **33 (7)**, 1446 – 1461, https://doi.org/10.1175/1520-0485(2003)033<1446:TROUWA>2.0.CO;2.

Knudsen, M., 1900: Ein hydrographischer Lehrsatz. *Annalen der Hydrographie und Maritimen Meteorologie*.

Lange, X., K. Klingbeil, and H. Burchard, 2020: Inversions of estuarine circulation are frequent in a weakly tidal estuary with variable wind forcing and seaward salinity fluctuations. *Journal of Geophysical Research: Oceans*, **125 (9)**, https://doi.org/10.1029/2019JC015789.

Lee, S.-Y., and A. F. Hamlet, 2011: Skagit River Basin Climate Science Report. Tech. rep., prepared for Skagit County and the Envision Skagit Project by the Department of Civil and Environmental Engineering and the Climate Impacts Group, University of Washington. URL https://www.skagitcounty.net/EnvisionSkagit/Documents/ClimateChange/Complete.pdf.

Lerczak, J. A., and W. R. Geyer, 2004: Modeling the lateral circulation in straight, stratified estuaries. *Journal of Physical Oceanography*, **34 (6)**, 1410 – 1428, https://doi.org/10.1175/1520-0485(2004)034<1410:MTLCIS>2.0.CO;2.

Lerczak, J. A., W. R. Geyer, and R. J. Chant, 2006: Mechanisms driving the time-dependent salt flux in a partially stratified estuary. *Journal of Physical Oceanography*, **36 (12)**, 2296 – 2311, https://doi.org/10.1175/JPO2959.1.

Li, X., W. R. Geyer, J. Zhu, and H. Wu, 2018: The transformation of salinity variance: A new approach to quantifying the influence of straining and mixing on estuarine stratification. *Journal of Physical Oceanography*, **48 (3)**, 607–623, https://doi.org/10.1175/JPO-D-17-0189.1.

Lorenz, M., K. Klingbeil, P. MacCready, and H. Burchard, 2019: Numerical issues of the Total Exchange Flow (TEF) analysis framework for quantifying estuarine circulation. *Ocean Science*, **15 (3)**, 601–614, https://doi.org/10.5194/os-15-601-2019.

MacCready, P., 1999: Estuarine adjustment to changes in river flow and tidal mixing. *Journal of Physical Oceanography*, **29 (4)**, 708 – 726, https://doi.org/10.1175/1520-0485(1999)029<0708:EATCIR>2.0.CO;2.

MacCready, P., 2011: Calculating estuarine exchange flow using isohaline coordinates. *Journal of Physical Oceanography*, **41 (6)**, 1116 – 1124, https://doi.org/10.1175/2011JPO4517.1.

MacCready, P., and W. R. Geyer, 2010: Advances in estuarine physics. *Annual Review of Marine Science*, **2 (Volume 2, 2010)**, 35–58, https://doi.org/10.1146/annurev-marine-120308-081015.

MacCready, P., and W. R. Geyer, 2024: Estuarine exchange flow in the Salish Sea. *Journal of Geophysical Research: Oceans*, **129 (1)**, e2023JC020 369, https://doi.org/10.1029/2023JC020369.

MacCready, P., W. R. Geyer, and H. Burchard, 2018: Estuarine exchange flow is related to mixing through the salinity variance budget. *Journal of Physical Oceanography*, **48 (6)**, 1375–1384, https://doi.org/10.1175/JPO-D-17-0266.1.

MacCready, P., and S. N. Giddings, 2016: The mechanical energy budget of a regional ocean model. *Journal of Physical Oceanography*, **46 (9)**, 2719–2733, https://doi.org/10.1175/JPO-D-16-0086.1.

MacCready, P., and Coauthors, 2021: Estuarine circulation, mixing, and residence times in the Salish Sea. *Journal of Geophysical Research: Oceans*, **126 (2)**, e2020JC016 738, https://doi.org/10.1029/2020JC016738.

MacVean, L. J., and M. T. Stacey, 2011: Estuarine dispersion from tidal trapping: A new analytical framework. *Estuaries and Coasts*, **34 (1)**, 45–59, https://doi.org/10.1007/s12237-010-9298-x.

Mehta, A., and E. Özsoy, 1978: 3 - Inlet hydraulics: 3.1 Flow dynamics and nearshore transport. *Stability of Tidal Inlets*, P. Bruun, Ed., Developments in Geotechnical Engineering, Vol. 23, Elsevier, 83–161, https://doi.org/10.1016/B978-0-444-41728-2.50011-4.

Miles, J. W., and Y. K. Lee, 1975: Helmholtz resonance of harbours. *Journal of Fluid Mechanics*, **67 (3)**, 445–464, https://doi.org/10.1017/S0022112075000407.

Miller, I., Z. Yang, N. VanArendonk, E. Grossman, G. S. Mauger, and H. Morgan, 2019: Extreme coastal water level in Washington State: Guidelines to support sea level rise planning. Tech. rep., A collaboration of Washington Sea Grant, University of Washington Climate Impacts Group, Oregon State University, University of Washington, Pacific Northwest National Laboratory and U.S. Geological Survey. Prepared for the Washington Coastal Resilience Project. URL https://cig.uw.edu/publications/extreme-coastal-water-level-in-washington-state-guidelines-to-support-sea-level-rise-planning/.

Monsen, N. E., J. E. Cloern, L. V. Lucas, and S. G. Monismith, 2002: A comment on the use of flushing time, residence time, and age as transport time scales. *Limnology and Oceanography*, **47 (5)**, 1545–1553, https://doi.org/10.4319/lo.2002.47.5.1545.

Okubo, A., 1973: Effect of shoreline irregularities on streamwise dispersion in estuaries and other embayments. *Netherlands Journal of Sea Research*, **6 (1)**, 213–224, https://doi.org/10.1016/0077-7579(73)90014-8.

Peters, H., and R. Bokhorst, 2001: Microstructure observations of turbulent mixing in a partially mixed estuary. Part II: salt flux and stress. *Journal of Physical Oceanography*, **31 (4)**, 1105–1119, https://doi.org/10.1175/1520-0485(2001)031<1105:MOOTMI>2.0.CO;2.

Pickering, M., K. Horsburgh, J. Blundell, J.-M. Hirschi, R. Nicholls, M. Verlaan, and N. Wells, 2017: The impact of future sea-level rise on the global tides. *Continental Shelf Research*, **142**, 50–68, https://doi.org/10.1016/j.csr.2017.02.004.

Premathilake, L., and T. Khangaonkar, 2022: Explicit quantification of residence and flushing times in the Salish Sea using a sub-basin scale shoreline resolving model. *Estuarine, Coastal and Shelf Science*, **276**, 108 022, https://doi.org/10.1016/j.ecss.2022.108022.

Ralston, D. K., 2022: Impacts of storm surge barriers on drag, mixing, and exchange flow in a partially mixed estuary. *Journal of Geophysical Research: Oceans*, **127 (4)**, e2021JC018 246, https://doi.org/doi.org/10.1029/2021JC018246.

Ralston, D. K., G. W. Cowles, W. R. Geyer, and R. C. Holleman, 2017: Turbulent and numerical mixing in a salt wedge estuary: Dependence on grid resolution, bottom roughness, and turbulence closure. *Journal of Geophysical Research: Oceans*, **122 (1)**, 692–712, https://doi.org/doi.org/10.1002/2016JC011738.

Ralston, D. K., W. R. Geyer, and J. A. Lerczak, 2010: Structure, variability, and salt flux in a strongly forced salt wedge estuary. *Journal of Geophysical Research: Oceans*, **115 (C6)**, https://doi.org/10.1029/2009JC005806.

Rayson, M. D., E. S. Gross, R. D. Hetland, and O. B. Fringer, 2016: Time scales in Galveston Bay: An

unsteady estuary. *Journal of Geophysical Research: Oceans*, **121 (4)**, 2268–2285, https://doi.org/doi.org/10.1002/2015JC011181.

Scully, M. E., C. Friedrichs, and J. Brubaker, 2005: Control of estuarine stratification and mixing by wind-induced straining of the estuarine density field. *Estuaries*, **28 (3)**, 321–326, https://doi.org/10.1007/BF02693915.

Scully, M. E., W. R. Geyer, and J. A. Lerczak, 2009: The influence of lateral advection on the residual estuarine circulation: A numerical modeling study of the Hudson River estuary. *Journal of Physical Oceanography*, **39 (1)**, 107 – 124, https://doi.org/10.1175/2008JPO3952.1.

Shchepetkin, A. F., and J. C. McWilliams, 2005: The regional oceanic modeling system (ROMS): a split-explicit, free-surface, topography-following-coordinate oceanic model. *Ocean Modelling*, **9 (4)**, 347–404, https://doi.org/10.1016/j.ocemod.2004.08.002.

Simpson, J. H., J. Brown, J. Matthews, and G. Allen, 1990: Tidal straining, density currents, and stirring in the control of estuarine stratification. *Estuaries*, **13 (2)**, 125–132, https://doi.org/10.2307/1351581.

Stigebrandt, A., 1976: Vertical diffusion driven by internal waves in a sill fjord. *Journal of Physical Oceanography*, **6 (4)**, 486 – 495, https://doi.org/10.1175/1520-0485(1976)006<0486:VDDBIW>2.0.CO;2.

Stigebrandt, A., 1977: On the effect of barotropic current fluctuations on the two-layer transport capacity of a constriction. *Journal of Physical Oceanography*, **7 (1)**, 118 – 122, https://doi.org/10.1175/1520-0485(1977)007<0118:OTEOBC>2.0.CO;2.

Stigebrandt, A., 1980: Some aspects of tidal interaction with fjord constrictions. *Estuarine and Coastal Marine Science*, **11 (2)**, 151–166, https://doi.org/10.1016/S0302-3524(80)80038-7.

Stommel, H., and H. G. Farmer, 1952: On the nature of estuarine circulation. Tech. rep., Woods Hole Oceanographic Institution. https://doi.org/10.1575/1912/2032, URL https://hdl.handle.net/1912/2032.

Taylor, G. I., 1953: Dispersion of soluble matter in solvent flowing slowly through a tube. *Proceedings*

of the Royal Society of London. Series A. Mathematical and Physical Sciences, **219 (1137)**, 186–203, https://doi.org/10.1098/rspa.1953.0139.

The SeaDoc Society, 2021: About the Salish Sea. https://www.seadocsociety.org/about-the-salish-sea.

Thomson, R. E., S. F. Mihály, and E. A. Kulikov, 2007: Estuarine versus transient flow regimes in Juan de Fuca Strait. *Journal of Geophysical Research: Oceans*, **112 (9)**, 1–25, https://doi.org/10.1029/2006JC003925.

U.S. Environmental Protection Agency, 2025: Basic information about estuaries. Https://www.epa.gov/nep/basic-information-about-estuaries.

Valle-Levinson, A., and R. Wilson, 1998: Rotation and vertical mixing effects on volume exchange in eastern Long Island Sound. *Estuarine, Coastal and Shelf Science*, **46 (4)**, 573–585, https://doi.org/10.1006/ecss.1997.0310.

Virtanen, P., and Coauthors, 2020: SciPy 1.0: Fundamental Algorithms for Scientific Computing in Python. *Nature Methods*, **17**, 261–272, https://doi.org/10.1038/s41592-019-0686-2.

Walters, R. A., and C. Heston, 1982: Removing tidal-period variations from time-series data using low-pass digital filters. *Journal of Physical Oceanography*, **12 (1)**, 112–115, https://doi.org/10.1175/1520-0485(1982)012<0112:rtpvft>2.0.co;2.

Wang, C.-F., M.-H. Hsu, and A. Y. Kuo, 2004: Residence time of the Danshuei River estuary, Taiwan. *Estuarine, Coastal and Shelf Science*, **60 (3)**, 381–393, https://doi.org/10.1016/j.ecss.2004.01.013.

Wang, T., and W. R. Geyer, 2018: The balance of salinity variance in a partially stratified estuary: Implications for exchange flow, mixing, and stratification. *Journal of Physical Oceanography*, **48 (12)**, 2887–2899, https://doi.org/10.1175/JPO-D-18-0032.1.

Wang, T., W. R. Geyer, and P. MacCready, 2017: Total Exchange Flow, entrainment, and diffusive salt flux in estuaries. *Journal of Physical Oceanography*, **47 (5)**, 1205–1220, https://doi.org/10.1175/JPO-D-16-0258.1.

Wang, T., Z. Wei, W. Jiang, T. Xu, J. L. Chen, and C. Bian, 2021: Quantification of numerical mixing in coastal ocean models through an offline method. *Ocean Engineering*, **222 (March 2020)**, 108 588, https://doi.org/10.1016/j.oceaneng.2021.108588.

Warner, J. C., W. R. Geyer, D. K. Ralston, and T. Kalra, 2020: Using tracer variance decay to quantify variability of salinity mixing in the Hudson River Estuary. *Journal of Geophysical Research: Oceans*, **125 (12)**, 1–18, https://doi.org/10.1029/2020JC016096.

Whitney, M. M., Y. Jia, P. M. McManus, and C. J. Kunz, 2014: Sill effects on physical dynamics in eastern Long Island Sound. *Ocean Dynamics*, **64 (3)**, 443–458, https://doi.org/10.1007/s10236-013-0681-6.

Wong, K.-C., 1994: On the nature of transverse variability in a coastal plain estuary. *Journal of Geophysical Research: Oceans*, **99 (C7)**, 14 209–14 222, https://doi.org/10.1029/94JC00861.

Xiong, J., and P. MacCready, 2024: Intercomparisons of Tracker v1.1 and four other ocean particle-tracking software packages in the Regional Ocean Modeling System. *Geoscientific Model Development*, **17 (8)**, 3341–3356, https://doi.org/10.5194/gmd-17-3341-2024.

Xiong, J., J. Shen, and Q. Qin, 2021a: Exchange flow and material transport along the salinity gradient of a long estuary. *Journal of Geophysical Research: Oceans*, **126 (5)**, e2021JC017 185, https://doi.org/10.1029/2021JC017185.

Xiong, J., J. Shen, Q. Qin, and J. Du, 2021b: Water exchange and its relationships with external forcings and residence time in Chesapeake Bay. *Journal of Marine Systems*, **215**, 103 497, https://doi.org/doi.org/10.1016/j.jmarsys.2020.103497.

Yu, Z., Y. Fan, E. J. Metzger, and O. M. Smedstad, 2018: The wind work input into the global ocean revealed by a 17-year global HYbrid coordinate ocean model reanalysis. *Ocean Modelling*, **130 (August)**, 29–39, https://doi.org/10.1016/j.ocemod.2018.07.009.

Chapter A

Appendix: Derivation of salinity variance budget from diagnostics

To create a salinity variance budget from ROMS averages and diagnostics files, we start with a salt budget:

$$\texttt{salt\_rate} = \texttt{salt\_xavd} + \texttt{salt\_yavd} + \texttt{salt\_vavd} + \texttt{salt\_hdiff} + \texttt{salt\_vdiff} \tag{A.1}$$

where `salt_xavd`, `salt_yavd`, and `salt_vavd` are diagnostics that give the rates of change due to advection in the x, y and z directions, respectively, and `salt_hdiff` and `salt_vdiff` are diagnostics that give the rates of change due to horizontal and vertical diffusion, respectively. `salt_rate` is the total rate of change in the salt content of the model cell, defined in ROMS as

$$\texttt{salt\_rate} \equiv \frac{\langle \frac{\partial}{\partial t}(\delta s) \rangle}{\langle \delta \rangle} \tag{A.2}$$

where δ is the thickness of the cell and angle brackets represent averaging over the hour. Since the model has 30 terrain following vertical layers, the cell thickness changes over time as the sea surface height changes. In the interest of physical interpretability, we will apply a thickness correction to the budget in Equation A.1 to account for this effect. Dropping the angle brackets and following MacCready and Giddings [2016], Equation A.2 can be expanded as:

$$\texttt{salt\_rate} = \frac{\delta \frac{\partial s}{\partial t} + s \frac{\partial \delta}{\partial t}}{\delta} \tag{A.3}$$

$$\frac{\partial s}{\partial t} = \texttt{salt\_rate} - \frac{s}{\delta} \frac{\partial \delta}{\partial t} \tag{A.4}$$

The values of s and δ are taken from the averages files, while the derivative $\partial\delta/\partial t$ can be calculated from the history files. The final term in Equation A.4 is the thickness correction that we apply to both sides of Equation A.1:

$$\texttt{salt\_rate} - \frac{s}{\delta} \frac{\partial \delta}{\partial t} = \texttt{salt\_xavd} + \texttt{salt\_yavd} + \left(\texttt{salt\_vavd} - \frac{s}{\delta} \frac{\partial \delta}{\partial t} \right) + \texttt{salt\_hdiff} + \texttt{salt\_vdiff} \tag{A.5}$$

Now the left-hand side is equal to $\partial s/\partial t$. We have grouped the thickness correction with the vertical advection on the right-hand side since the moving cell boundaries artificially change the advection though the top and bottom of the cell. The quantities s and δ are taken from the averages files while $\partial\delta/\partial t$ is calculated from the history files at the start and end of the hour. Similarly to the development in Section 2.2.1, to create a salinity variance budget we multiply both sides of the equation by $2s'$:

$$2s' \left[\texttt{salt\_rate} - \frac{s}{\delta} \frac{\partial \delta}{\partial t} \right] = 2s' \left[\texttt{salt\_xavd} + \texttt{salt\_yavd} + \left(\texttt{salt\_vavd} - \frac{s}{\delta} \frac{\partial \delta}{\partial t} \right) \right] + 2s' \left[\texttt{salt\_hdiff} + \texttt{salt\_vdiff} \right] \tag{A.6}$$

This equation balances exactly in every model cell. If we take the volume integral over the same volume V used to calculate $\bar{s}$,

$$\int_V 2s' \left[\texttt{salt\_rate} - \frac{s}{\delta}\frac{\partial \delta}{\partial t}\right] dV = \int_V 2s' \left[\texttt{salt\_xavd} + \texttt{salt\_yavd} + \left(\texttt{salt\_vavd} - \frac{s}{\delta}\frac{\partial \delta}{\partial t}\right)\right] dV + \int_V 2s' \left[\texttt{salt\_hdiff} + \texttt{salt\_vdiff}\right] dV \quad \text{(A.7)}$$

This is the salinity variance budget constructed from averages and diagnostics. Note that the integrand on the left-hand side of Equation A.7 is $2s'\partial s/\partial t$. Similarly to Section 2.2.1, we can expand $s = \bar{s} + s'$:

$$\int_V 2s' \frac{\partial s}{\partial t}\, dV = \int_V 2s' \frac{\partial \bar{s}}{\partial t}\, dV + \int_V 2s' \frac{\partial s'}{\partial t}\, dV \quad \text{(A.8)}$$

The first term on the right-hand side of Equation A.8 can be eliminated since $\bar{s}$ has no spatial gradients and the volume integral of s' is zero by definition. Therefore

$$\int_V 2s' \frac{\partial s}{\partial t}\, dV = \int_V 2s' \frac{\partial s'}{\partial t}\, dV \quad \text{(A.9)}$$

Using the inverse product rule, we can reformulate the right-hand side of Equation A.9:

$$\int_V 2s' \frac{\partial s}{\partial t}\, dV = \int_V \frac{\partial}{\partial t}\left(s'^2\right)\, dV \quad \text{(A.10)}$$

This means that

$$\int_V 2s' \left[\texttt{salt\_rate} - \frac{s}{\delta}\frac{\partial \delta}{\partial t}\right] dV = \int_V \frac{\partial}{\partial t}\left(s'^2\right)\, dV \quad \text{(A.11)}$$

The diagnostic advection fields in each direction give the change in the salt content of a cell due to the difference in salt fluxes through opposite cell walls. Therefore, the integrand of first term on the right-hand side of Equation A.7 is a divergence:

$$2s' \left[\texttt{salt\_xavd} + \texttt{salt\_yavd} + \left(\texttt{salt\_vavd} - \frac{s}{\delta}\frac{\partial \delta}{\partial t}\right)\right] = -2s' \nabla \cdot (\boldsymbol{u} s) \quad \text{(A.12)}$$

and if we assume incompressibility,

$$2s'\left[\texttt{salt\_xavd} + \texttt{salt\_yavd} + \left(\texttt{salt\_vavd} - \frac{s}{\delta}\frac{\partial \delta}{\partial t}\right)\right] = -2s'\boldsymbol{u}\cdot\nabla s \tag{A.13}$$

Again using the inverse product rule, we obtain

$$2s'\left[\texttt{salt\_xavd} + \texttt{salt\_yavd} + \left(\texttt{salt\_vavd} - \frac{s}{\delta}\frac{\partial \delta}{\partial t}\right)\right] = -\boldsymbol{u}\cdot\nabla(s'^2) \tag{A.14}$$

and taking the volume integral produces

$$\int_V 2s'\left[\texttt{salt\_xavd} + \texttt{salt\_yavd} + \left(\texttt{salt\_vavd} - \frac{s}{\delta}\frac{\partial \delta}{\partial t}\right)\right] dV = -\int_V \boldsymbol{u}\cdot\nabla(s'^2)\, dV \tag{A.15}$$

Substituting Equation A.11 and Equation A.15 into the diagnostics budget Equation A.7 we find:

$$\int_V \left[\frac{\partial}{\partial t}(s'^2) + \boldsymbol{u}\cdot\nabla(s'^2)\right] dV = \int_V 2s'\left[\texttt{salt\_hdiff} + \texttt{salt\_vdiff}\right] dV \tag{A.16}$$

Using the same reasoning as presented in Section 2.2.1, we can move the derivative on the right-hand side outside the integral due to the Reynolds transport theorem:

$$\frac{d}{dt}\int_V \left(s'^2\right)\, dV = -\int_A s'^2\boldsymbol{u}\cdot\hat{\boldsymbol{n}}\, dA + \int_V 2s'\left[\texttt{salt\_hdiff} + \texttt{salt\_vdiff}\right] dV \tag{A.17}$$

Now we can see that Equation A.7 is an exact salinity variance budget constructed from the diagnostics with three terms:

$$\text{Storage} = \text{Advection} + \text{Diffusion} \tag{A.18}$$

where

$$\text{Storage: } \int_V 2s'\left[\texttt{salt\_rate} - \frac{s}{\delta}\frac{\partial \delta}{\partial t}\right] dV \tag{A.19}$$

$$\text{Advection: } \int_V 2s'\left[\texttt{salt\_xavd} + \texttt{salt\_yavd} + \left(\texttt{salt\_vavd} - \frac{s}{\delta}\frac{\partial \delta}{\partial t}\right)\right] dV \tag{A.20}$$

$$\text{Mixing: } \int_V 2s' \left[\texttt{salt\_hdiff} + \texttt{salt\_vdiff}\right] dV \tag{A.21}$$